LOW FREQUENCY VIBRATION ISOLATION AND ALIGNMENT SYSTEM FOR ADVANCED LIGO

A DISSERTATION

SUBMITTED TO THE DEPARTMENT OF ELECTRICAL ENGINEERING

AND THE COMMITTEE ON GRADUATE STUDIES

OF STANFORD UNIVERSITY

IN PARTIAL FULFILLMENT OF THE REQUIREMENTS

FOR THE DEGREE OF

DOCTOR OF PHILOSOPHY

Wensheng Hua

June 2005

I certify that I have read this dissertation and that, in my opinion, it is fully adequate in scope and quality as a dissertation for the degree of Doctor of Philosophy.

_____
Daniel B. DeBra
(Principal Co-Advisor)

I certify that I have read this dissertation and that, in my opinion, it is fully adequate in scope and quality as a dissertation for the degree of Doctor of Philosophy.

_____
Claire J. Tomlin
(Principal Co-Advisor)

I certify that I have read this dissertation and that, in my opinion, it is fully adequate in scope and quality as a dissertation for the degree of Doctor of Philosophy.

_____
Stephen P. Boyd

I certify that I have read this dissertation and that, in my opinion, it is fully adequate in scope and quality as a dissertation for the degree of Doctor of Philosophy.

_____
Norna A. Robertson

I certify that I have read this dissertation and that, in my opinion, it is fully adequate in scope and quality as a dissertation for the degree of Doctor of Philosophy.

<div style="text-align:center">

_____

Brian T. Lantz

</div>

Approved for the University Committee on Graduate Studies.

Abstract

The Laser Interferometer Gravitational-Wave Observatory (LIGO) is dedicated to the observation of astrophysical sources through detection of gravitational waves. In order to reach the sensitivity requirements for Advanced LIGO, the isolation and alignment system for the optics must reduce the RMS of seismic motion at all frequencies. At the LIGO observatories, the seismic motion has peaks around 0.15 Hz in all three translational degrees of freedom which dominate the differential RMS motion of the ground. The isolation system needs to simultaneously reduce the seismic peak magnitude by at least a factor of five in all three degrees of freedom. At frequencies from 1 Hz to 10 Hz, the isolation system needs to achieve an isolation factor of 1000 to 2000.

Tilt-horizontal coupling is the most challenging problem for low-frequency seismic isolation systems. Tilt-horizontal coupling comes from the principle of equivalence: horizontal inertial sensors cannot distinguish between horizontal acceleration and tilt motion. The magnitude of tilt-horizontal coupling rises very rapidly at low frequencies, and this makes low frequency isolation difficult. A variety of techniques, including sensor correction and sensor blending, are used to address the tilt-horizontal coupling problem. Optimal FIR complementary filters were designed to separate efficiently tilt motion from horizontal acceleration. A nonlinear analysis technique was developed to study the nonlinear tilt-horizontal coupling effect. With these techniques, our prototype vibration isolation systems obtained isolation performance that is very close to the requirement of Advanced LIGO.

Acknowledgements

To Dan DeBra for being my advisor,

to Brian Lantz for being the fearless leader,

to Corwin Hardham for beautiful mechanical designs,

to Norna Robertson, Stephen Boyd and Claire Tomlin for insightful advice,

to Mike Henessey and Jim Perales for being the best technicians,

to the LIGO collaboration and the NSF for generous support,

to my mother Guihua Liu for constant support,

to my dearest wife Xianghui and my most lovely daughter Ashley,

Thank you.

Contents

List of Tables

List of Figures

xiv

Chapter 1

Introduction

1.1 Gravitational Waves

The existence of gravitational waves was first predicted by Einstein in 1916 [16] to provide a causal explanation to the gravitational force exerted by an accelerating mass. By expressing gravitational force with a wave equation, it ceases to act instantaneously, as suggested earlier by Newton, and instead travels at the speed of light.

At this time, gravitational waves have yet to be directly observed, but there has been indirect observations made by Hulse & Taylor [26], Taylor & Weisberg [52] and others. Through careful study of the orbital decay in a neutron star binary system, Taylor & Weisberg found the decay rate to be in excellent agreement with the predicted energy lost to gravitational radiation.

Gravitational waves are differential planar strain waves, meaning that an object subjected to a gravitational wave is alternatingly stretched in one axis while compressed in the orthogonal axis (figure 1.1). The gravitational waves have both a plus, h_+, and cross, $h_\times$, polarization.

The strain ,h, produced by an gravitational wave is tiny: $h \sim r_{s1}r_{s2}/(r_o R)$ where r_{s1} and r_{s2} are the Schwarzschild radii of the masses involved ($r_s = GM/c^2$). The remaining variables are G, the gravitational constant; R, the distance to the source; r_o, the distance between the stars; M, the mass of each star and c, the speed of light.
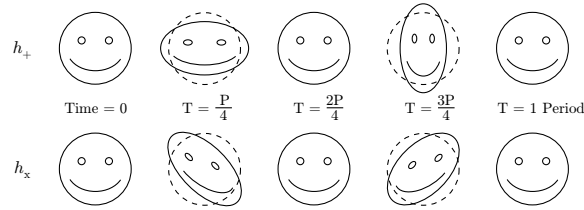
Figure 1.1: The effect of a gravitational wave passing perpendicularly through an object. Note the plus h_+ and cross $h_\times$ polarizations. Courtesy of Brian Lantz.

The ratio of G^2/c^4 is so small that the only measurable sources of gravitational waves are produced by masses on the order of a solar mass or greater.

Despite the need for large masses, there are a variety of sources that may be powerful enough to be detected. A commonly discussed source is the coalescence of two compact objects such as neutron stars or black holes. For an estimate of the strain that these sources would produce on Earth, consider a pair of 1.4 solar mass $(3 \times 10^{30}$ kg) neutron stars located in one of the closest galaxies (in the Virgo Cluster, for example) at a distance R of approximately 15 megaparsec or 4.5×10^{23} meters. Moments before impact these stars may orbit each other at frequencies approaching 400 Hz. The resulting strain on Earth will be approximately 10^{-21} [43].

1.2 Laser Interferometric Gravitational Wave Detection

In spite of the extraordinarily small strain on earth, several methods have been proposed to detect gravitational radiation for astrophysical observation. These include bar detectors which consist of a large suspended mass whose longitudinal flexible mode is at a frequency of about 1 kHz for which there are anticipated gravitational radiation sources.

However, in more recent times, most research effort has been directed toward laser interferometric detectors. Laser interferometry is attractive for gravitational wave detection because of its inherently high displacement sensitivity and the capability

to project light over large distances. The high displacement sensitivity is necessary because of the small displacement produced by gravitational waves on Earth, and since the detection of gravitational waves is based on measuring a strain, the signal is amplified by a large baseline. The Michelson configuration is typical for all detectors, and the fundamental aspects of the interferometer arrangement differ little from the 1887 original. The important distinction for gravitational wave detection is that the mirrors are not connected to a rigid structure. Instead, each mirror is freely suspended to respond to gravitational wave effects. In the event of a gravitational wave, the space between the freely suspended mirrors, or test masses, is stretched much like the smiling face in figure 1.1. The interferometer is sensitive to this distortion and outputs the resulting displacement signal.

Rainer Weiss first proposed a practical interferometric detection scheme in the 1970's [56]. Subsequent to this, several countries have constructed long baseline detectors. A interferometric detector was built by a British-German group known as GEO [45] in Hanover, Germany. The Japanese built a detector with impressive sensitivity for its size called TAMA [53]. There is an Italian/French effort known as Virgo [55]. The Australian group, ACIGA [9], is building a detector in Western Australia .

1.3   LIGO

Laser Interferometer Gravitational-wave Observatory (LIGO) detectors [4], built in the United States, are both larger and more sensitive than any other existing interferometric detectors. There are two LIGO observatories: the LIGO Hanford Observatory (LHO) in Hanford, Washington and the LIGO Livingston Observatory (LLO) in Livingston, Louisiana. Both of these observatories are now operational. The current configuration of each observatory is commonly known as Initial LIGO with the expectation of an Advanced LIGO [18] configuration by approximately 2010. The LIGO observatories consist of two 4 km long beam tubes arranged orthogonally to one another (figure 1.2). Each beam tube contains one arm of a Michleson interferometer with a Fabry-Perot resonant cavity. The end mirrors of the Fabry-Perot cavity are

contained in Beam Splitter Chambers (BSC) at either end of each 4 km long beam
tube. The BSC at the Corner Station houses the beam splitter and the surrounding
Horizontal Access Modules (HAM) contain a variety of support optics for the main
interferometer.
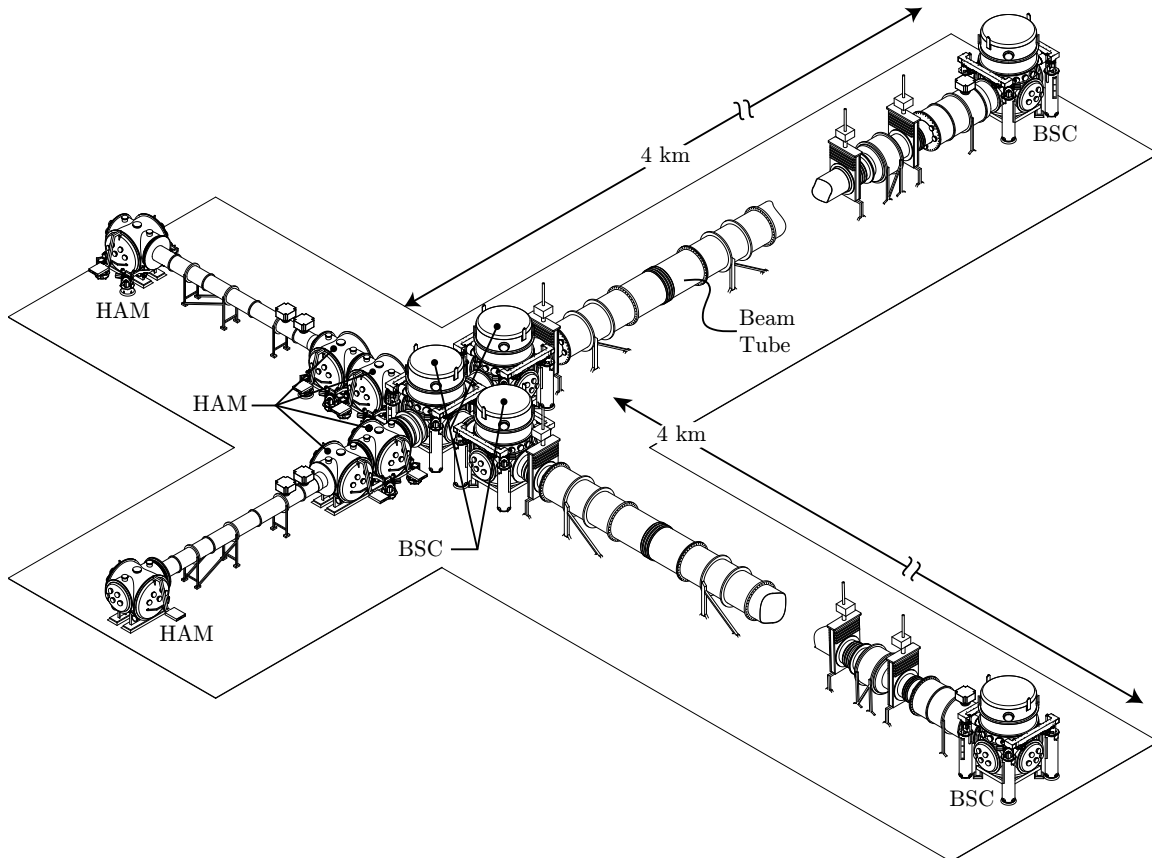
Figure 1.2: The vacuum envelope of the Laser Interferometer Gravitational-wave
Observatory (LIGO). The beam tubes are 4 kilometers long and contain the two axes
of the LIGO interferometer. The test masses are suspended within the Beam Splitter
Chambers (BSC) while the Horizontal Access Module (HAM) chambers contain a
variety of support optics. Courtesy of Oddvar Spjeld.

Initial LIGO is intended to sense gravitational waves at frequencies between 40
and 7000 Hz from sources within 15-20 megaparsecs (1 megaparsec $\approx 3.0 \times 10^{22}$ meters
$\approx 3.0 \times 10^{6}$ lightyears) from the earth. The goal of Advanced LIGO is to increase
the sensitivity of the instrument to distances approaching 200 megaparsecs over a

frequency range of 10 to 10,000 Hz. This translates into a factor of 10 reduction in the strain-equivalent noise floor which requires nearly every aspect of the detector to be improved or replaced with the notable exception of the vacuum envelope. The expected sensitivity of Advanced LIGO is shown in figure 1.3.
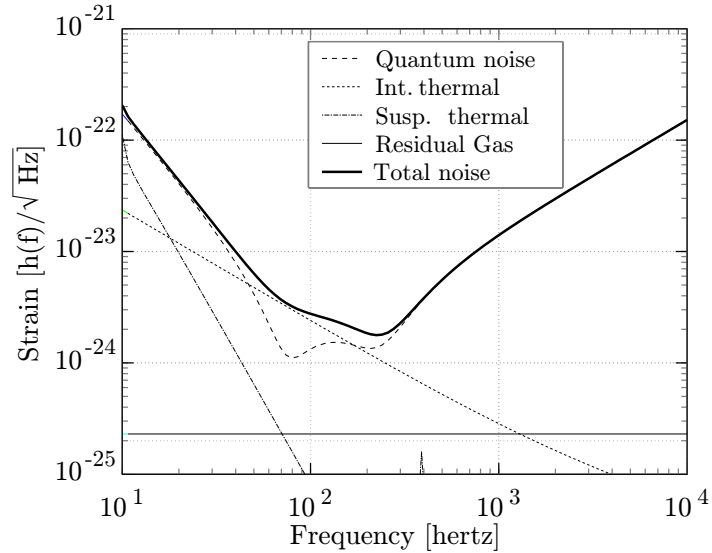
Figure 1.3: Various detector noise sources to the Advanced LIGO strain sensitivity level. Current estimates of the contributions of various detector noise sources to the Advanced LIGO strain (h) sensitivity level. [19]

1.3.1   Vibration Isolation and Alignment of Ligo

For terrestrially rooted gravitational wave detectors, vibration isolation systems are necessary for reducing the coupling from the ground seismic vibration to the motion of the suspended masses.

Ground motion induced vibrations can disrupt the operation of the interferometer and add noise at the low end of the gravitational wave detection band. The sources and magnitude of seismic disturbances vary with frequency (figure 1.6) [1]. Overall, the root-mean-square (RMS) of the ambient ground motion at each site is approximately 1 μm. Much of the spectral contribution to this RMS motion comes from the so-called microseismic peak in the 0.1-0.3 Hz band. The microseismic peak

results from coastal ocean water waves exciting surface waves along the Earth's crust. Another notable disturbance source is human activity which contributes largely between 1 and 10 Hz. This is particularly apparent at the LIGO Livingston Observatory (LLO), where commercial logging in the surrounding forest causes a factor of 10 increase in motion during the daytime. At very low frequencies, the surface of the Earth undergoes a tidal motion on the order of 200 μm peak to peak caused by attraction to the sun and the moon. Seasonal temperature variations may also introduce larger annual length variations [19].

In the presence of these disturbances, suspensions for LIGO must provide both alignment and isolation. Alignment control is important in all degrees-of-freedom (DOF). We have to aim the interferometer beam at the center of the test mass and to control the length between the two ends of each optical cavity. Vibration isolation has to be done both inside and below the detection band of LIGO. In the detection band, isolation is necessary to reduce test mass motion to enable gravitational wave detection. At frequencies below the detection band, vibration isolation is to reduce the RMS motion of the mirrors such that the interferometers can operate in their designed dynamic ranges.

The required vibration isolation performance in terms of isolation factor and the amplitude spectrum density (ASD) of the motion of the suspended mirrors for Advanced LIGO is:

	0.16 Hz	1 Hz	10 Hz
isolation factor	10	1000	10^{10}
ASD (m/$\sqrt{\text{Hz}}$)	2×10^{-7}	10^{-11}	10^{-19}

Table 1.1: Vibration isolation performance required by Advanced LIGO

1.4 Passive and Active Vibration Isolation

The simplest passive horizontal vibration isolation system is a suspended pendulum as shown in figure 1.4 (a). Its transfer function from ground motion $G(s)$ to the

(a) Passive isolation.
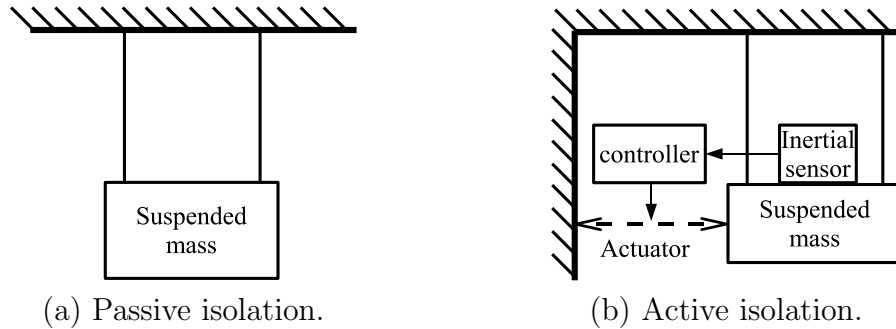
(b) Active isolation.

Figure 1.4: Passive and active vibration isolation systems.

motion of the suspended mass, $x(s)$ is:

$$T_p(s) = \frac{x(s)}{G(s)} = \frac{\omega_0^2 + 2\lambda\omega_0 s}{s^2 + 2\lambda\omega_0 s + \omega_0^2}, \tag{1.1}$$

where λ denotes the damping ratio and ω_0 denotes the natural frequency of the pendulum.

$$\omega_0 = \sqrt{\frac{g}{l}}, \tag{1.2}$$

where g is gravity acceleration on the surface of the earth and l is the length of the simple pendulum. At frequencies above ω_0, the passive isolation system provides isolation factor approximately proportional to frequency squared. For passive isolation systems, equation 1.2 determines the characteristic size of the system. For example, for a passive isolation system that provides isolation at frequencies above 0.1 Hz, the length of the pendulum is at least 25 meters long. One problem associated with a long pendulum is its thermal stability. When the temperature changes, the length of the pendulum changes proportionally to its length, which makes alignment difficult for long pendulums. There are clever ways that one can fold a long pendulum in a compact space, but its thermal stability remains a problem. Another problem associated with a low frequency passive isolation system is stiffness. The stiffness k is given by

$$k = m\omega_0^2. \tag{1.3}$$

Since the stiffness is proportional to ω^2, the low frequency passive isolation system is typically very soft, which makes the alignment between different systems very difficult. In low frequency vertical isolation systems, low stiffness springs have to be used to support the isolated payload with typical weight of several hundred kilograms, which implies the stress level of the springs tends to be high. As a consequence, the creep of the spring could contribute to the vibration noise. Another problem of the high stress springs is that they they might exhibit high nonlinear stiffness [15].
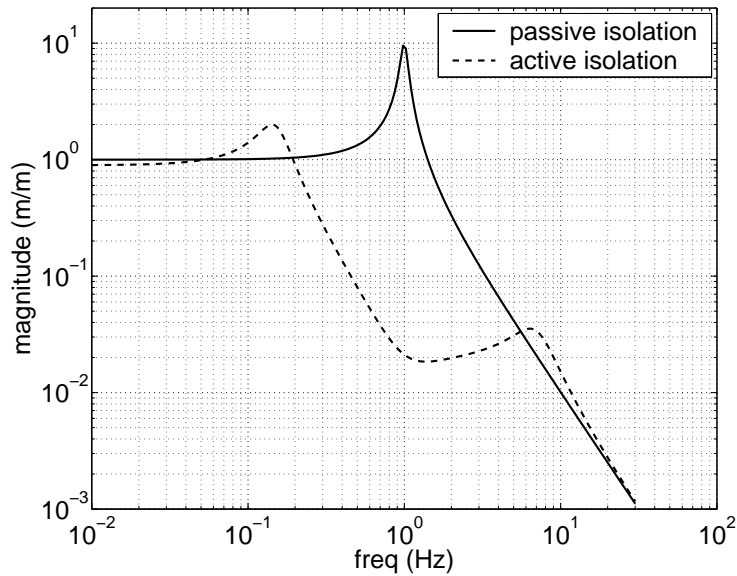
Figure 1.5: Isolation performance of passive and active vibration isolation systems shown in figure 1.4.

We can achieve better isolation performance on the same suspended pendulum by means of active control as shown in figure 1.4 (b). The inertial sensor measures the position of the mass, x, in inertial space. The actuator applies a force between the ground and the mass according to the commands from the controller. The transfer function from the ground motion to the mass motion in the active isolation system is

$$T_a(s) = \frac{T_p(s)}{1 + K_L(s)}, \tag{1.4}$$

$K_L(s)$ denotes the open loop gain of the feedback control system. In the controlled band, i.e. frequencies at which $|K_L(s)| \gg 1$, the active isolation system provides an isolation factor which is approximately $|K_L(s)|$ time larger than that of the passive system. Figure 1.5 compares isolation performance of the active isolation system and the passive isolation system. The active system can give low frequency isolation without lowering the natural frequencies of the system, and thus keep the system stiff. For this reason, sometimes the passive isolation system is called the soft system and the active isolation system is called the stiff system. One problem for the active isolation system is that it depends on the sensitivity of the inertial sensor. One has to find an inertial sensor whose noise level is lower than the motion of the passively isolated mass to further reduce its motion by active feedback.

1.5   Vibration Isolation for Advanced LIGO

The proposed vibration isolation system consists of seven stages as shown in figure 1.7 [1] [2] [42]. From ground, the Hydraulically actuated External Pre-Isolator (HEPI) system [23] is built to attenuate large amplitude disturbances so that systems within the vacuum tank only need to operate about their centered position. Attached to HEPI, a six stage vibration isolation system, including a two stage electromagnetic active vibration isolation system followed by a four stage passive isolation system (also called the quad pendulum) [40], will be built in the vacuum tank. The last four stages of the isolation system are designed to be passive because of the lack of sensors that are sensitive enough to do active isolation. The passive system provides vibration isolation above 1 Hz. Particularly, it needs to provide an isolation factor of 2×10^6 above 10 Hz.

The work discussed in this thesis is about how to build the two stage electromagnetic active system. Its isolation performance required by Advanced LIGO is shown in table 1.2 and in figure 1.6.

	0.16 Hz	1 Hz	10 Hz
isolation factor	10	1000	2×10^3
ASD (m/$\sqrt{\text{Hz}}$)	2×10^{-7}	10^{-11}	2×10^{-13}

Table 1.2: Vibration isolation performance of the active isolation system required by Advanced LIGO
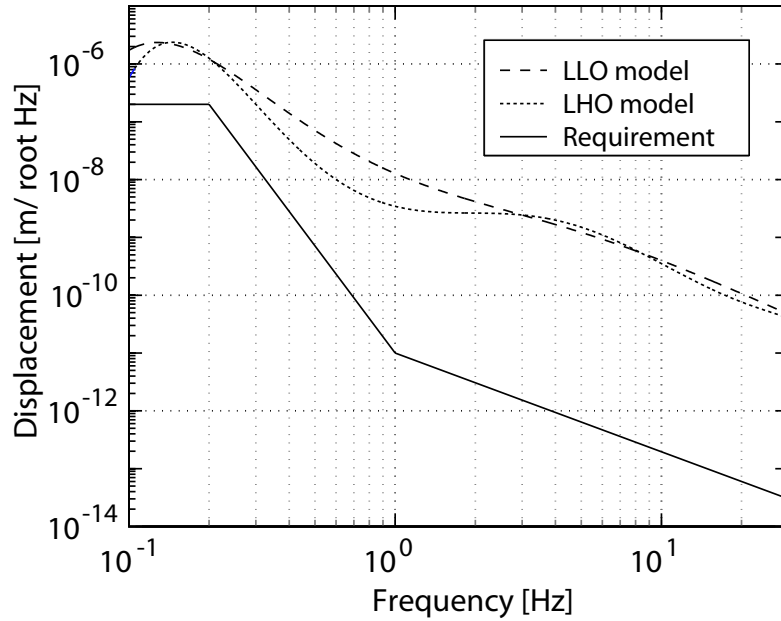
Figure 1.6: Models of the ground motion measured at LLO and LHO and the requirement on displacement noise for the second stage of the two stage active isolation system. [1]

.

1.6 Prior Art

Many vibration isolation systems were designed in the past. They are used in many different areas, including space-based vibration control [49] [21], vibration isolation for the scanning tunnelling microscope [36], the scanning probe microscope [35] and atom interferometric measurements [24].

Gravitational wave detectors require their isolation systems to have much higher
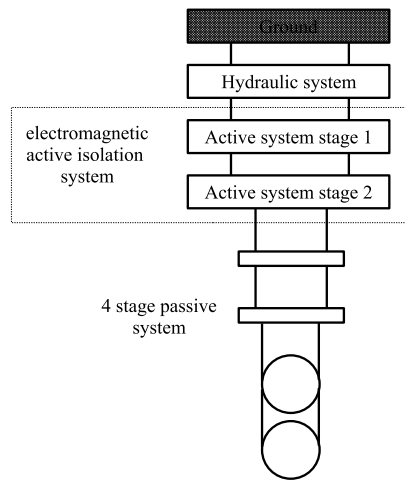
(a) Schematic.
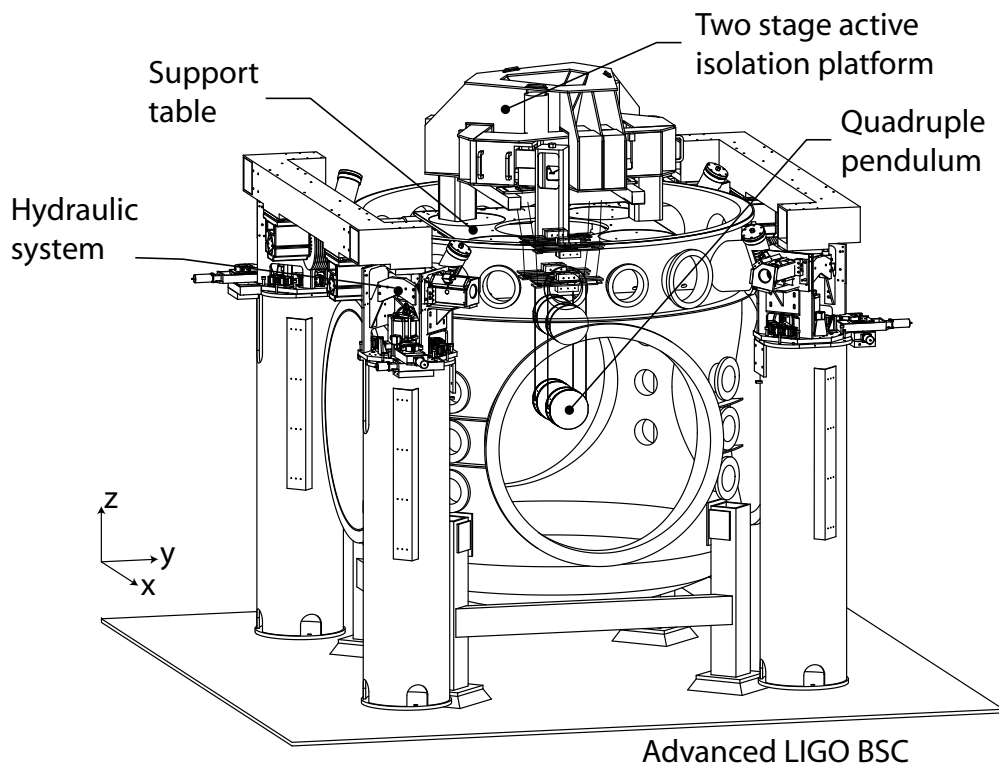
(b) Actual system.

Figure 1.7: The vibration isolation system proposed for Advanced LIGO.
.

performance than most of the previous applications. Many research groups have developed/proposed passive systems to obtain vibration isolation at frequencies starting from 0.1 Hz. David Blair and his group in Australia developed a series of low frequency passive isolation systems using various forms of equivalent long period pendulums, including the Euler buckling spring [58], Roberts linkage [20], and folded pendulum [29]. An X shaped pendulum was developed by Mark A. Barton and his colleagues in Japan [5] [6].

Practical vibration isolation systems have been built for each of the existing gravitational wave detectors. The group in Australia has developed a multistage passive vibration isolation system for ACIGA [28]. Groups in Italy and Japan have developed similar multistage passive vibration isolation systems using inverted pendulums for VIRGO [30] [3] and TAMA [31][50][51]. Recently, Z. Zhou and his colleagues in China have also built a multistage passive system [60]. The vibration isolation systems of the Initial LIGO and the GEO600 is different from the systems above, and do not provide significant vibration isolation below 1 Hz. Initial LIGO uses a multistage passive isolation stack followed by a single pendulum [22]. GEO600 uses a triple pendulum [38].

For Advanced LIGO, active isolation systems are proposed to overcome the problems of passive systems as discussed in the previous section. In fact, active isolation for gravitational wave detection has been proposed and studied for more than 20 years [41] [44]. Particularly, the group in JILA [34] [39] developed an active isolation system that can provide vibration isolation factor of 100 above 1.5 Hz, but it does not provide much isolation at the ground microseismic peak at 0.16 Hz.

1.7   List of Contributions

The rest of the thesis is structured with a set of individual concepts and tools that are used in low frequency vibration isolation system, described in chapter 2 to 6, followed by the experimental results obtained using all these tools together, given in chapter 7. My research contributions includes:

- The study of tilt horizontal coupling problem within the complementary filter

framework using convex optimization (chapter 2 and 4).

- The development polyphase FIR filter algorithm for reducing the number of calculations required for FIR filter implementation (chapter 3).

- The development of a set of linear MIMO transfer function and noise measurement tools. I have measured noise levels of seismometers when the background vibration amplitude spectrum density (ASD) is 5×10^4 times higher than that of the noise (chapter 5).

- The development of MIMO nonlinearity analysis algorithm and its use to study the relationship of nonlinear tilt horizontal coupling and the surface profile of the target plate of the capacity sensors (chapter 6).

- Experimental demonstration of vibration isolation performance (chapter 7):

	0.16 Hz	1 Hz	10 Hz
isolation factor	10	100	1000
ASD (m/$\sqrt{\text{Hz}}$)	10^{-7}	10^{-10}	10^{-12}

Horizontal

	0.16 Hz	1 Hz	10 Hz
isolation factor	10	50	150
ASD (m/$\sqrt{\text{Hz}}$)	10^{-7}	2×10^{-10}	2×10^{-11}

Vertical

Table 1.3: Performance of vibration isolation systems.

Chapter 2

Complementary Filters

2.1 Introduction

In our experiments, we find need to combine information from different sensors together. The complementary filters provide a framework for discussing the combination.

A pair of filters, $(H(s), L(s))$, are called complementary filters if their transfer functions sum to one at all frequencies in a complex sense, i.e. the phase is zero and the magnitude is one.

$$H(s) + L(s) = 1. \tag{2.1}$$

The blending frequency, ω_b, of $H(s)$ and $L(s)$ is defined as the frequency where the two filters' transfer functions have the same magnitude:

$$|H(j\omega_b)| = |L(j\omega_b)|. \tag{2.2}$$

Often, it is desirable to have one of the complementary filters be a high-pass filter and the other be a low-pass filter. For example, the transfer functions of a pair of complementary filters with blending frequency of 1 Hz are shown in figure 2.1. In general, a pair of desired complementary filters should have the following properties.

1. Each filter's transfer function should be close to zero in its stop band;

2. Each filter's transfer function should be close to one in its pass band;

3. The magnitude of the two filters' transfer functions should be limited in the transition bands.
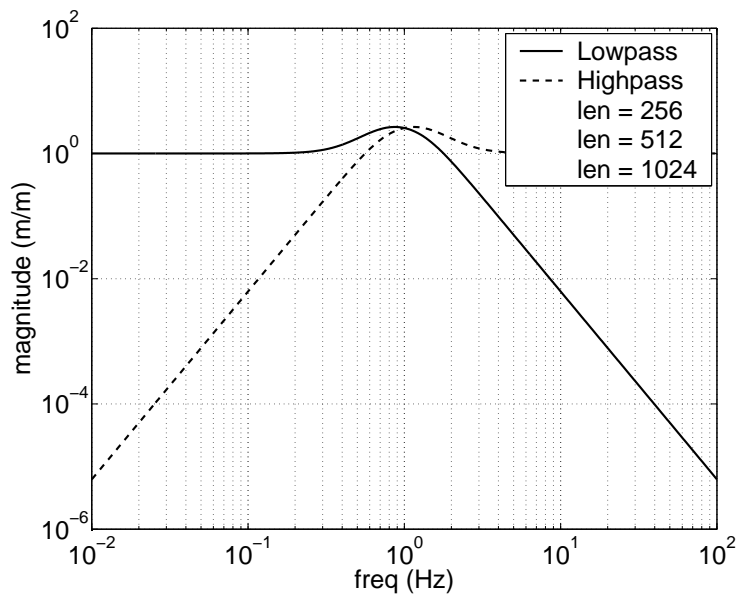
Figure 2.1: A pair of sample complementary filters with blending frequency at 1 Hz.

It is worth mentioning that a similar kind of filter pair, also-called "magnitude complementary filter pair", is widely used in communication systems [54]. The difference between those filters and the filters discussed in this thesis is that the sum of the transfer functions of a magnitude complementary filter pair does not have to have zero phase. In many communication systems, a little bit of time delay will not damage the system's performance much, so some phase lag is allowed in the filters. However, the phase lag could be disastrous for dynamic control systems. Therefore, only strict complementary filters are studied in this thesis.

2.2   Sensor Blending

In dynamic control systems, different sensors are often used to measure the same physical variable in different frequency bands. For example, in a navigation system, a GPS sensor which has good low frequency performance can be used together with a high frequency velocity or acceleration sensor, which can have unbounded position error at low frequencies, to measure the position of vehicle. In that case, complementary filters can be used to combine the signals from those two sensors: filter the signal from the GPS sensor by the low-pass filter and filter the signal from the inertial sensor by the high-pass filter, and then sum the two filter outputs together to generate a "super sensor" signal. Ideally, the super sensor will have superior noise characteristics than either of the sensors alone over all frequencies. This technique is called sensor blending.

In our active vibration isolation system, multiple sensors are used to measure the isolation platform's motion in different frequency bands in each degree of freedom. For example, on the first stage of the rapid double stage active isolation prototype, position sensors are used to measure the platform's motion from zero frequency to about 0.5 Hz. Streckeisen STS-2 seismometers are used at frequencies between 0.5 Hz and 10 Hz, and Sercel L-4C geophones are used at frequencies above 10 Hz. Complementary filters are used to combine the signals from these sensors together.

2.2.1   Effective Noise

Figure 2.2 shows a block diagram of a pair of complementary filters used in a feedback control system. A high frequency sensor and a low frequency sensor are used together to measure the plant variable x. For simplicity, the transfer functions of the sensors, V_H and V_L, are assumed to be 1 in this section. Desirably, the high frequency sensor's noise, N_H is low at the high-pass filter's pass band:

$$|N_H(j\omega)H(j\omega)| < n_c(j\omega), \tag{2.3}$$

where n_c is a certain desired design noise level as a real function of frequency. Similarly, it is desirable to have

$$|N_L(j\omega)L(j\omega)| < n_c(j\omega). \tag{2.4}$$

The transfer function of the super sensor signal is

$$Y_s(s) = X(s)[H(s)V_H(s) + L(s)V_L(s)] + N_H(s)H(s) + N_L(s)L(s) \tag{2.5}$$

Since V_H and V_L are assumed to be 1, the super sensor response function $T_s(s)$ is

$$T_s(s) = H(s) + L(s). \tag{2.6}$$

Given equation 2.1, $T_s(s) = 1$. The noise of the super sensor signal, N_s is defined as:

$$N_s(s) = N_H(s)H(s) + N_L(s)L(s). \tag{2.7}$$

If equation 2.3 and 2.4 are satisfied,

$$|N_s(j\omega)| \leq |N_H(j\omega)H(j\omega)| + |N_L(j\omega)L(j\omega)| < 2n_c(j\omega). \tag{2.8}$$

If input command e is zero, the transfer function of the close-loop platform signal X is:

$$X(s) = \frac{K(s)G(s)H(s)}{1 + P(s)}N_H(s) + \frac{K(s)G(s)L(s)}{1 + P(s)}N_L(s) + \frac{1}{1 + P(s)}N_p(s), \tag{2.9}$$

where $N_p(s)$ is the platform noise, and $P(s)$ is the open-loop loop-gain:

$$P(s) = K(s)G(s)[H(s) + L(s)]. \tag{2.10}$$

In the controlled band, assume $|P(s)| \gg 1$.

$$X(s) \approx \frac{H(s)}{H(s) + L(s)}N_H(s) + \frac{L(s)}{H(s) + L(s)}N_L(s). \tag{2.11}$$
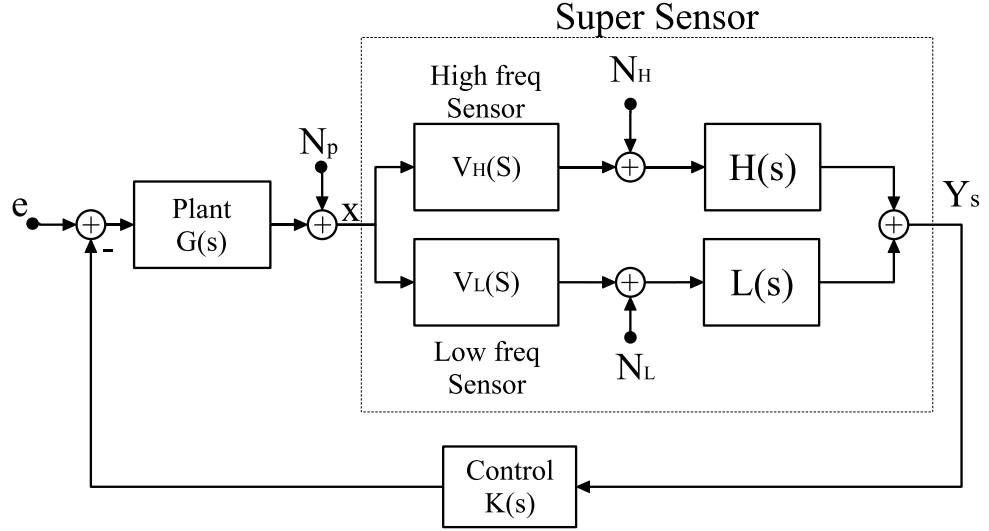
Figure 2.2: A pair of complementary filters used as sensor blending filters in a feedback control system. The overall controller consists of $H(s)$, $L(s)$, and $K(s)$, and it is conceptually divided into blending filters and control filters just to make the design easier.

If equation 2.1 is satisfied,

$$X(s) \approx N_H(s)H(s) + N_L(s)L(s) = N_s(s), \qquad (2.12)$$

which implies that in the controlled band the platform's noise is dominated by the super sensor noise.

2.2.2   Non-Complementary Filters and Stable Normalization

A general pair of stable filters, $(\bar{H}(s), \bar{L}(s))$, are called stably normalizable, if a pair of stable complementary filters can be constructed as:

$$H(s) = \frac{\bar{H}(s)}{\bar{H}(s) + \bar{L}(s)}, L(s) = \frac{\bar{L}(s)}{\bar{H}(s) + \bar{L}(s)}. \qquad (2.13)$$

For notation simplicity, denote the sum of the two original filters as

$$T(s) = \bar{H}(s) + \bar{L}(s). \tag{2.14}$$

It is obvious that the stability of the constructed complementary filters is determined
by the stability of,

$$\frac{1}{T(s)} = \frac{1}{\bar{H}(s) + \bar{L}(s)}. \tag{2.15}$$

The necessary and sufficient condition for equation 2.15 to be stable is: in the Nyquist
plot, $T_s(s)$ does not encircle $(0,0)$ more than once.

    If a general stable filter pair $(\bar{H}(s), \bar{L}(s))$, are stably normalizable, the overall
controller, including blending filter pair $(\bar{H}(s)\bar{L}(s))$, and control filter $K(s)$, in figure
2.3(a), can be converted to the overall controller shown in figure 2.3(b), where com-
plementary filters are used as blending filters. Because $T(s) = \bar{H}(s) + \bar{L}(s)$ has no
zeros or poles that are in the right half plane, there is no unstable pole-zero cancella-
tion introduced in the conversion. If only stably normalizable filters are going to be
used in the control system, the conversion shown in figure 2.3 enables the separation
of the overall controller design into two parts:

1. design the complementary blending filters to minimize the noise of the super
   sensor based on the noise levels of the two original sensors;

2. given the super sensor transfer function is always one, design the control filter
   to handle the stability issues.

2.2.3   System Stability and Sensor Blending Filter Stable Nor-
malization

One might suggest using non-complementary filters for sensor blending and hope to
find filters with better performance within the enlarged design space. However, we
argue that for stable control systems, the benefit of this approach is limited. From
equation 2.10, the sum of the two blending filters contribute directly to open-loop loop
gain $P(s)$. For a stable system, the Nyquist plot of $P(s)$ should not encircle $(-1, 0)$
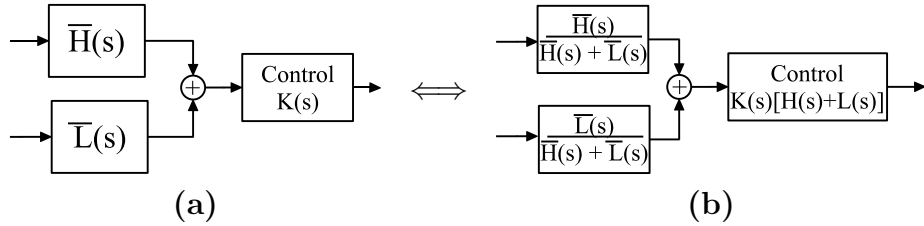
Figure 2.3: Stable normalization of non-complementary filters. If a pair of filters $(\bar{H}(s), \bar{L}(s))$ is stably normalizable, overall controller (a) can be converted to overall controller (b) without introducing nonstable pole-zero cancellation.

more than once. In practical designs, most of the dynamic structures of $\bar{H}(s) + \bar{L}(s)$ lies in the frequency band around ω_b. If $\bar{H}(s) + \bar{L}(s)$ encircles $(0,0)$, it is very likely that it happens in the blending frequency band. To have the benefit of sensor blending, the blending frequency of $\bar{H}(s)$ should be in the controlled band where $|P(s)| \gg 1$. So, if the $\bar{H}(s) + \bar{L}(s)$ encircles $(0,0)$, it is very likely that $P(s)$ encircles $(-1,0)$, which will cause the whole system to be unstable. Hence, in practical stable systems, the blending filter pair $(\bar{H}(s), \bar{L}(s))$ are very likely to be stably normalizable.

2.2.4 Robust Sensor Blending for Sensors with Transfer Function Errors

In section 2.2, the transfer functions of the two sensors are assumed to be exactly one. If a sensor's transfer function is $V(s) \neq 1$, an inversion filter $V^{-1}(s)$ can be used to normalize the sensor's transfer function. There are two possible problems with this inversion process. First, there could be an error in the calibration of the sensor's transfer function. Second, the sensor's transfer function may not be stably invertible. Let $\hat{V}(s)$ denote the invertible nominal transfer function of the sensor after calibration. The leftover error, $V_\delta(s)$, is defined as.

$$V_\delta(s) = 1 - V(s)\hat{V}^{-1}(s). \tag{2.16}$$

In a sensor blending control system, the error in the transfer function of the sensors could cause stability problems. For example, if the high pass sensor's transfer function

is 0.35 rather than 1, the sensor blending control system will not be stable as shown in Figure 2.4. The sum of the high frequency branch , $H(s)V_H(s)$, and the low frequency branch, $L(s)V_L(s)$, has a phase lag of 360 degrees around the blending frequency, which will cause the overall controller to be unstable.

Let $V_{H\delta}$ and $V_{L\delta}$ denote the leftover transfer function errors of the high frequency sensor and the low frequency sensor respectively. The overall transfer function of the super sensor is:

$$W(s) = (1 + V_{L\delta}(s))L(s) + (1 + V_{H\delta}(s))H(s) = 1 + (V_{L\delta}(s)L(s) + V_{H\delta}(s)H(s)) \quad (2.17)$$

The overall error in the super sensor's transfer function, $W_\delta(s) = (V_{L\delta}L(s) + V_{H\delta}H(s))$, could cause the whole control system to be unstable. $W_\delta(s)$ introduces both magnitude and phase errors to the super sensor's transfer function. Practically, because $|W_\delta(s)|$ has maximum around the blending frequency, where the loop gain of the whole system is much larger than one, the phase error is more likely to cause the controller to be unstable. Both the phase error and the magnitude error of $W(s)$ can be bounded by bounding $|W_\delta(s)|$. When $|W_\delta(s)| \leq 1$, the phase error,

$$|P_\delta(s)| \leq \arcsin(|W_\delta(s)|) \quad (2.18)$$

$|W_\delta(s)|$ can be bounded by bounding the leftover errors and the magnitudes of the sensor blending filters:

$$|W_\delta(s)| = |V_{L\delta}(s)L(s) + V_{H\delta}(s)H(s)| \quad (2.19)$$
$$\leq |V_{L\delta}(s)||L(s)| + |V_{H\delta}(s)||H(s)| \quad (2.20)$$

For example, if there is 5% error in the sensors' transfer functions, i.e. $|V_{L\delta}(s)| \leq 0.05$ and $|V_{H\delta}(s)| \leq 0.05$, and the magnitudes of the blending filter are bounded by $H(s) \leq 5$ and $L(s) \leq 5$, we have $|W_\delta(s)| \leq 0.5$, which guarantees that the phase error is less than 30 degrees. Bounding the magnitudes of the blending filters makes the sensing blending control system robustly stable even if there are some small errors in the sensor nominal transfer function.
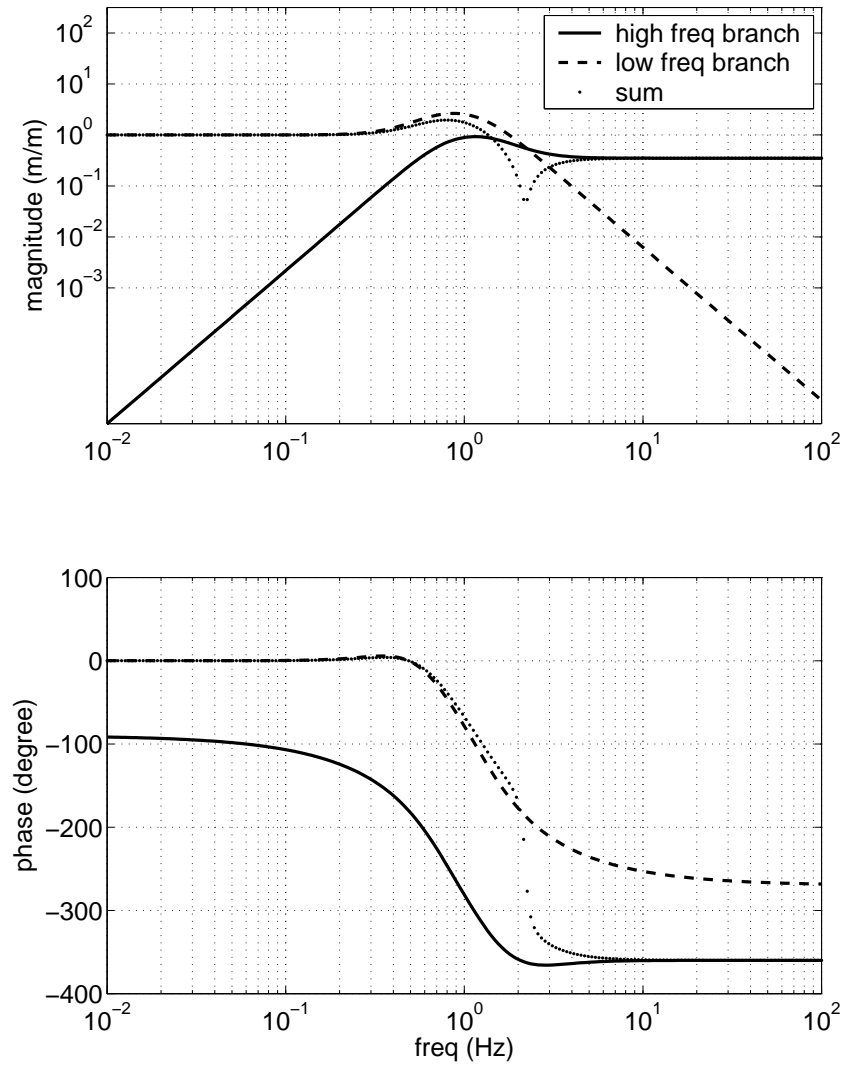
Figure 2.4: Unstable sensor blending. The sum of the high frequency branch and the low frequency branch has a phase lag of 360 degrees, which will cause the control system to be unstable.
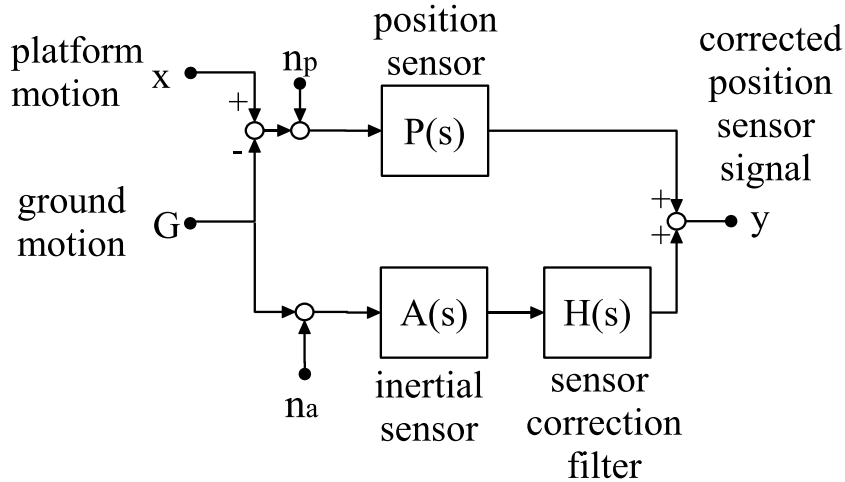
Figure 2.5: Sensor correction.

2.3   Sensor Correction

A similar technique for combining sensors is called sensor correction. For example, in an active vibration isolation system, a relative position sensor can be used to measure the platform's position with respect to the ground. From a different point of view, one can say that the relative position sensor is sensitive to both the platform motion and the ground motion. If an inertial sensor is set up on the ground to measure the ground motion, its signal can be used to cancel out the ground sensitivity of the position sensor. To do so, one has to use a sensor correction filter to match the gains of the inertial sensor and the position sensor in a complex sense, i.e. both magnitude and phase. The sensor correction filter also has to take care of noise. For example, in general, the inertial sensors are noisy at low frequencies. Hence, it is desirable to process the ground inertial signal with a high-pass sensor correction filter which can filter out the low frequency noise. In that case, the high-pass filter in the complementary filter pair can be used as the sensor correction filter.

As shown in figure 2.5, the corrected position sensor signal $y(s)$ is:

$$y(s) = [x(s) - G(s) + n_p(s)]P(s) + [G(s) + n_a(s)]A(s)H(s). \qquad (2.21)$$

For simplicity, assume the transfer function of the sensors are one, i.e. $P(S) = 1$, $A(s) = 1$.

$$y(s) = x(s) + n_p(s) + G(s)[1 - H(s)] + n_a(s)H(s). \tag{2.22}$$

Note that $L(s) = 1 - H(s)$ is the complement of $H(s)$,

$$y(s) = x(s) + n_p(s) + G(s)L(s) + n_a(s)H(s). \tag{2.23}$$

Equation 2.23 show that the error of the corrected position sensor signal is a combination of the sensor noises and the ground motion. The design of our optimal sensor correction filter is a tradeoff between gain match error, $G(s)L(s)$, and noise error, $n_a(s)H(s)$. For example, if the filter gain is one, there is no gain match error. but all the noise will go through the filter and generate a large noise transmission. On the other hand, if the filter gain is zero, no noise can go through the filter but the gain match error is huge. The sensor filter's noise error is determined by the magnitude of its transfer function, while the filter's gain match error is determined by the magnitude of the complement's transfer function. Hence, the sensor correction filter design problem is also a complementary filter design problem, even though only one filter is actually implemented.

2.4 Complementary Filter Design Problem

Both sensor correction filters and sensor blending filters can be design by solving the following problem: find a pair of complementary filters that satisfy:

$$L(\omega) + H(\omega) = 1; \tag{2.24}$$
$$|L(\omega)| \leq \Psi_L(\omega); \tag{2.25}$$
$$|H(\omega)| \leq \Psi_H(\omega); \tag{2.26}$$

Here, ω denotes frequency. Complex functions $L(\omega)$ and $H(\omega)$ are used to denote the transfer functions of the low-pass filter and high-pass filter respectively. $\Psi_L(\omega)$ and $\Psi_H(\omega)$ are known real functions of frequency. In general, the desired complementary

filters are designed by choosing appropriate values of $\Psi_L(\omega)$ and $\Psi_H(\omega)$ and then solving the problem given by equations 2.24 through 2.26.

2.4.1 FIR Complementary Filter

For a finite impulse response (FIR) filter, the transfer function, $Q(\omega)$, is the Fourier transform of its filter coefficients in the time domain, $q(n)$:

$$Q(\omega) = \mathbf{F}(g(n)) = \sum_n q(n)\cos(n\omega) + iq(n)\sin(n\omega) \tag{2.27}$$

The problem given by equations 2.24 through 2.26 becomes finding filter coefficients $l(n)$ and $h(n)$:

$$\sum_n l(n)\cos(n\omega) + \sum_n h(n)\cos(n\omega) = 1; \tag{2.28}$$

$$\sum_n l(n)\sin(n\omega) + \sum_n h(n)\sin(n\omega) = 0; \tag{2.29}$$

$$[(\sum_n l(n)\cos(n\omega))^2 + (\sum_n l(n)\sin(n\omega))^2]^{\frac{1}{2}} \leq \Psi_L(\omega); \tag{2.30}$$

$$[(\sum_n h(n)\cos(n\omega))^2 + (\sum_n h(n)\sin(n\omega))^2]^{\frac{1}{2}} \leq \Psi_H(\omega); \tag{2.31}$$

All variables in equation 2.28 through 2.31 are real numbers. Equations 2.28 and 2.29 are linear functions of variables $h(n)$ and $l(n)$. The left sides of 2.30 and 2.31 are quadrature functions of $h(n)$ and $l(n)$. Hence the problem defined by equations 2.28 through 2.31 is a convex optimization problem (specifically, a convex feasibility problem)[11], which can be solved very efficiently [11].

Note that the convex feasibility problem defined by equations 2.28 through 2.31 is defined in continuous frequency. To solve the problem practically, the frequency needs to be sampled. A set of frequency points $\omega_1, \omega_2,...,\omega_i,...\omega_M$ need to be selected in the frequency band of interest. For each frequency point, ω_i, equations 2.28 through 2.31 have to be satisfied. Hence, the convex optimization problem has $2M$ equality constraints and $2M$ inequality constraints. The method of selecting frequency samples is discussed in the following sections.

$\Psi_H(\omega)$ and $\Psi_L(\omega)$ are the design parameters. In general, the design procedure is:

1. Select desired $\Psi_H(\omega)$ and $\Psi_L(\omega)$ based on practical needs, for example noise levels of different sensors, gain error of different sensors, etc.

2. Solve the convex feasibility problem defined by equation 2.28 through 2.31.

3. If a solution is found, stop. Otherwise, relax constraints defined by $\Psi_H(\omega)$ and $\Psi_L(\omega)$ and repeat step 2.

Because the globally optimized solutions can always be found for the above convex optimization problem, the search for the feasible solution is complete. If there exists an FIR filter pair $h(n)$ and $l(n)$ that satisfies the constraints defined by design parameter $\Psi_H(\omega)$ and $\Psi_L(\omega)$, the convex optimization solver id guarantees to generate the solution of the problem, i.e. the filter coefficients. Otherwise, if there is no feasible solution, the convex optimization solver generates a numerical proof that there is no solution that meets the requirement.

A general linear time invariant complementary filter pair that satisfies equation 2.24 through 2.26 is called a absolute optimal filter pair. The absolute optimal filters could be FIR or IIR filters. If the impulse response time and the sampling frequency of the FIR filter are allowed to approach infinity, the solution of the problem defined by equations 2.24 through 2.26 approaches the absolute optimal filter limit. Hence, if there is enough calculation power to solve the convex problem defined by equations 2.28 through 2.31 for long enough FIR filters, the absolute optimal filters can be approximated.

2.4.2 Simplification of the FIR Complementary Filter Design Problem

To solve the FIR filter design problem of 2.28 through 2.31, it is simplified in the following way.

Take the inverse Fourier transform of equation 2.24,

$$\mathbf{F}^{-1}(H(\omega)) + \mathbf{F}^{-1}(L(\omega)) = \mathbf{F}^{-1}(H(\omega) + L(\omega)) = \mathbf{F}^{-1}(1), \qquad (2.32)$$

which gives

$$l(n) = \begin{cases} 1 - h(n) & \text{if } n = 0; \\ -h(n) & \text{if } n > 0. \end{cases} \quad (2.33)$$

Hence $l(n)$ can be eliminated and the optimization problem becomes: find $h(n)$, such that

$$[(1 - \sum_n h(n)\cos(n\omega))^2 + (\sum_n h(n)\sin(n\omega))^2]^{\frac{1}{2}} \leq \Psi_L(\omega); \quad (2.34)$$

$$[(\sum_n h(n)\cos(n\omega))^2 + (\sum_n h(n)\sin(n\omega))^2]^{\frac{1}{2}} \leq \Psi_H(\omega); \quad (2.35)$$

Because $\Psi_H(\omega)$ and $\Psi_L(\omega)$ can be any arbitrary functions of ω, the design space is huge. The advantage is that there is a lot of flexibility in the FIR filter design. The disadvantage is that it is difficult to search through all possible design parameters in the design space. Hence, it is helpful to search automatically for the best filter in the design space. One can construct the convex optimization problem for variables h, Ψ_H and Ψ_L:

$$\text{minimize: } V(h, \Psi_H, \Psi_L) \quad (2.36)$$

$$\text{such that: } \quad (2.37)$$

$$[(1 - \sum_n h(n)\cos(n\omega))^2 + (\sum_n h(n)\sin(n\omega))^2]^{\frac{1}{2}} \leq \Psi_L(\omega); \quad (2.38)$$

$$[(\sum_n h(n)\cos(n\omega))^2 + (\sum_n h(n)\sin(n\omega))^2]^{\frac{1}{2}} \leq \Psi_H(\omega); \quad (2.39)$$

where, $V(h, \Psi_H, \Psi_L)$ (called value function), is a convex function of h, Ψ_H and Ψ_L. For example, one can chose

$$V = \sum_{\omega_i} [\Psi_L(\omega_i)N_L(\omega_i)]^2 + [\Psi_L(\omega_i)N_L(\omega_i)]^2. \quad (2.40)$$

The convex optimization problem defined by this value function finds the optimal filter that minimizes the total noise of the super sensor.

2.4.3 Example of FIR Complementary Filter Design Using SeDuMi

Design Requirement

In our vibration isolation system, we need a high pass sensor correction filter that has the following properties:

1. Form 0 to 0.008 Hz, the magnitude of the filter's transfer function should be less than or equal to 8×10^{-4}. We chose to have a "flat" magnitude at very low frequencies to avoid numerical problems which will be discussed later in this section.

2. From 0.008 Hz to 0.04 Hz, it attenuates the input signal proportional to frequency cubed. Because the noise level of the horizontal inertial sensor increases very rapidly (proportional to inverse frequency cubed) at low frequencies, we need a powerful high pass filter to get rid of the sensor noise;

3. Between 0.04 Hz and 0.1 Hz, the magnitude of the transfer function should be less than 3. Because the inertial sensor's noise level is low in this frequency band, the filter is allowed to magnify the sensor noise here;

4. Above 0.1 Hz, the maximum of the magnitude of the complement filter should be as close to zero as possible. As mentioned above, the magnitude of the complementary filter determines the amount of gain match error in the sensor correction system. In our system, we would like to have the magnitude of the complementary filter to be less than 0.1. However, to make this problem an optimization problem, rather than a feasibility problem, we construct this problem to automatically search for the best filter that satisfies constraints 1 through 3. If the optimal filter solution does not satisfy the design requirement, i.e. complementary filter's magnitude less than 0.1, it implies that that there does not exist a FIR filter that satisfies all of our design requirements, and the constraints of 1 through 3 need to be loosened. Through this approach, we can

tradeoff between the gain match error and the sensor noise error as indicated by equation 2.23.

Frequency Sampling

The sensor correction filter is designed to have a sampling frequency of 1.67 Hz (sample time is 0.6 second). The length of the filter is 512. How to chose sampling frequencies and filter length will be discussed in later sections. Let us just assume that they are fixed numbers now.

The impulse response of the filter is about 300 second long, which implies the frequency discrimination of this filter is about 0.003 Hz. Hence, in general, the gap between the neighboring frequency samples should be less than 0.003 Hz such that the sampled frequency response can represent the actual transfer function of the filter. On the other hand, the number of frequency samples determines the number of constraints in the convex optimization problem. If there are too many frequency samples, the amount of calculations required to solve the problem becomes impractical.

The filter's transfer function changes dramatically at low frequencies. For example, at 0.008 Hz the upper limit of the magnitude of the transfer function is 8×10^{-4}, but at 0.0016 Hz it becomes 6.4×10^{-3}. Hence, more samples are needed at low frequencies than at high frequencies. For frequencies below 0.04 Hz, the frequency sample rate is 4.06×10^{-4} Hz per sample. For frequencies above 0.04 Hz, the frequency sample rate is 8.12×10^{-4} Hz. The fast changing transfer function at low frequencies can also cause numerical problems for the convex optimization solver program. To avoid those problems, the upper limit of the magnitude of the filters transfer function were kept flat as indicated by the constraint 1.

Quadratic Cone Programming and SeDuMi

A quadratic cone is by defined as

$$\mathrm{Qcone} := \{(x_1, x_2) \in \Re \times \Re^{(N-1)} | \ x_1 \geq \|x_2\|\} \tag{2.41}$$

where $\| \cdot \|$ denotes the Euclidean norm.

$$\|x\| = (\sum_i x_i^2)^{1/2}. \tag{2.42}$$

The quadratic cone is also known as the second order cone or Lorentz cone.

The quadratic cone programming optimization problem is:

$$\text{minimize: } c^T x \tag{2.43}$$

$$\text{such that: } Ax = b, \ x \in \text{Qcone}. \tag{2.44}$$

Its dual problem is:

$$\text{maximize: } b^T y \tag{2.45}$$

$$\text{such that: } c - A^T y \in \text{Qcone}. \tag{2.46}$$

SeDuMi [48] solves quadratic cone programming and its dual problem at the same time, i.e., given vector c, b and matrix A, it generates solution x and y at the same time.

We format our FIR filter design problem to the dual problem. The magnitude constraints can be easily converted into quadratic cone constraints in the format as equation 2.46. For example, inequality constraint 2.31 at frequency ω can be formatted as:

$$\|[\nu_c(\omega); \ \nu_s(\omega)]h\| \leq \Phi_H(\omega) \tag{2.47}$$

where

$$h = [h(0), h(1), ..., h(N-1)]^T \tag{2.48}$$

$$\nu_c = [1, \cos(\omega), ..., \cos((N-1)\omega)] \tag{2.49}$$

$$\nu_s = [0, \sin(\omega), ..., \sin((N-1)\omega)] \tag{2.50}$$

Construct

$$c = [\Phi_H(\omega), 0, ..., 0]^T \tag{2.51}$$

$$A^T = [0, ... ,0; \nu_c(\omega); \nu_s(\omega)] \tag{2.52}$$

and we have

$$c - A^T y \in \text{Qcone.} \tag{2.53}$$

The other constraints can be formatted into Qcone format in similar ways. To convert the convex feasibility problem to a convex optimization problem, introduce a new variable, t, as the maximum gain match error above 0.1 Hz, i.e. the maximum magnitude of Φ_L. The FIR filter design problem is formatted as:

for variable vector $y = [t, h(1), h(2) ,..., h(N-1)]^T$ $\tag{2.54}$

maximize: $-t = [\text{-1 0 0 ... 0}]^T y$ $\tag{2.55}$

such that:

for constants $\omega = 0, 4.06 \times 10^{-4}, ... , 0.008$ Hz :

$\|[0 \ \nu_c(\omega); 0 \ \nu_s(\omega)]y\| \leq 8 \times 10^{-4};$ $\tag{2.56}$

for constants $\omega = 0.008, 0.008 + 4.06 \times 10^{-4}, ... , 0.04$ Hz :

$\|[0 \ \nu_c(\omega); 0 \ \nu_s(\omega)]y\| \leq 8 \times \omega^3;$ $\tag{2.57}$

for constants $\omega = 0.04, 0.04 + 8.12 \times 10^{-4}, ... , 0.1$ Hz :

$\|[0 \ \nu_c(\omega); 0 \ \nu_s(\omega)]y\| \leq 3;$ $\tag{2.58}$

for constants $\omega = 0.1, 0.1 + 8.12 \times 10^{-4}, ... , 0.83$ Hz :

$\|[1 \ 0]^T - [0 \ \nu_c(\omega); 0 \ \nu_s(\omega)]y\| \leq t$ $\tag{2.59}$

Note that when these formulas are applied, the unit of frequency, ω, needs to be converted to radians:

$$\omega \text{ (rad)} = \frac{\omega \text{ (Hz)}}{\text{sample frequency (Hz)}}. \tag{2.60}$$

Results

Totally, there are 513 variables and about 1500 constraints in this convex optimization problem. It takes about 10 minutes for a PC with 1 gigabyte of memory and one Pentium 4 CPU to solve the problem.

Figure 2.7 shows the transfer functions of the FIR complementary filter pair. The high pass filter satisfies all the magnitude constraints at low frequencies. Its complement, the low pass filter, shows that the gain match error is about 0.05 above 0.1 Hz.

Figure 2.6 shows the time domain impulse response of the high pass filter. It looks like the impulse response of a damped oscillator. The oscillation period is about 0.04 Hz to 0.1 Hz, where the transfer function of the filter in the frequency domain has a large overshoot.
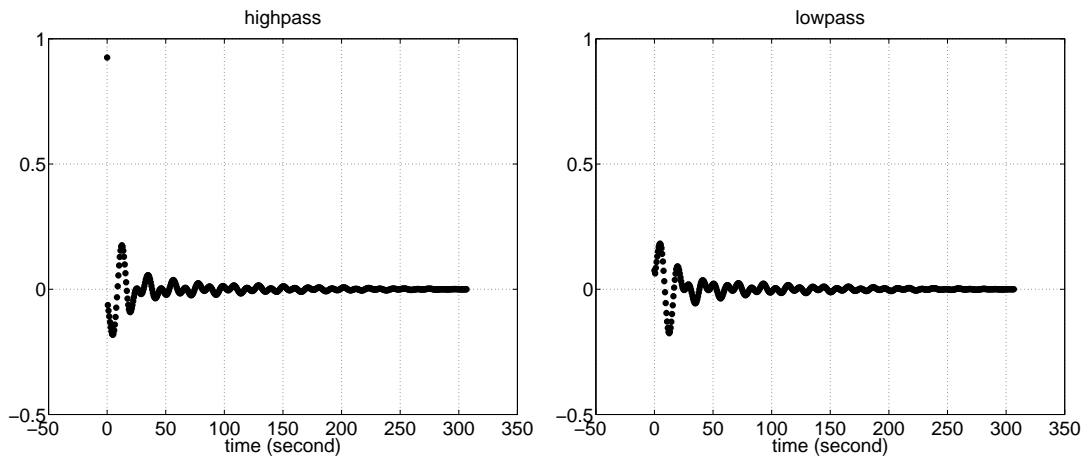
Figure 2.6: Time domain impulse response of the FIR complementary filter pair designed using SeDuMi convex optimization tool.

The Effect of Filter Length and Sampling Frequency of the FIR Filters

The impulse response time of an FIR filter is given by its sample time t_s and its filter length (number of filter coefficients) N.

$$T = Nt_s. \tag{2.61}$$
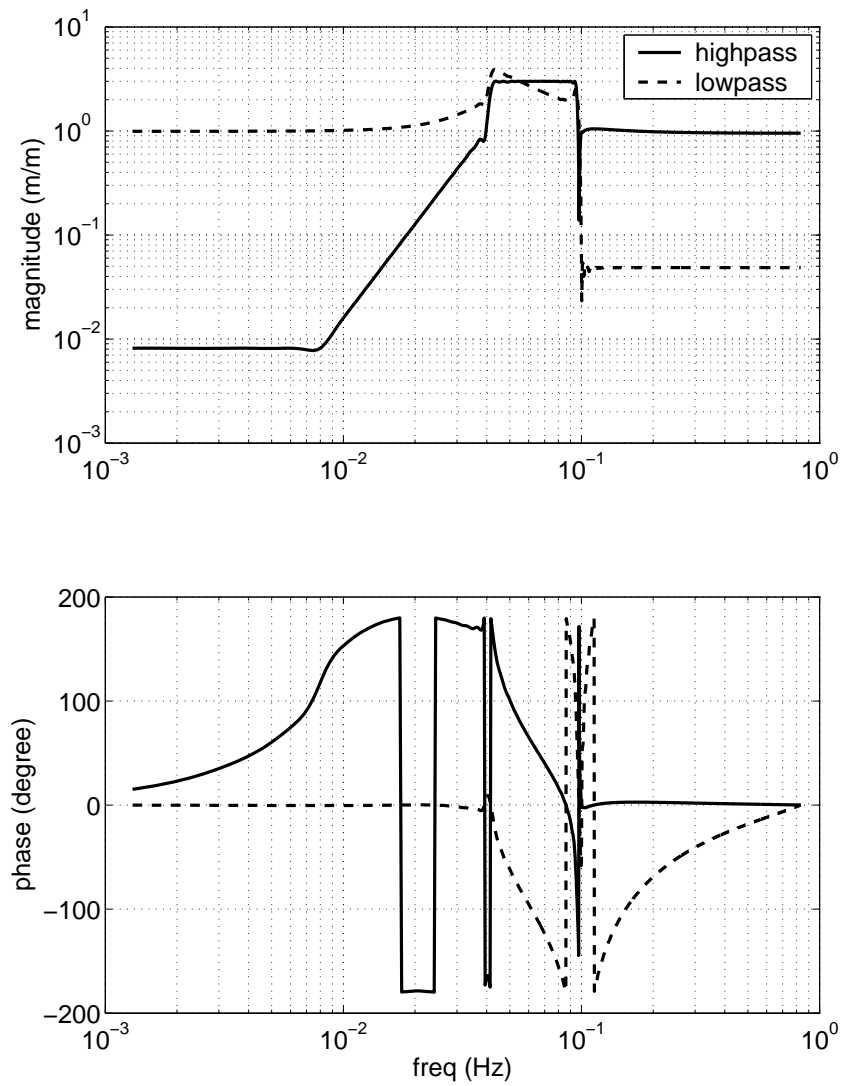
Figure 2.7: Transfer functions of a pair of FIR complementary filters designed using SeDuMi convex optimization tool.

The impulse response time determines its frequency resolution: δf.

$$\delta f = \frac{1}{T}. \tag{2.62}$$

The filters with longer impulse response have better performance, but on the other hand, they requires more calculation to design and to implement. The effect of filter length and sample time on complementary FIR filter performance is studied in this section.

A set of FIR complementary filters are designed with different filter length. All the other design parameters for those filters were kept the same as the previous example. The transfer functions of the complementary filters are shown in figure 2.8. Their time domain impulse responses of the low pass filters of the complementery filter pairs are shown in figure 2.9. In general, filters with more coefficients have better performance, which is measured by the gain match error (magnitude of the low pass filter above 0.1 Hz). Because the sample frequencies were kept the same (at 1.67 Hz), for all these filters, filters with more coefficients have a longer impulse response time, which implies better frequency resolution. As shown in figure 2.8, the filter with 1024 coefficients has much sharper transfer function than the filter with 64 coefficients has. Because the filters with sharper transfer function can make a better use of the frequency band of 0.04 Hz to 0.1 Hz, where overshoot is allowed, they tends to have less gain match error above 0.1 Hz. However, as shown in figure 2.10, when filter length is longer than a certain level, its significance becomes much less. For example, the gain match error of filter with 1024 coefficients is only 5% better than that of the filter with 512 coefficients. This implies that the optimal FIR filter is approaching the absolute optimal filter and that the absolute optimal filter's impulse response after 1024 second is close to zero. In the time domain, all the filters have a similar response in the first several seconds. Another similarity is that all the filter's time response is close to zero at the end. One intuitive explanation of this phenomenon is that the optimization solver tried to avoid a sudden turnoff of the filter's impulse response, because it will cause bad frequency domain behavior. The peak to peak value of the impulse response of the 1024 coefficient filter in the last 200 seconds is less than 2%

of the max peak to peak value, which is also an indication that the optimal FIR filter is approaching the absolute optimal filter.

Another way to change the impulse response time is to change the sample time. The effect of sample time is similar to that of the filter length. The set of transfer functions of the complementary FIR filters are shown in figure 2.11. The time domain impulse response of the low pass filters are shown in figure 2.12. These set of FIR filters with different sample times have the same values of impulse response time as the set of FIR filters with different filter length. Figure 2.13 compares the gain match errors of these two set of filters. The effect of the sample time and filter length are similar, but there are till some realizable difference. For example, the filter with 1024 coefficients and sample time of 0.6 seconds and the filter with 512 coefficients and sample time of 1.2 seconds has the sample impulse response time, but the latter has less gain match error. The reason for this difference can be explained by the frequency domain transfer function. In figure 2.11, the transfer function of the filter with 1.2 second sample time has a peak around 0.83 Hz. Because the sampling frequency of this filter is at 0.83 Hz, the peak comes from the reflection of the filter's transfer function below 0.41 Hz. On the other hand, the transfer function of the filter with 1024 coefficient in figure 2.8 does not have such a peak. Hence, the filter with longer sample time achieves better performance in the range of 0.1 to 0.85 Hz, but the at cost of worse performance at 0.86 Hz. The same theory can be used to explained the other gain error difference between these two different sets of filters. Details of tradeoff between gain match error and the frequency reflection peak will be discussed in the next chapter.

Tradeoff Between Gain Match Error and Overshoot

The convex optimization FIR filter design method can also be used to study the engineering tradeoff between different design parameters. Figure 2.14 shows transfer functions of a set of complementary filters with different magnitude constraint on the highpass filter between 0.04 Hz and 0.1 Hz (also called overshoot). Figure 2.15 shows the relationship between overshoot and gain match error. One can realize that when overshoot is more than 3, its contribution in minimizing the gain match error is not
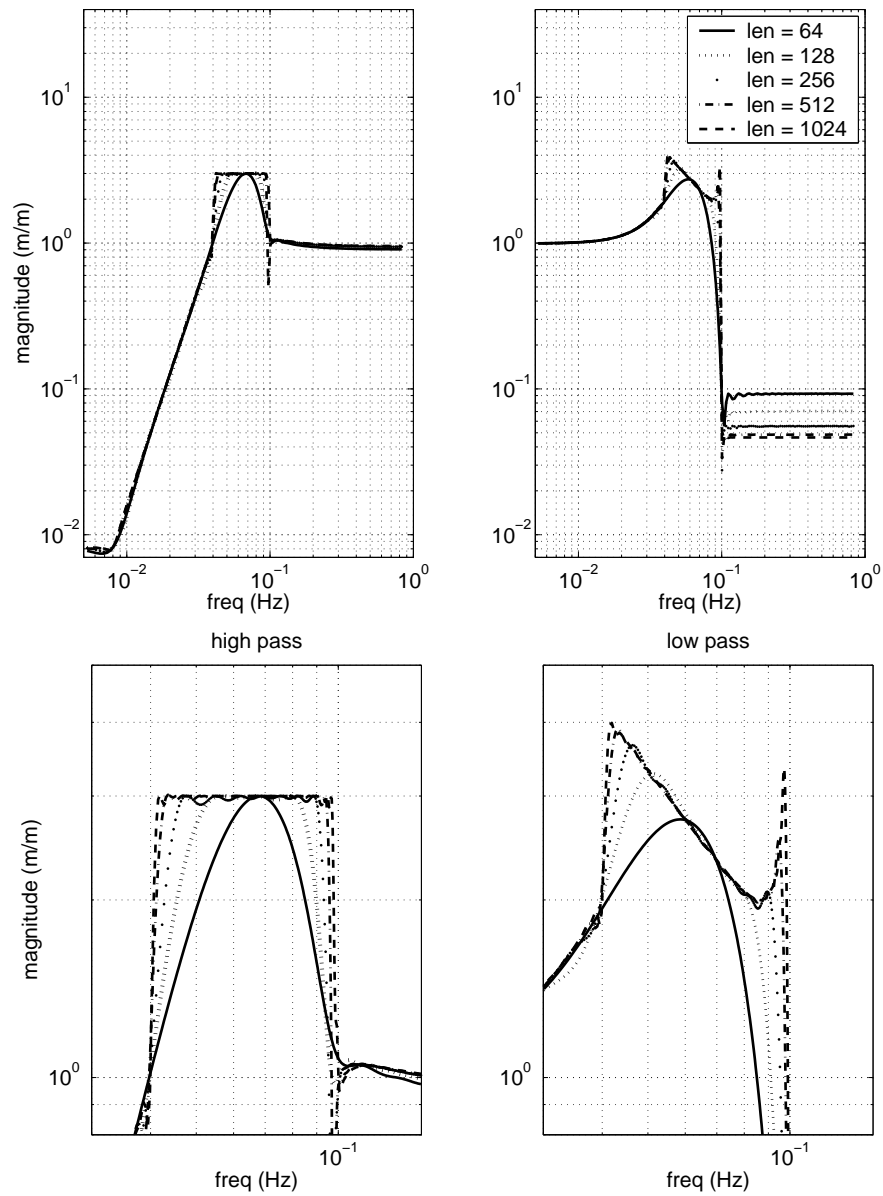
Figure 2.8: Optimal FIR complementary filters for different filter lengths. The details of the transfer function between 0.03 Hz and 0.12 Hz are shown in the lower plots.
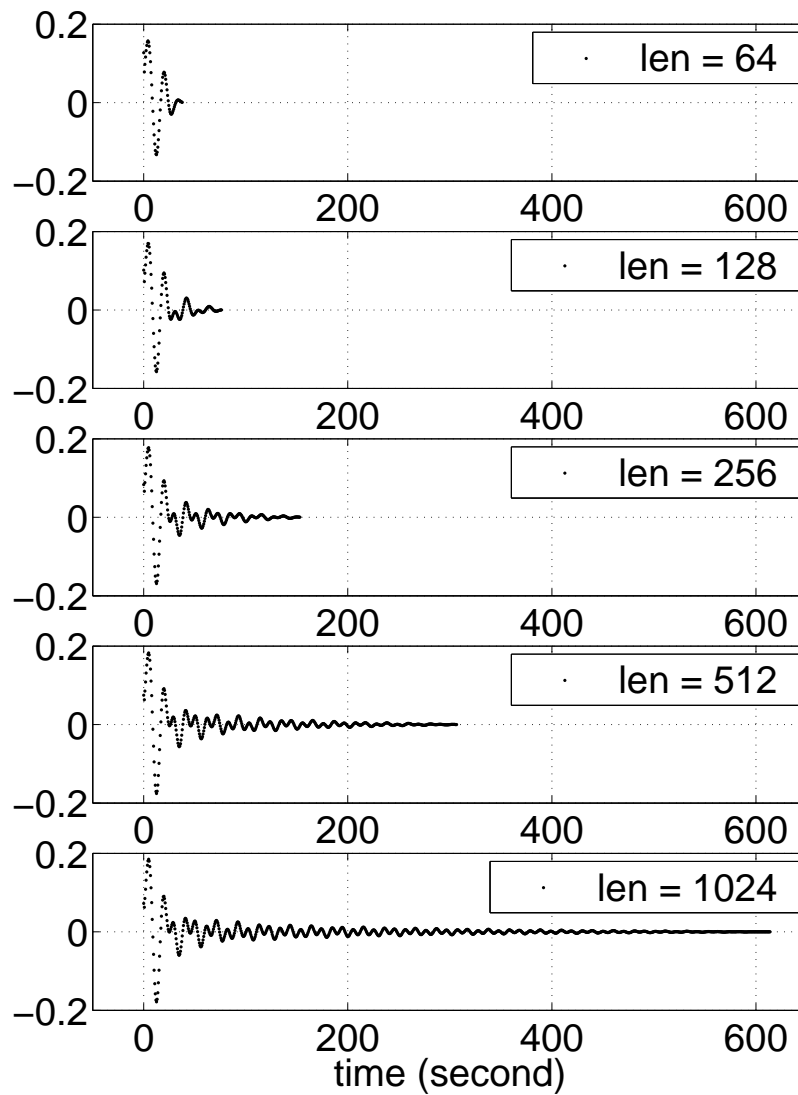
Figure 2.9: Time domain impulse response of the lowpass optimal FIR filters in the complementary filter pairs with different filter length.
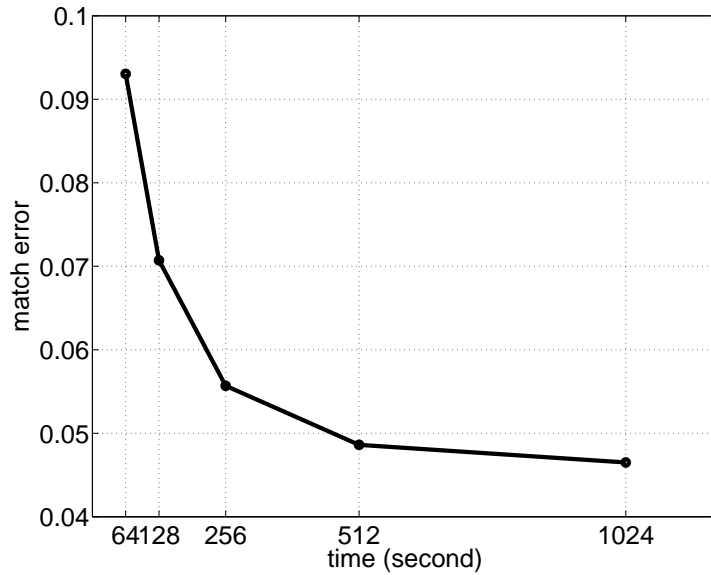
Figure 2.10: Gain match errors (magnitudes of the lowpass filters above 0.1 Hz) as a function of filter length. It seems that after the filter length is longer than some threshold, increasing the filter length does not reduce the gain match error any more.

very significant. For this reason, an overshoot of 3 was chosen for the previous filter.

Changing the Shape of the Gain Match Error

In previous sections the magnitude of the low pass filter above 0.1 Hz is almost constant because the constraint of equation 2.59 is constant with respect to frequency. Filters with different gain error shape can be designed by introducing a shape function to the constrain:

$$\|[1\ 0]^T - [0\ \nu_c(\omega); 0\ \nu_s(\omega)]y\| \leq W(\omega)t \tag{2.63}$$

For example let $W(\omega) = \omega^{-1}$, we can design a filter whose gain match error decreases as the inverse of the frequency. The transfer function of the designed complementary filter pair is shown in figure 2.16
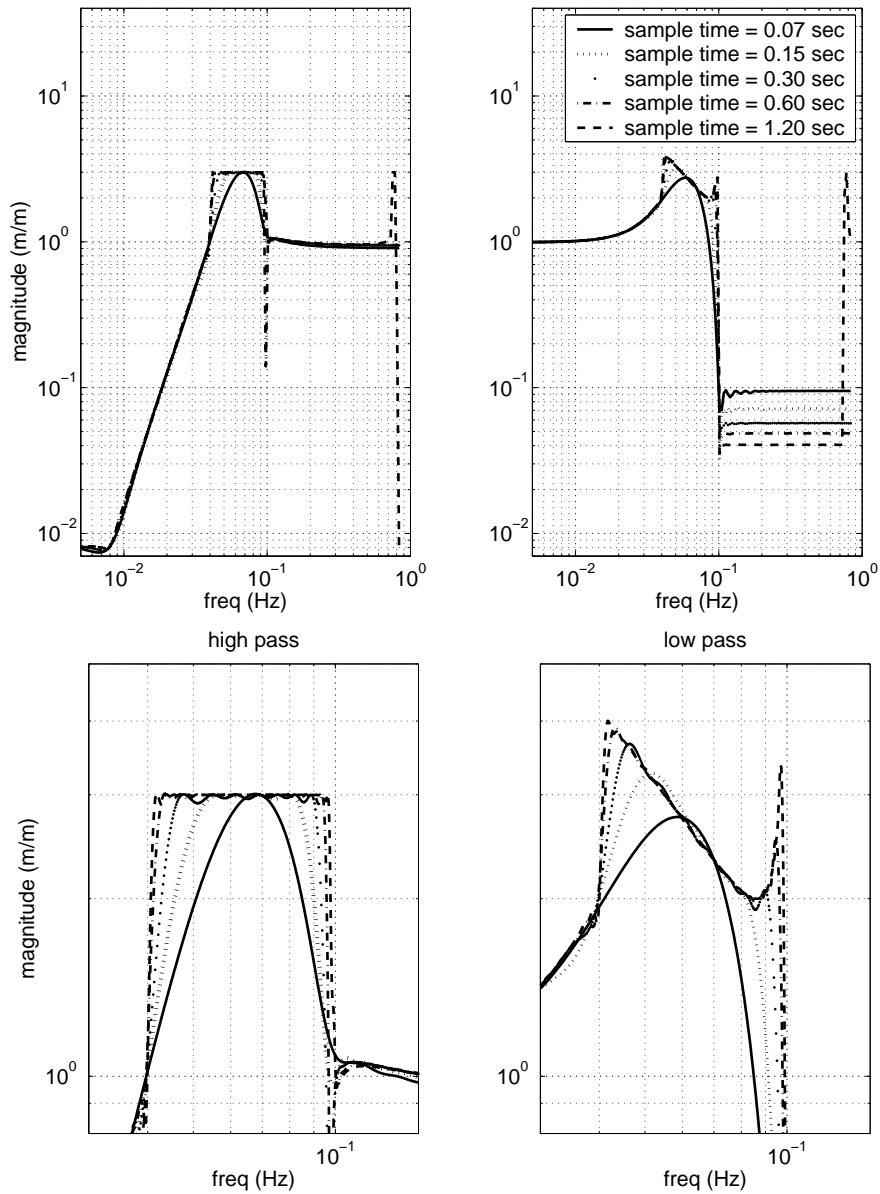
Figure 2.11: Optimal FIR complementary filters for different filter lengths. The details of the transfer function between 0.03 Hz and 0.12 Hz are shown in the lower plots.
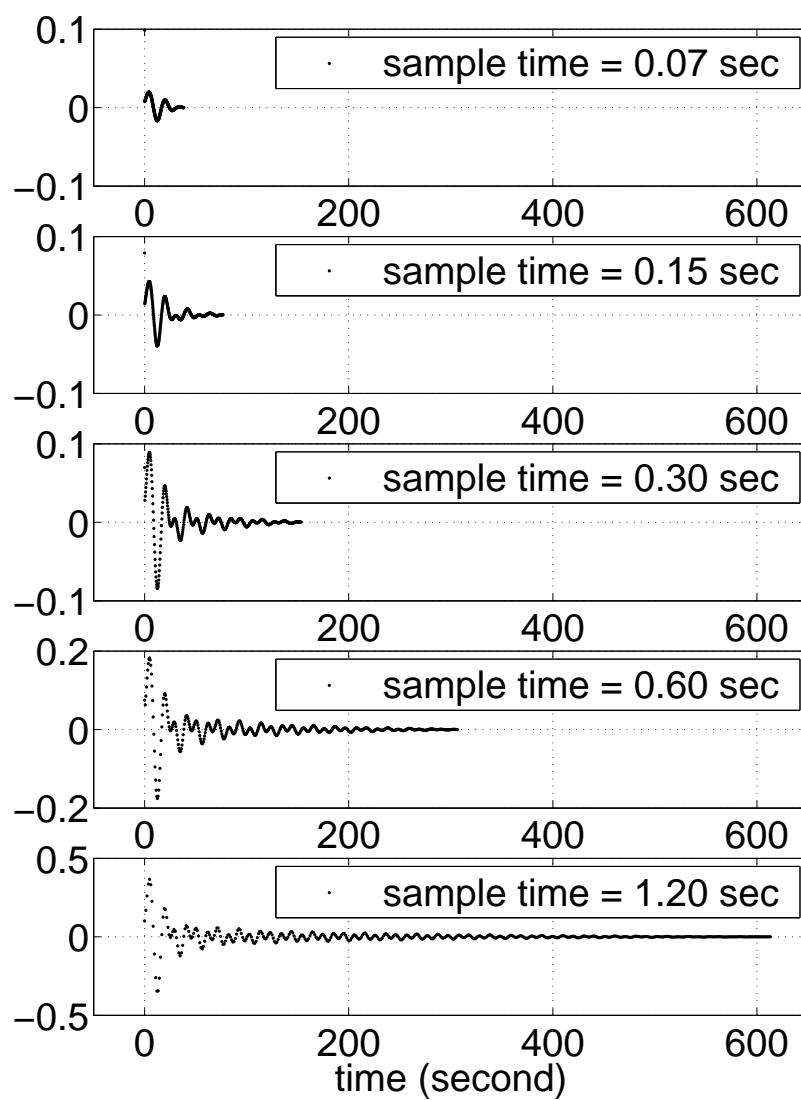
Figure 2.12: Time domain impulse response of the lowpass optimal FIR filters in the complementary filter pairs with different sample frequencies.
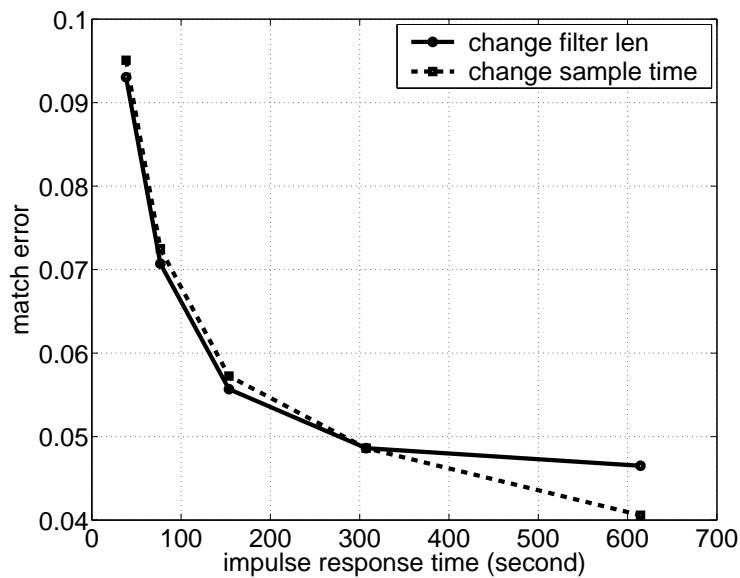
Figure 2.13: Gain match errors (magnitudes of the lowpass filters above 0.1 Hz) as a function of sample time.
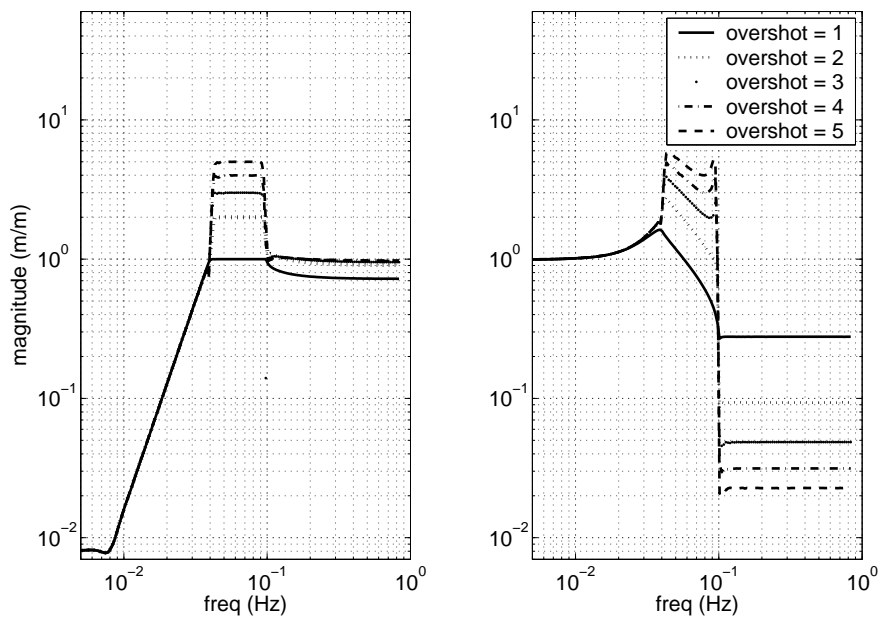
Figure 2.14: The maximum gain match errors (magnitudes of the lowpass filters above 0.1 Hz) as a function of sample time.
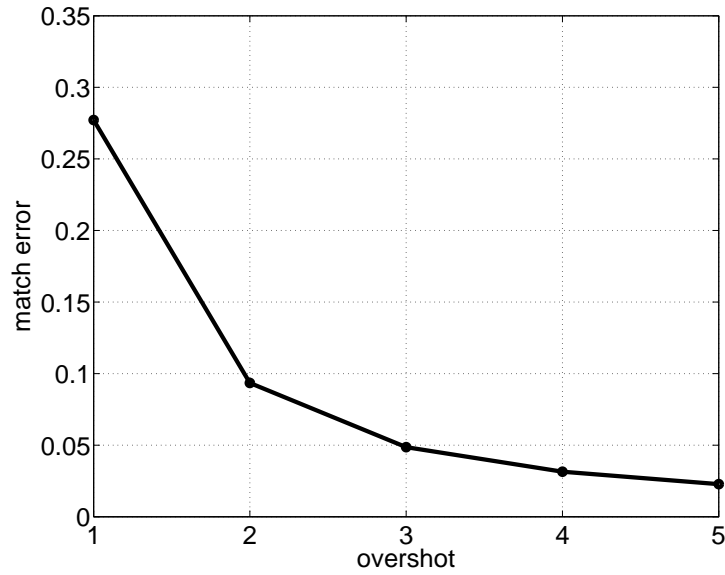
Figure 2.15: Gain match errors (magnitudes of the lowpass filters above 0.1 Hz) as a function of sample time.

2.5 IIR Complementary Filters

For an infinite impulse response (IIR) filter, the transfer function, $K(\omega)$, can also be easily obtained from its time domain numerator coefficients $k_N(n)$ and denominator coefficients $k_D(n)$:

$$K(\omega) = \frac{\sum k_N(n)e^{-in\omega}}{\sum k_D(n)e^{-in\omega}}. \tag{2.64}$$

However, finding $k_N(n)$ and $k_D(n)$ that satisfy equations 2.24 through 2.26 is not a convex problem, and hence very difficult to solve.

For the most of the IIR complementary filters used in this thesis, they are designed using the following procedure:

1. Design a pair of desired highpass and lowpass filter.

2. Check to make sure that the sum of these two filters is invertible.

3. Normalize the two filters such that they are complementary.

For example, the filter shown at the beginning of this chapter in figure 2.1 is
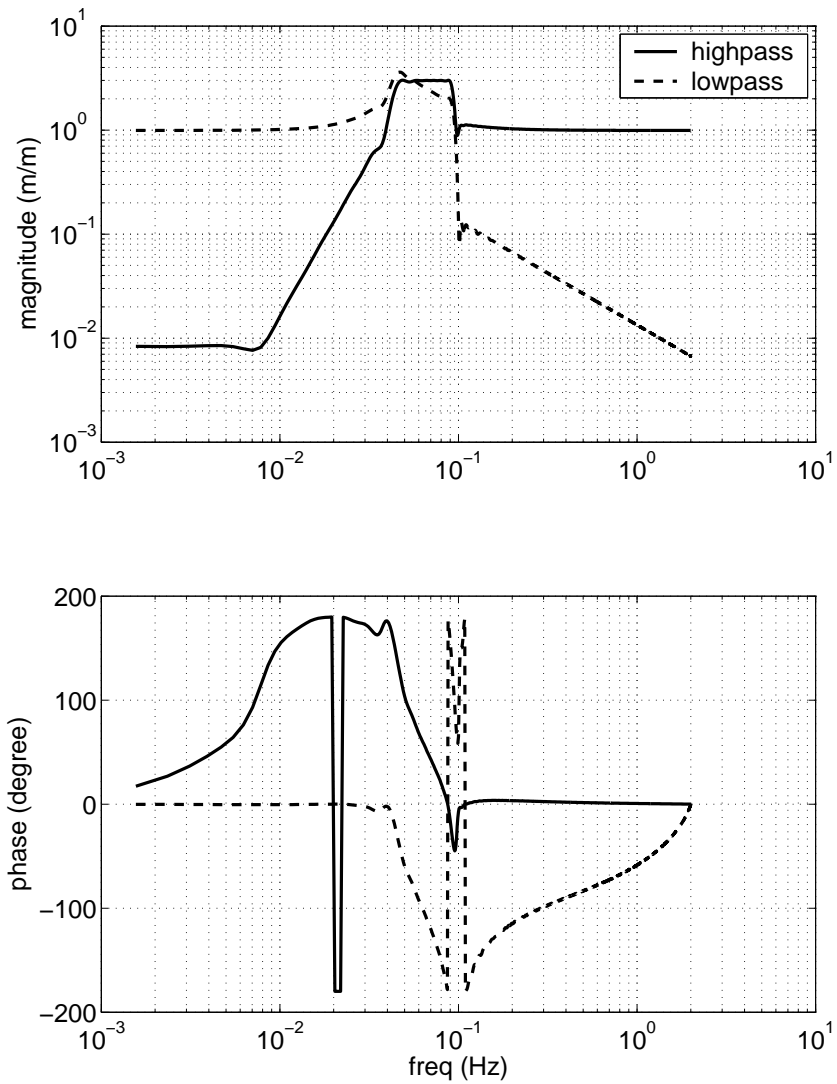
Figure 2.16: Complementary filter with the gain match error (magnitude of the low pass filter at high frequencies) decreases as the inverse of the frequency.

designed by normalizing the highpass filter and the lowpass filter shown in figure 2.17. The transfer function of the sum does not have overall phase lag, so it is invertible.

2.6 Summary

Because the IIR complementary filters can only be designed by trial and error, their performance is not as good as the optimal FIR filters. Figure 2.18 shows the difference of the optimal FIR filters and a typical IIR filter designed using the above procedure. The FIR filter and the IIR filter have similar overshoot and gain match error (at 0.16 Hz), but the FIR filters have much better low frequency performance.

The difference between FIR and IIR complementary filters is summarized in table 2.1.

	FIR	IIR
design	convex, easy	non-convex, difficult
implementation	complex	simple
computation	much	little
performance	great	ok

Table 2.1: Comparing FIR and IIR complementary filters.
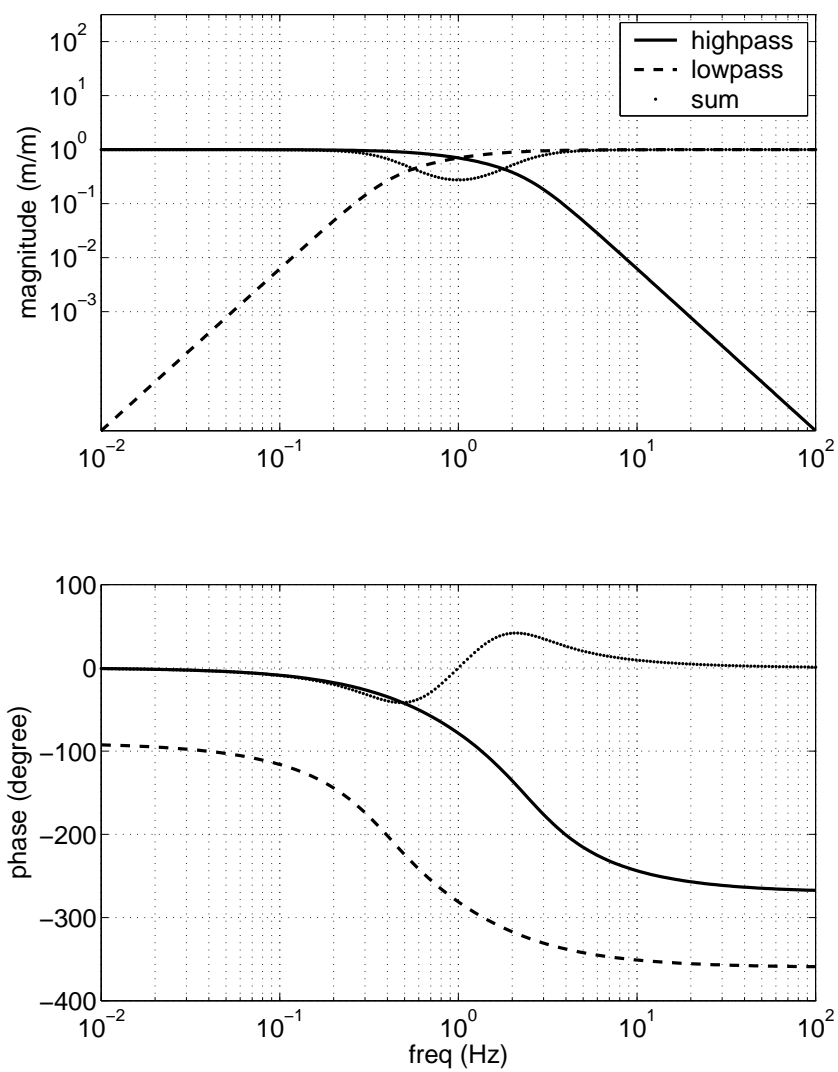
Figure 2.17: Complementary IIR filters can be constructed by normalizing a pair of IIR filters. The transfer function of the sum does not have overall phase lag, so it is invertible.
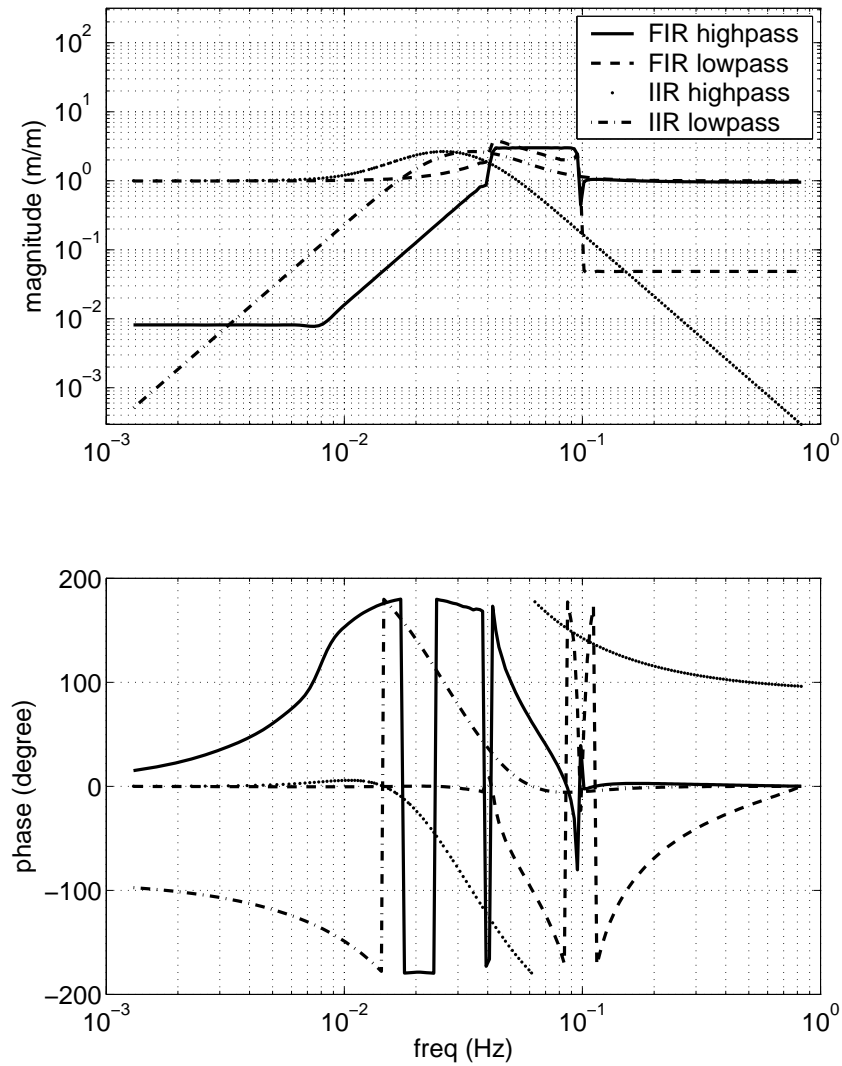
Figure 2.18: Compare the performance of FIR and IIR filter. The FIR filter and the IIR filter have similar overshoot and gain match error (at 0.16 Hz), but the low frequency performance is very different. The sharp noise reduction of the FIR filters is essential for the low frequency isolation systems.

Chapter 3

Polyphase FIR Filter Implementation

3.1 Introduction

In chapter 2, it is shown that FIR complementary filters have superior performance than the IIR filters. However, the amount of calculations required to implement the FIR filters is too large to be practical if they are implemented in the traditional way with today's computer technology.

In a standard FIR filter with filter coefficients q, at each time step, the output, y, is calculated from the input, x, by

$$y(n) = \sum_{m=0}^{N-1} q(m)x(n-m). \tag{3.1}$$

So, at each time step, $2N(N$ multiplications and N additions) FLoating Point Operations(FLOPs) need to be calculated. Hence, the number of FLOPs per second (FLOPs/sec) for a FIR filter with sampling frequency f_s is

$$\mathcal{N} = 2Nf_s. \tag{3.2}$$

From chapter 2, it is known that to obtain a sharp transition between a stop-band

49

and pass-band for FIR filters, the filter has to have high frequency resolution, which is determined by the filters impulse response time T. Since

$$T = \frac{N}{f_s},\tag{3.3}$$

we have

$$\mathcal{N} = 2Tf_s^2.\tag{3.4}$$

In our vibration isolation system prototype, the sampling frequency of the digital control system is at 2500 Hz. If a FIR filter with 300 second impulse response time is implemented directly, the required FLOPS is 3.75×10^9 operations per second, which is too large for most processors today.

3.2   Down Sampling

To reduce the FLOPs/sec for FIR filters, the sampling frequency of the low pass FIR filters can be reduced by down sampling as shown in figure 3.1. The down sampling block with down sampling ratio of D just select one data sample from every D data samples from the incoming data stream and send it to its output and throws the rest of the data points away. The up sampling block does the opposite, it interpolates zeros inbetween the input data points and then sends them to output. [54].

A low pass anti-aliasing filter is used before the down sampling to reduce the amount of high frequency signals aliased to the low frequencies when the signal is down sampled. Similarly another low pass interpolation filter is used to avoid the low frequency signal from aliasing to the high frequencies. The introduction of the anti-aliasing filter and the interpolation filter has two effects on the FIR filter. First, they reduce the aliasing noise of the filter. Second, they contribute to the overall transfer function of the whole filter. Figure 3.2 shows a low pass filter with cutoff frequency of 0.5 Hz. In the following examples in this section, this filter is used as both the anti-aliasing filter and the interpolation filter in a down sampling FIR filter system with the original FIR filter shown in figure 2.7.
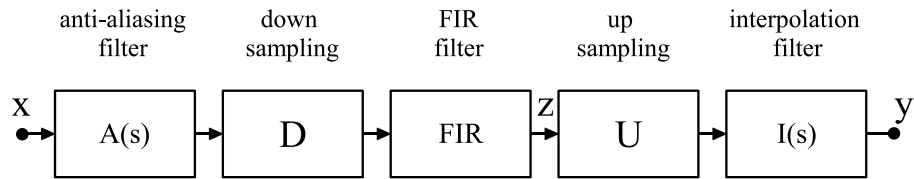
Figure 3.1: To reduce the number of floating point calculation per second (FLOPS) by reducing the sampling frequency of the FIR filter. An anti-aliasing filter is used before down sampling to reduce the amount of high frequency signals aliased to the low frequencies when the signal is down sampled. Similarly an interpolation filter is used to avoid low frequency signal to alias to high frequencies.
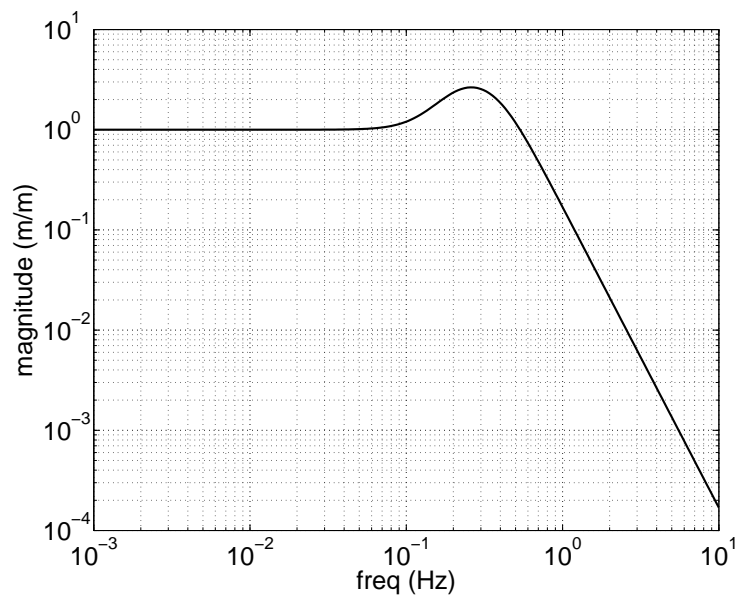
Figure 3.2: Low pass filters with cutoff frequency of 0.5 Hz, as an example of the anti-aliasing filter or interpolation filter in figure 3.1.

Let D denote the down sampling ratio between the sampling frequency of the outside digital system f_{s0} and the sampling frequency of the FIR filter f_s. Suppose the input signal (in the frequency domain) is $x(f)$, the aliasing noise due to down sampling of the signal before entering the FIR filter between zero frequency and $f_s/2$

is

$$x_{Dn}(f) = \sum_{d=1}^{D} x(df_s - f)A(df_s - f), \tag{3.5}$$

where $A(\cdot)$ denotes the frequency response of the anti-aliasing filter. If the amplitude spectral density (ASD) of the input signal is assumed to be 1 m/$\sqrt{\text{Hz}}$, and the low pass filter shown in figure 3.2 is used as the anti-aliasing filter, the ASD of different aliasing components are shown in figure 3.3. Because $A(s)$ is a low pass filter, the first term in the summation of equation 3.5 dominates the down sampling noise. To reduce the down sampling noise, we need to increase the sampling frequency of the FIR filter or to decrease the cutoff frequency of the anti-aliasing filter.
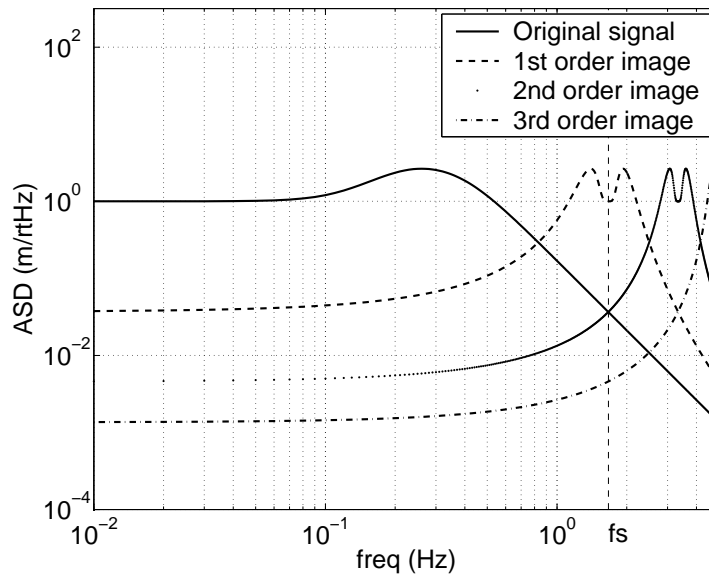
Figure 3.3: Signal aliasing due to down sampling. The signal coming out of the anti-aliasing filter is shown as the original signal. The sampling frequency of the FIR filter, f_s, is 1.67 Hz. The high order aliasing components contributes to the down sampled signal between zero and $f_s/2$. The down sampling aliasing noise is about 1% in this plot.

Similarly, up sampling aliasing noise is introduced to the signal when the output of the FIR filter is interpolated to match the sampling frequency of the outside digital

system. If the output signal of the FIR filter is $z(f)$ at frequencies between 0 and f_s, the signal after up sampling and interpolation filtering is:

$$y(f) = z(mod(f, f_s))I(f), \tag{3.6}$$

where $I(\cdot)$ denotes the frequency response of the interpolation filter and $mod(\cdot, \cdot)$ is the modular function defined as

$$mod(a, b) = a - nb, \ n \text{ is the largest interger that satisfies } n \leq \frac{a}{b}. \tag{3.7}$$

If the ASD of the input of the FIR filter is assumed to be 1, the ASD of the output of the interpolation filter is shown in figure 3.4. The aliasing noise introduced by down sampling and up sampling appears as sensor noise in the sensor blending and sensor correction systems. Hence, the aliasing noise directly contributes to the platform noise of the controlled system. It also needs to be realized that the aliasing noise is not independent of the sensor signal, too much aliasing noise could cause the control system to become unstable. In the vibration isolation system design requirement for Advanced LIGO, the ASD of the motion of the controlled platform should be 10^{-11} m/$\sqrt{\text{Hz}}$ at 1 Hz. However, the ground motion is about 10^{-6} m/$\sqrt{\text{Hz}}$ at 0.16 Hz. This implies the up sampling aliasing from 0.16 Hz to 1 Hz should be 10^{-5} times smaller than the signal at 0.16 Hz. Obviously, the performance of the example shown in figure 3.4 will not meet the requirement. Hence if the down sampling FIR filter is used in the vibration isolation system for Advanced LIGO, either the sampling frequency f_s needs to be increased, or the cutoff frequency of the interpolation filter needs to be decreased.
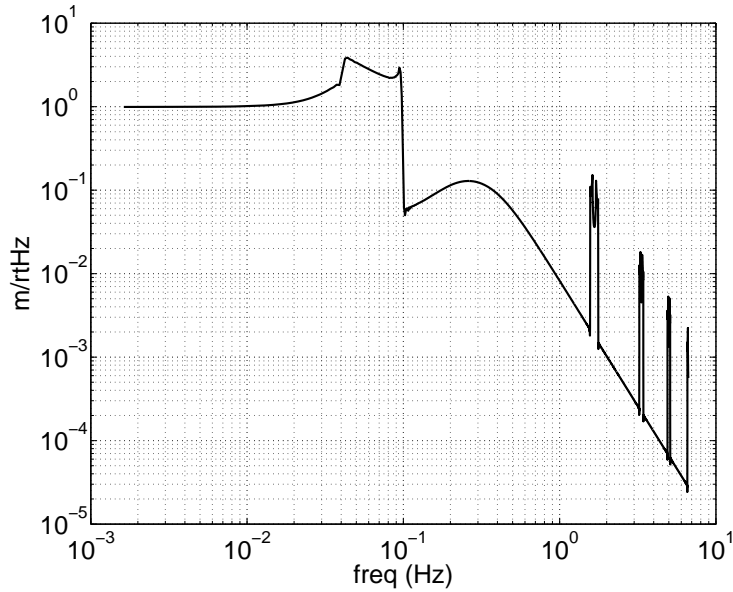
Figure 3.4: Signal aliasing due to up sampling.

At frequencies between 0 to f_s, the anti-aliasing filter and the interpolation filter contribute to the transfer function of the overall down sampling FIR filter system, which could degrade the performance of the overall FIR filter. For example, the transfer functions of a down sampling FIR complementary filter pair is shown in figure 3.5. The gain match error of the overall high pass filter is about 9 times larger than that of the original filter at 0.3 Hz. If this filter is used as the sensor correction filter, the isolation performance will not meet LIGO's requirement. To address the problem for down sampling FIR filters, we need to increase either the sampling frequency of the FIR filter or the cutoff frequencies of the anti-aliasing filter and the interpolation filter.
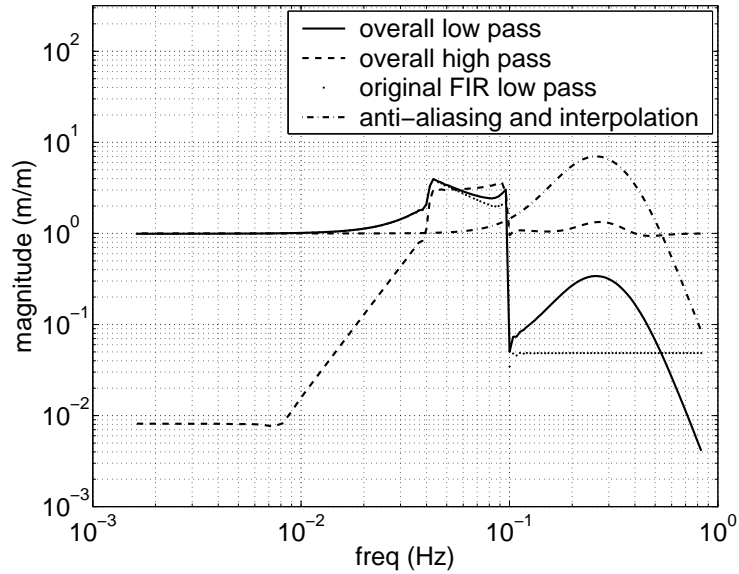
Figure 3.5: The anti-aliasing filter and interpolation filter contributes to the transfer function of overall down sampling FIR filter system. As result, the gain match error of the overall high pass filter is about 9 times larger than that of the original filter at 0.3 Hz.

In conclusion, in a down sampling FIR filter system, if the sampling frequency of the FIR filter is fixed, the cutoff frequencies of the anti-aliasing filter and the interpolation filter determines the tradeoff between signal aliasing noise and transfer function error. In our examples in this section, these two problems can not be solved at the same time unless the sampling frequency is dramatically increased. However, increasing the sampling frequency will cause two other problems. First, the run time FLOPS will increase proportional to f_s^2. Second, the number of coefficients in the FIR filter will increase proportional to f_s, which will cause the FLOP used to solve the FIR filter design problem to increase proportional to f_s^3. Either of the these problems could make the design impractical.

3.3   Polyphase FIR Filter Implementation

A technique called polyphase FIR filtering, as shown in Figure 3.9, is designed to reduce the the calculation load of traditional down sampling FIR filters. The incoming data stream is divided into m sub-streams by a cyclic distributer according to the data samples' arrival time. Hence, each sub-stream has the sample rate of f_s/m (in Figure 3.9, $m = 3$). The FIR filters on each sub-stream are identical traditional FIR filters which work at frequency $f_f = f_s/m$. At each time step, the cyclic collector picks up an output sample from the FIR filter that is working in that phase and sends it to the output. Hence, the output sample rate is f_s, which is the same as the input sample rate.
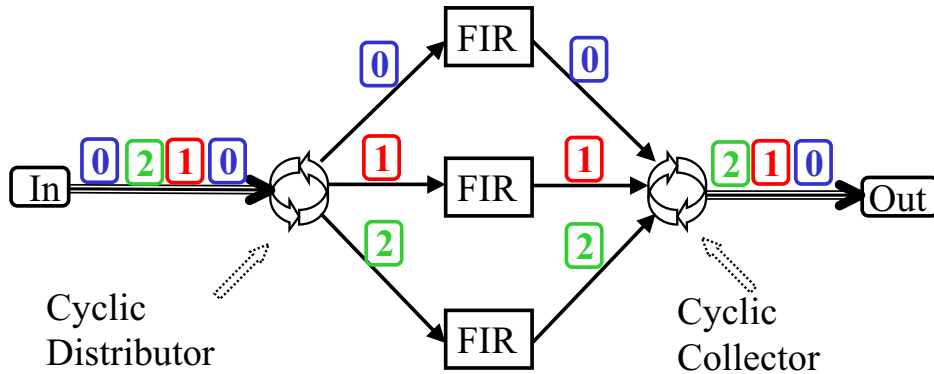
Figure 3.6: Polyphase FIR filter implementation. The three FIR filters have identical filter coefficients and each operates at frequency f_f, but are offset in phase. The cyclic distributor distributes the incoming data samples to different FIR filters according to the samples' arriving time phase. At each time step, the cyclic collector picks up an output sample from the FIR filter with the appropriate phase and sends it to the output. Hence, the overall sampling frequency is $f_s = m \cdot f_f$, where m is the number of cyclic phases.

The total amount of calculation that is required by the polyphase FIR filter is given by the total of m parallel FIR filters:

$$\mathcal{N}_p = 2mT{f_f}^2 = 2Tf_sf_f = 2\frac{\mathcal{N}}{m}, \tag{3.8}$$

which is m times smaller than what the traditional FIR filter requires.

This polyphase FIR filter is used to replace the FIR filter in the down sampling system shown in figure 3.1. The down sampling polyphase FIR filter is shown in figure 3.7. Because the signal sampling frequency is allowed to be higher than the filter sampling frequency in polyphase filters, the anti-aliasing and interpolation filter design becomes easier. As shown in figure 3.8, the signal sampling frequency is at 50 Hz and the signal below 1 Hz only aliases to frequencies above 50 Hz as shown in figure 3.3.
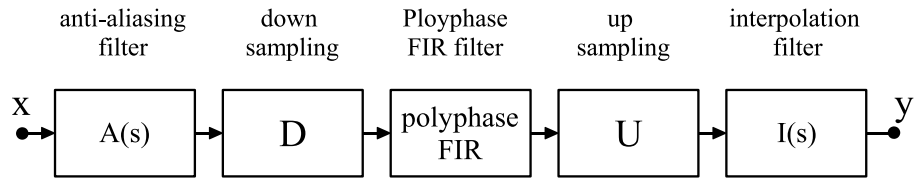
Figure 3.7: Polyphase FIR filter with down sampling.

3.4 Transfer Function Compensation

The output of the polyphase FIR filter is given by

$$y(n) = \sum_{q=0}^{N_f-1} x(n-qm)f(q), \tag{3.9}$$

where $x(n)$ denotes the nth input signal, $y(n)$ denotes the nth output signal, N_f is the number of coefficients of each FIR filter and $f(q)$ denotes the qth filter coefficient of the FIR filter.

If the transfer function of each FIR filter is $f(\omega), \omega \in [0, f_f]$, the transfer function
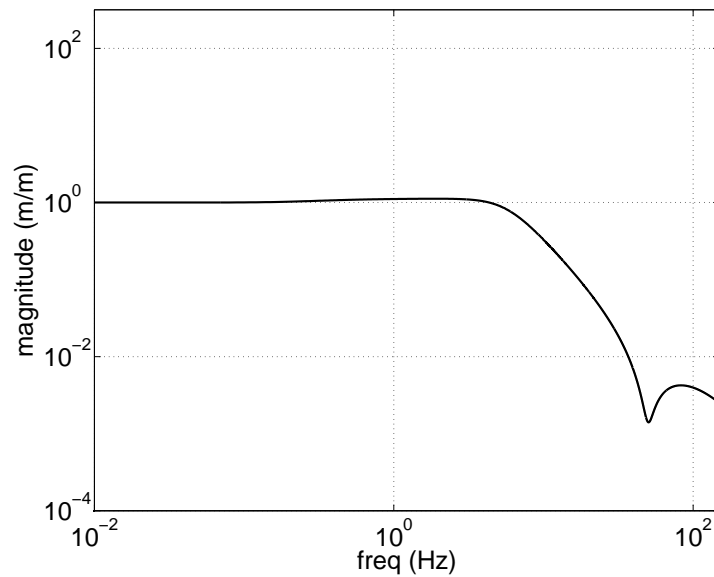
Figure 3.8: Interpolation filter for polyphase down sampling FIR filter.

of the polyphase FIR filter is given by:

$$P(\omega) = f(mod(\omega, f_f)), \omega \in [0, f_s].$$

(3.10)

At low frequencies, when $\omega \in [0, f_f]$, $P(\omega)$ is exactly the same as $F(\omega)$. However, is obvious that $P(\omega)$ is not perfect at higher frequencies. In fact, $P(\omega)$ is a periodic repetition of the function of $F(\omega)$ with a frequency period of f_f. An example of the transfer function of a polyphase FIR filter is shown in figure 3.9.
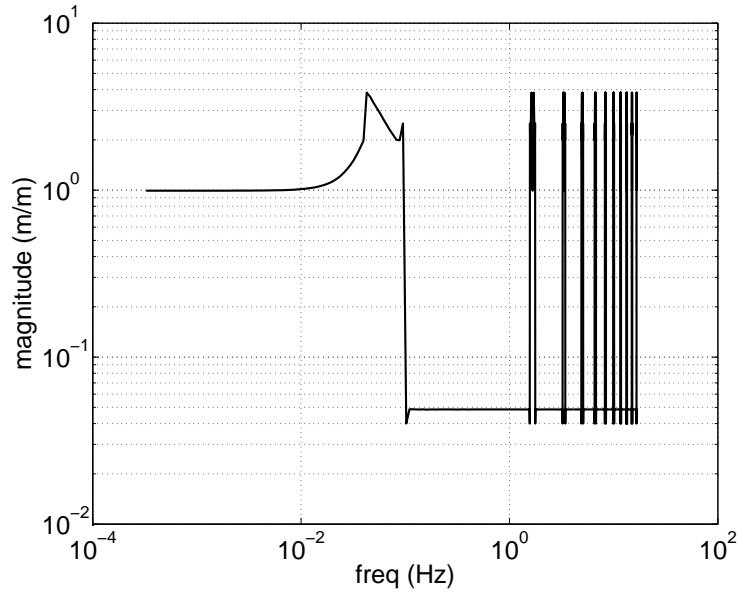
Figure 3.9: Transfer function of the high pass polyphase FIR filter based on the high-pass FIR filter shown in Figure 2.7. The sampling frequency of the FIR filter, f_s, is 1.67 Hz. The the peaks at around f_s, $2f_s$, $3f_s$ and so on are the frequency reflection of the low frequency component below 0.1 Hz.

Additional filters could be used to compensate the non-ideal transfer function of the polyphase FIR filter at frequencies above the filter sample frequency. First, a low pass IIR filter, L_a, as shown in figure 3.10(a), can be used to compensate the high frequency transfer function of a low pass polyphase FIR filter. The high pass complement can be simply implemented as in figure 3.10(b). After the compensation, the transfer function of the overall complementary filter pair (L_{cp}, H_{cp}) becomes:

$$L_{cp}(\omega) \;=\; L_p(\omega)L_a(\omega) \tag{3.11}$$

$$H_{cp}(\omega) \;=\; 1 - L_{cp}(\omega) \tag{3.12}$$

$$=\; 1 - (1 - H_p(\omega))(1 - H_a(\omega)) \tag{3.13}$$

$$=\; H_p(\omega) - L_p(\omega)H_a(\omega), \tag{3.14}$$

where the H_a denotes the complement of L_a. Equation 3.11 and 3.14 show that the compensation filter design problem is also a complementary filter design problem:

$|L_a|$ is preferred to be low at high frequencies such that the high frequency peaks of L_p is attenuated; $|H_a|$ is prefer to be low at low frequencies. In general, one would like to have

$$|L_{cp}| \leq \Psi_{Lc} \tag{3.15}$$

$$|H_{cp}| \leq \Psi_{Hc}, \tag{3.16}$$

where Ψ_{Lc} and $\Psi_{H}c$ are magnitude constrains for the overall complementary filters. If L_a and H_a are FIR filters, equation 3.16 and 3.15 defines an other convex optimization problem for fixed L_p and H_p. Practically, one can design the compensation filters which satisfies

$$|L_p(\omega)H_a(\omega)| \ll |H_p(\omega)| \tag{3.17}$$

$$\tag{3.18}$$

, such that H_p dominates the overall transfer function H_{cp}. For example,

$$|L_p(\omega)H_a(\omega)| \leq 0.2|H_p(\omega)|. \tag{3.19}$$

The frequency resolution of the compensation filters do not need to be as high as the original FIR filters. Hence, simple IIR filters can meet the requirement. It worth mentioning that it is easier to compensate the low pass FIR filter than to compensate the high pass FIR filter using a low pass IIR filter because we do not care about the phase of the low pass filter at high frequencies. To further simply the structure of the whole filter, the compensation low pass filter can also be used as the anti-aliasing filter.

Similarly, a high pass filter can be used to compensate the transfer function of the high pass polyphase FIR filter. In the original FIR filter design, the magnitude of the transfer function of the high pass filter is flat below 0.008 Hz because the FIR filter has not enough frequency resolution below that frequency. A high pass filter H_b can be applied to make the magnitude of the transfer function continue to decrease as a function proportional to frequency cubed below 0.008 Hz as shown in figure . The

final implementation of the complementary filter pair is shown in figure 3.12 (c) and (d).
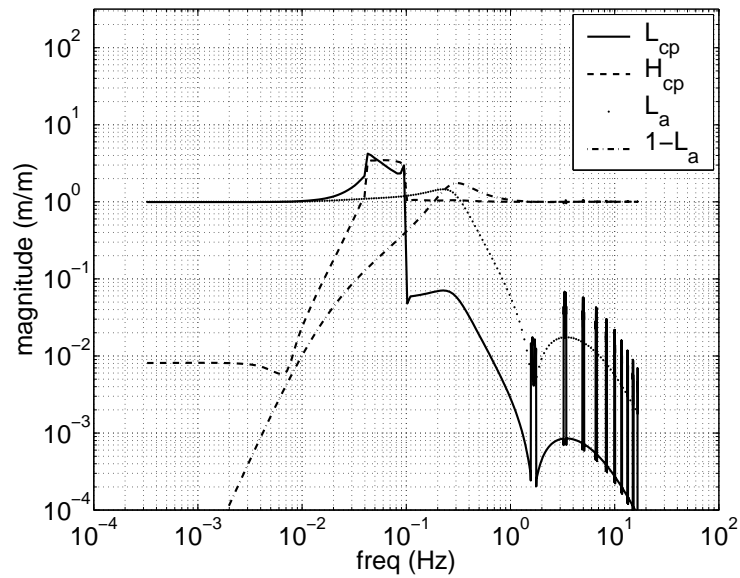
Figure 3.10: Low pass IIR filter L_a for compensating the high frequency transfer function of a low pass FIR polyphase filter in a complementary filter pair.
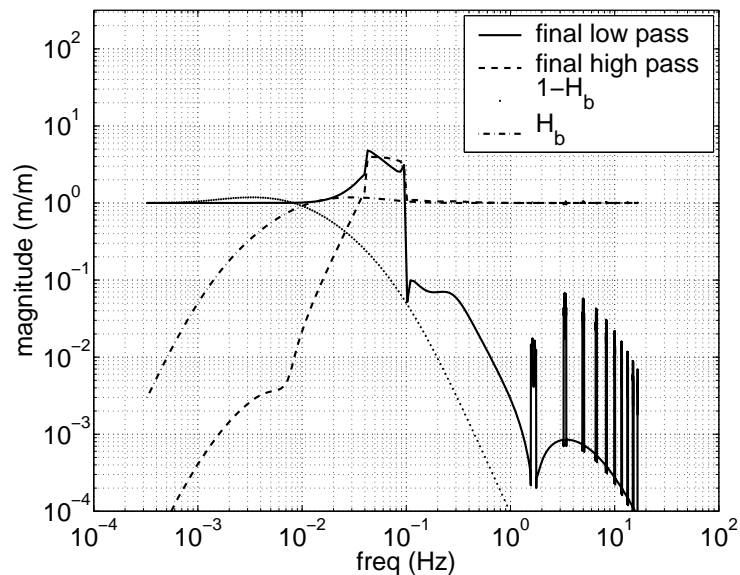
Figure 3.11: High pass IIR filter H_b for compensating the low frequency transfer

function of the high pass FIR polyphase filter in a complementary filter pair. At low frequencies, the final transfer function of the high pass filter is no longer flat.
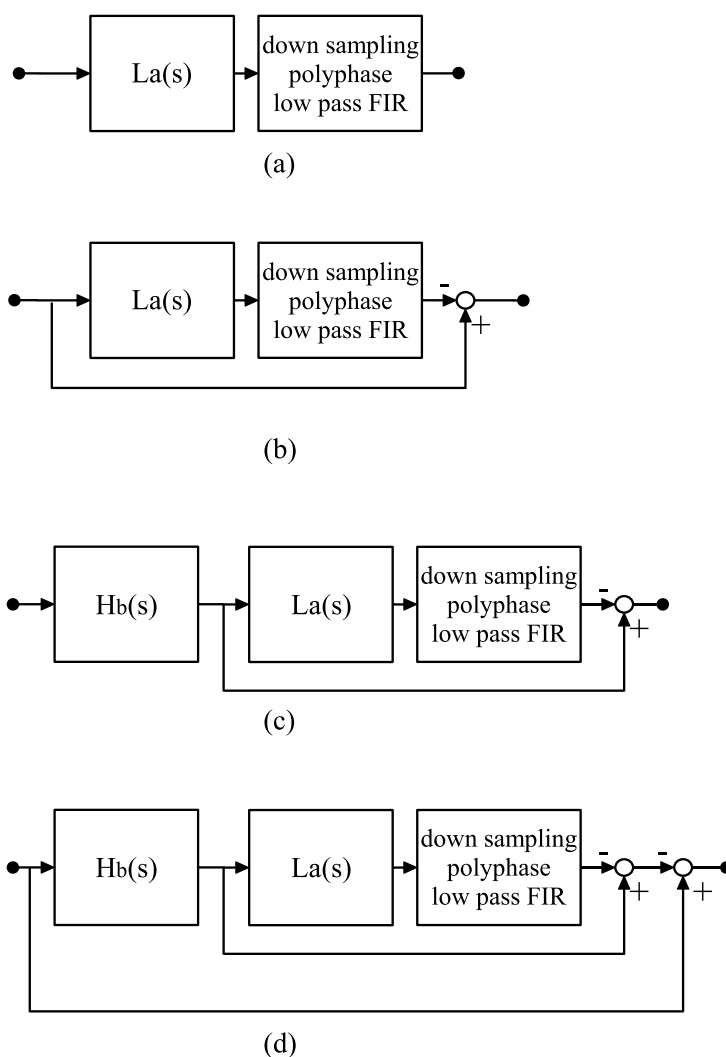
Figure 3.12: Transfer function compensation of polyphase FIR filter. (a) A low pass filter L_a is used with the low pass FIR filter to attenuate its peaks at high frequencies. (b) The high pass filter is simply built as the complement of (a). (c) A high pass filter is use to compensate the low frequency transfer function of (b). (d) The final low pass filter is implemented as the complement of the high pass filter in (c)

3.5 Summary

The polyphase FIR filter [1] decouples the noise problem and the transfer function problem in a FIR filter design by allowing different filter sampling frequency and signal sample frequency. Practically f_f could be much smaller than f_s, which saves a lot of calculation operations.

The transfer function design of the polyphase FIR complementary is separated into three frequency bands:

1. In the transition band, where the high pass filter and the low pass filter have comparable magnitude, there are a lot of structures in the transfer functions which requires high frequency resolution to implement. Hence, a lot of design effort and run time calculation capability is used to build the FIR complementary filter pair which dominates the whole transfer function in this frequency band.

2. At high frequencies, there is not much structure in the transfer functions: all we need to do is to allow the high pass filter to pass and the low pass filter to stop. Hence, it make sense to use simple (both simple to design and simple to implement) IIR filter, such as L_a, to dominate the transfer function in this band. Of course, it is possible to use another FIR filter to replace the IIR filter for even better performance.

3. Similarly at low frequencies, a simple IIR filter H_b is used to dominate the transfer functions.

Similar FIR filter structures, called multi-phase FIR filters, are widely used in digital signal processing systems [54]. There are two differences between that multiphase FIR filter and the polyphase filter in this chapter. First, the parallel FIR filters

---

[1]During the final editing of this thesis, it was realized that a mathematically equivalent FIR filter structure, called the interpolated FIR filter, was independently developed by other researchers [33]. However, there are still two differences between the interpolated FIR filter in [33] and the polyphase FIR filter in this thesis. 1, We studied the polyphase FIR filter structures for complementary filters. 2, The polyphase FIR filter structure in this thesis can be easily generalized to construct polyphase IIR filters.

are not identical to each other in the multi-phase filters. Second, the multi-phase FIR filter sums all the FIR filter outputs together, rather than using a cyclic collector. Interestingly, there is a duality relationship between these two kinds of filters in the ways that they reduce the number of calculations of a traditional FIR filter as shown in equation 3.1: the multi-phase decimation filter decimates the signal, while the polyphase filter decimates the filter coefficients.

Chapter 4

Tilt Horizontal Coupling

4.1   Introduction

To reach the design sensitivity of the proposed Advanced LIGO detectors, the seismic isolation system is required to isolate the interferometer mirrors from ground motion in the observing band above 10 Hz and to reduce the RMS motion in the range of 0.1 Hz to 10 Hz to simplify the stabilization of the laser interferometer. At the LIGO observatories, the seismic motion has peaks near 0.15 Hz. These microseismic peaks dominate the seismic motion above 0.1 Hz. The isolation system needs to reduce the magnitude of those seismic peaks by at least a factor of five in all three translational degrees of freedom at same time.

Tilt-horizontal coupling is the most challenging problem that needs to be solved in low frequency seismic isolation. Tilt-horizontal coupling is a result of the principle of equivalence: inertial horizontal sensors cannot distinguish horizontal acceleration from tilt motion. The magnitude of tilt-horizontal coupling goes up very rapidly at low frequencies, which makes low frequency vibration isolation extremely difficult.

4.2   Tilt Horizontal Coupling Problem

4.2.1   Inertial Sensor

An inertial sensor senses its motion with respect to inertial space by measuring the apparent force acting on its proof mass in the sensor's sensitive direction. When the sensor is operating in the Earth's gravitational field, the apparent force on the sensor is:

$$F = m(\frac{d^2}{dt^2}x - g\cos\Theta), \tag{4.1}$$

where m denotes the mass of the proof mass, x denotes the sensor's position in inertial space, g is the gravitational acceleration constant on Earth, and Θ denotes the angle of sensor's sensitive direction with respect to the local vertical, defined by the gravitational field. Hence, the sensor's output is not only a function of the sensor's position, but also a function of the sensor's orientation. The sensor's sensitive direction, Θ, can be decomposed as the sum of its nominal direction, Θ_0, and its incremental change, θ:

$$\Theta = \Theta_0 + \theta. \tag{4.2}$$

Then, the incremental change of the apparent force, f, is given by

$$f = m(\frac{d^2}{dt^2}x + g\theta \cdot \sin\Theta_0). \tag{4.3}$$

For vertical inertial sensors, $\Theta_0 = 0$, therefore, they are not sensitive to small orientation changes. However, for horizontal sensors, $\Theta_0 = \frac{\pi}{2}$, and

$$f = m(\frac{d^2}{dt^2}x + g\theta), \tag{4.4}$$

which implies that the horizontal inertial sensors are sensitive to both horizontal motion and tilt motion. This is called inertial sensor tilt-horizontal coupling. In fact, equation 4.4 shows that the tilt-horizontal coupling effect can be directly explained by the principle of equivalence: a local observer can not distinguish between acceleration and a gravitational field. For this reason, the tilt-horizontal coupling is universal for
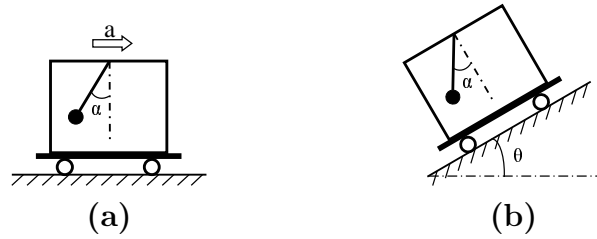
Figure 4.1: Simple pendulum in a box as a horizontal inertial sensor. The sensor is sensitive to both horizontal acceleration (a) and tilt motion (b), which demonstrates the intrinsic tilt-horizontal coupling problem for inertial horizontal sensors.

all horizontal inertial sensors, independent of the sensors' specific implementation[27].

Conceptually, a horizontal inertial sensor can be implemented as a simple pendulum mounted inside a rigid box as shown in figure 4.1. The apparent acceleration of the box can be measured by observing the angle of the pendulum in the rigid box. In figure 4.1(a), when the platform is accelerating horizontally, the pendulum will rotate an angle, α, thus the sensor can sense the horizontal acceleration. On the other hand, if the sensor is tilted by an angle, θ, as shown in figure 4.1(b), the pendulum will also rotate with respect to the rigid box, which demonstrates the tilt sensitivity of the sensor. An observer sitting inside the rigid box cannot distinguish between these two situations. Therefore, the tilt-horizontal coupling problem is an intrinsic problem for the inertial horizontal sensor.

In the frequency domain, the inertial sensor's response function, $P(s)$, is given by the Laplace transform of equation 4.4:

$$P(s) = \beta(s)[x(s)s^2 + g\theta(s)], \tag{4.5}$$

with some scaling $\beta(s)$ to account for sensor dynamics and electronics. The ratio between the sensor's tilt sensitivity and horizontal sensitivity is $\frac{g}{s^2}$. At high frequencies, the sensor's tilt sensitivity can be ignored and the sensor behaves as a normal horizontal sensor. However, at low frequencies, the sensor's tilt sensitivity dominates and the horizontal inertial sensor behaves more like a tilt sensor.

4.2.2   Actuator and Tilt-Horizontal Coupling Zero

The tilt-horizontal coupling problem is made worse by imperfections in the actuators and the plant. When the horizontal actuator is commanded to drive the platform horizontally, it will typically cause the platform to tilt slightly as well. At low frequencies, because the horizontal inertial sensors are very sensitive to tilt motion, even small tilts can create problems.

Denote the transfer function from horizontal actuator command, $h_c(s)$, to horizontal motion of the platform, $x(s)$, as $H(s)$, i.e.,

$$x(s) = H(s)h_c(s). \tag{4.6}$$

The tilt-horizontal coupling can be represented by

$$\theta(t) = \gamma(x,t)x(t). \tag{4.7}$$

The tilt-horizontal coupling coefficient, $\gamma(x,t)$, is, in general, time varying and nonlinear. However, if γ is assumed to be constant, the systems's horizontal transfer function from the actuator command to the inertial sensor's output is:

$$G(s) = \frac{P(s)}{h_c(s)} = \beta(s)H(s)(s^2 + g\gamma). \tag{4.8}$$

The tilt-horizontal coupling of the actuators is directly related to the curvature of the platform's horizontal moving path. For example, in the conceptual system shown in figure 4.2, the cart tilts when it moves back and forth on the bottom of a circle with radius R. The tilt horizontal coupling coefficient is given by:

$$\gamma = \frac{1}{R}. \tag{4.9}$$

Hence, the system's horizontal transfer function is

$$G(s) = \beta(s)H(s)(s^2 + \frac{g}{R}). \tag{4.10}$$
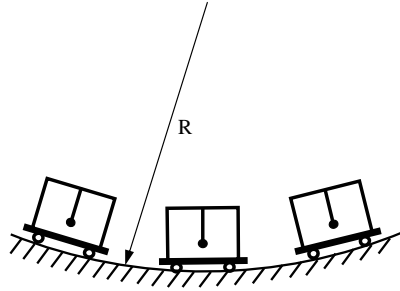
Figure 4.2: Tilt-horizontal coupling and curvature of the system's horizontal path. When the cart goes into free body motion along the path at frequency $\omega_0 = \sqrt{\frac{g}{R}}$, the pendulum does not move with respect to the rigid box.

Figure 4.3 shows an example of a transfer function measured from the horizontal actuator to the horizontal inertial sensor in our prototype system (which is described in more detail in later chapters). The zero at about 120 mHz is not from the natural mechanical modes of the system but an effect that comes from tilt-horizontal coupling. From equation 4.10, the system's horizontal transfer function has two zeros at $s_0 = \pm\sqrt{\frac{g}{R}}$, where the tilt component and the horizontal component have the same magnitudes. Define

$$\omega_0 = \sqrt{\frac{g}{R}} \tag{4.11}$$

as the tilt-horizontal coupling zero frequency. Therefore,

$$R = \frac{g}{\omega_0{}^2}. \tag{4.12}$$

At frequencies below ω_0, the system's horizontal transfer function is dominated by the tilt component, while at frequencies above ω_0, it is dominated by the horizontal component.

The existence of the tilt-horizontal coupling zero can be directly explained by the conceptual cart-pendulum model in figure 4.2. When the cart goes into the free body motion along the curved path, the apparent force acting on the proof mass is zero, thus the pendulum remains perpendicular to the roof of the rigid box, which means the sensor's output is zero. The frequency of the free body motion along a path with
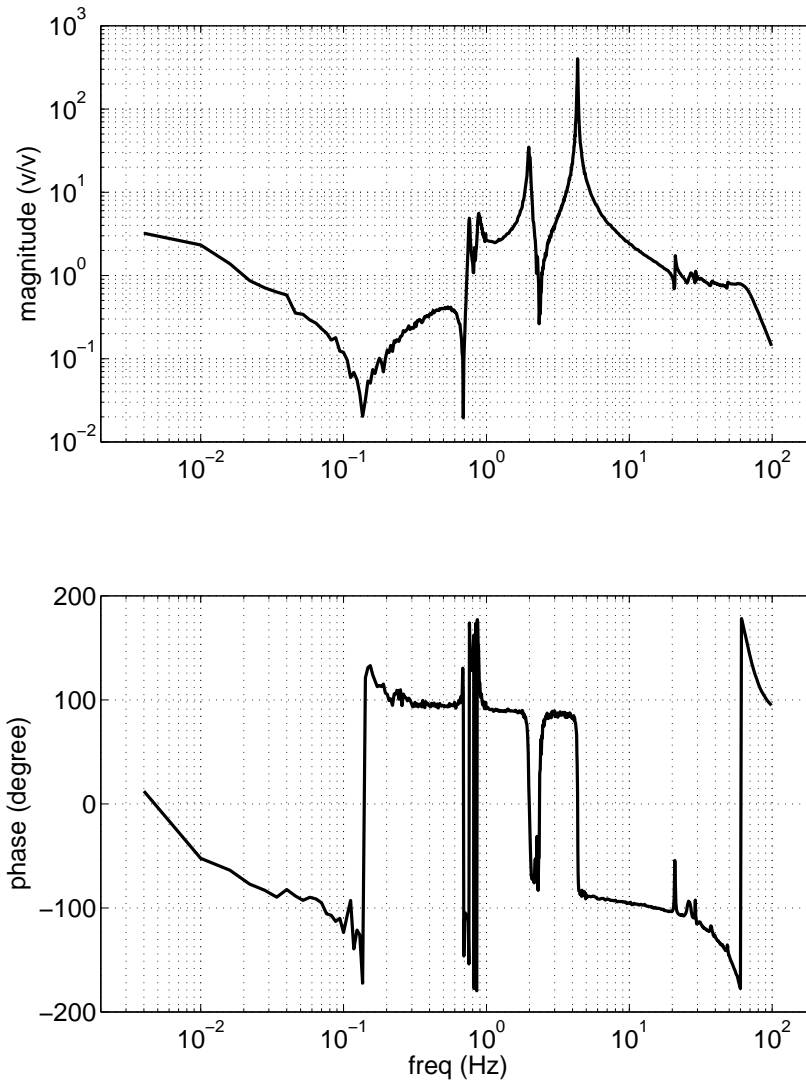
Figure 4.3: A transfer function from a horizontal actuator to a horizontal inertial sensor in our prototype. The zero at 120 mHz is called the tilt-horizontal coupling zero.

radius R (also called pendulum motion) is exactly the same as the tilt-horizontal coupling zero frequency given by equation 4.11.

The frequency of the tilt-horizontal coupling zero is critical for low frequency horizontal vibration isolation systems. In an active isolation system, if low frequency inertial sensors are used directly in the feedback control loop (called direct feedback system), the sensor's output is driven to be zero by the control system. (Of course, we have to assume that the control system is stable and has enough loop gain.) This means the active controller will force the system to follow the free body motion on the system's horizontal path. As result, the system will only have horizontal isolation at frequencies above the tilt-horizontal coupling zero frequency. To achieve an isolation factor of 10 above 0.1 Hz and have robust performance with a relatively simple control law, the system's tilt-horizontal coupling zero frequency should be around 0.01 Hz or below. For passive vibration isolation systems, the situation is similar. In a passive system, the tilt-horizontal coupling frequency is equivalent to the natural pendulum frequency.

4.2.3 Curvature

Equation 4.12 shows the radius of the horizontal path is inversely proportional to the tilt-horizontal coupling zero frequency squared as shown in the table 4.1. The rapid

$2\pi\omega_0$ (Hz)	0.01	0.1	1
R (meter)	2,480	24.8	0.248

Table 4.1: Radius of the horizontal path for different tilt-horizontal coupling frequencies.

growth of the path radius R as $\omega \to 0$ creates one of the most challenging problems in reducing the tilt-horizontal coupling in low frequency active isolation systems. For example, to have the tilt-horizontal coupling zero frequency below 0.01 Hz, the radius of the path should be larger than 2.5 km. Nominally the total RMS of the ground seismic vibration below 1 Hz is about 10^{-6} meter, which implies that the change in the platform tilt over this stroke length should be less than 10^{-6} m/2.5 km = 0.4 nrad!
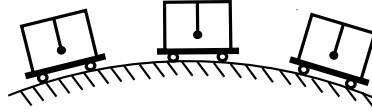
Figure 4.4: Horizontal motion path with negative curvature.

Another problem comes from the shape of the horizontal path. Figure 4.2 shows a path with constant positive curvature, but the actual path shape is typically more complicated. For example, the path could have a negative curvature, which would change the sign of the tilt-horizontal coupling coefficient and result in non-minimum phase zeros, or the path could be non-linear, as discussed in the next section.

Figure 4.5 shows a typical horizontal transfer function for a system with negative horizontal path curvature. Comparing to figure 4.3, the phase of the transfer function is changed by 180 degrees at frequencies below 0.12 Hz, which indicates the sign change in the tilt-horizontal coupling coefficient.

One problem associated with the negative horizontal path curvature is stability, because the free body motion on such a path is not stable. In a direct feedback system, the controller forces the platform to follow the free body motion and fall down along the path. For a passive system, negative horizontal path curvature means that the system is mechanically nonstable and will collapse.

4.2.4   Nonlinear Coupling

The real difficulty of handling the tilt-horizontal coupling problem comes from its nonlinearity. In practical mechanical systems, the horizontal motion path does not always have constant curvature as discussed in section 4.2.3. It could have mountains and valleys as shown in figure 4.6, which means that the tilt-horizontal coupling effect is nonlinear. Figure 4.7 shows the horizontal transfer functions for our system measured using a random driving signal at different RMS levels. The tilt-horizontal coupling zero frequency moved from 0.06 Hz to 0.18 Hz as the RMS drive level changes from 0.011 volt to 0.13 volt, which is a clear indication of the nonlinearity of the system.
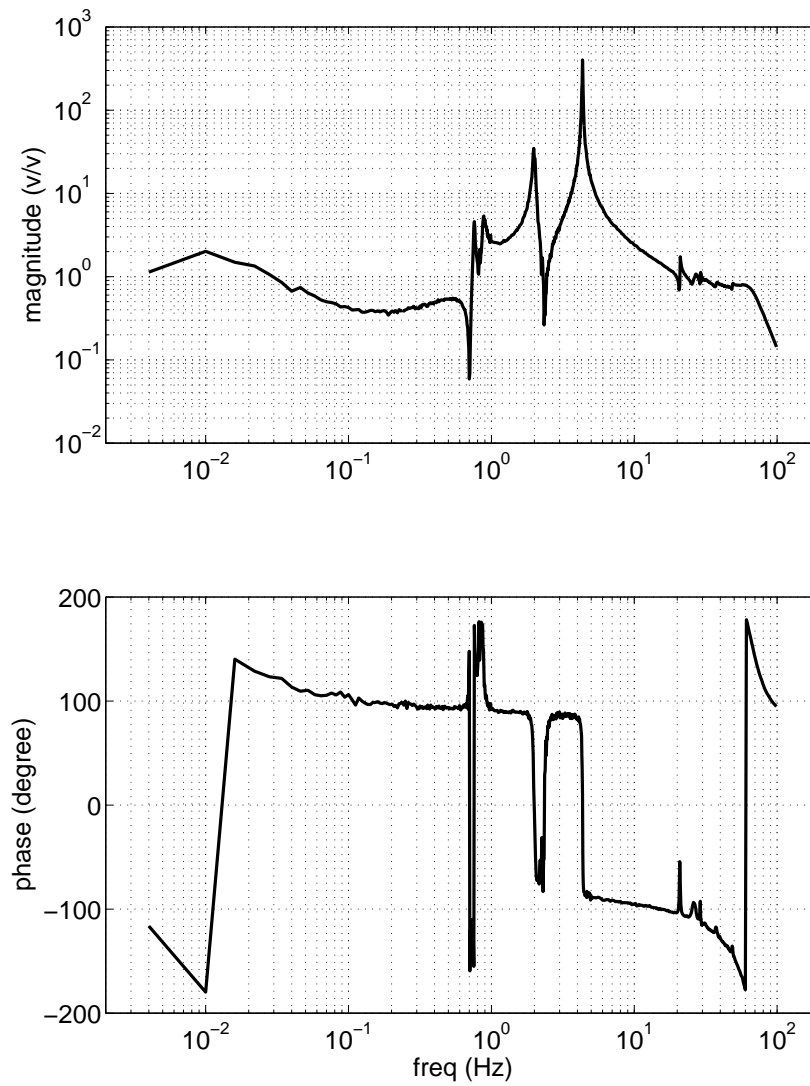
Figure 4.5: Transfer function from horizontal actuators to horizontal inertial sensors. The non-minimum phase tilt-horizontal coupling zeros are at 0.12 Hz

Additional evidence of nonlinearity came from the harmonic analysis of the system, as shown in figure 4.8. The three horizontal actuators are driven with a sine signal, at three different frequencies: 0.0527 Hz, 0.0625 Hz, and 0.0793 Hz. The drive levels are the same for the three actuators. The platform moves about 80 μm horizontally in this test. In the spectrum of the STS-2 inertial sensor's output, many high-order harmonics generated by the nonlinear coupling of the system are visible.

Actually, it should not be surprising to see the high nonlinearity in the tilt-horizontal coupling. Because the inertial sensors are very sensitive to tilt motion at low frequencies, even very small nonlinear tilt couplings will be evident. As discussed in section 4.2.3, if the tilt-horizontal coupling zero is at 0.01 Hz, the total amount of tilt allowed is less than 0.4 nrad. If the horizontal stiffness is similar to the vertical stiffness and the vertical springs are separated by 1 meter, the magnitude of nonlinear vertical forces generated at the vertical springs only need to be 4×10^{-10} of the magnitude of the horizontal force to generate the total allowed tilt. Many components in a practical mechanical system can contribute nonlinearity at this level. Examples include the nonlinearity of the spring stiffness, the nonlinearity of the actuators, the nonlinearity from the stiffness of the wires for various instruments mounted on the platform, etc.

One problem associated with nonlinear tilt-horizontal coupling is that the horizontal motion path could have multiple valleys. The free body motion on such paths will have multiple equilibrium points. The platform could move from one equilibrium point to another due to seismic excitations. In addition, the system can not sense such horizontal motions by itself! For these reasons, it is extremely difficult, and perhaps impossible, to build direct feedback or passive systems to achieve the low frequency horizontal vibration isolation required by Advanced LIGO using only local inertial sensors.

More details of nonlinear tilt horizontal coupling will be discussed in later chapters.
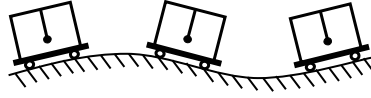
Figure 4.6: Horizontal motion path with non-constant curvature.
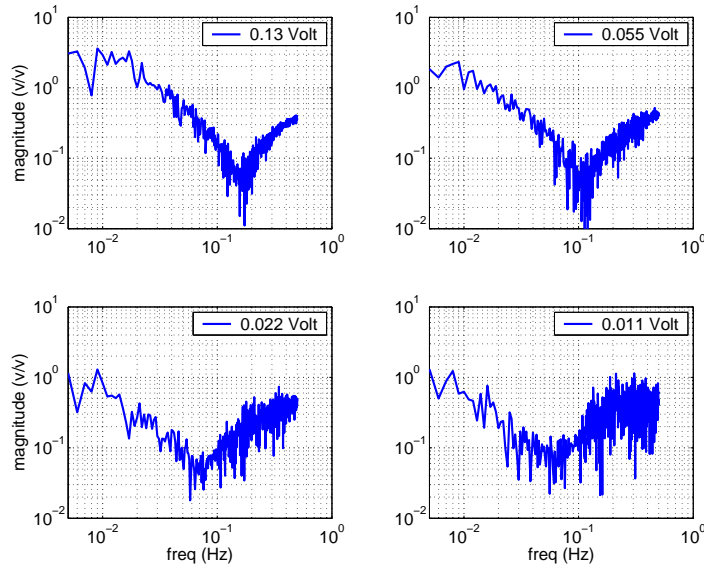
Figure 4.7: The tilt-horizontal coupling zero frequency changes from 0.18 Hz to 0.06 Hz as the RMS drive level changes from 0.13 volt to 0.011 volt.

4.2.5   Tilt Horizontal Coupling Noise

The tilt-horizontal coupling effect not only changes the system's horizontal transfer function but also adds noise to the horizontal sensors. Figure 4.9 shows the ground motion measured by the STS-2 inertial sensor. The horizontal direction and the vertical direction have similar signals above 0.04 Hz. For example, the micro-seismic peaks show up in both directions at about 0.15 Hz. However, at frequencies below 0.04 Hz, the signals in the two directions are very different: the ground motion seen by the horizontal inertial sensor is about 40 times larger than that seen by the vertical sensor! The difference can be explained, again, by tilt-horizontal coupling. Because the horizontal inertial sensor is very sensitive to tilt motion at low frequencies, the tilt noise of the ground and the sensor itself are magnified. As shown in figure 4.9,
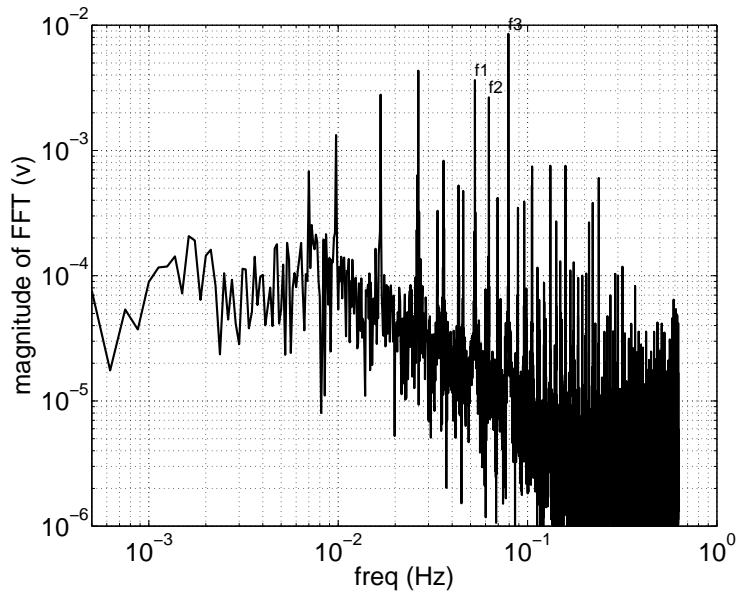
Figure 4.8: Harmonic analysis of the nonlinearity of the open loop system. The three horizontal actuators are driven by three sine signals with frequencies, $f1 = 0.0527$ Hz, $f2 = 0.0625$ Hz, and $f3 = 0.0793$ Hz. This plot shows the FFT of the signal from one of the horizontal STS-2 sensors.

the tilt noise is proportional to inverse frequency cubed at frequencies below 0.04 Hz. Because the vertical inertial sensor is not sensitive to tilt motion its noise level is much lower at low frequencies. However, the noise level of the vertical sensor also goes up proportional to inverse frequency cubed at frequencies below 0.015 Hz, which could be explained by the vertical STS-2 having a little horizontal sensitivity. Because of the existence of the low frequency tilt noise in horizontal inertial sensors, aggressive high pass FIR filter have be designed to attenuate it.

4.3   Reduction of Tilt Horizontal Coupling

4.3.1   Actuator Correction

One way to reduce the tilt-horizontal coupling is to add an additional torque to correct the tilt motion. This is equivalent to changing the actuation point of the
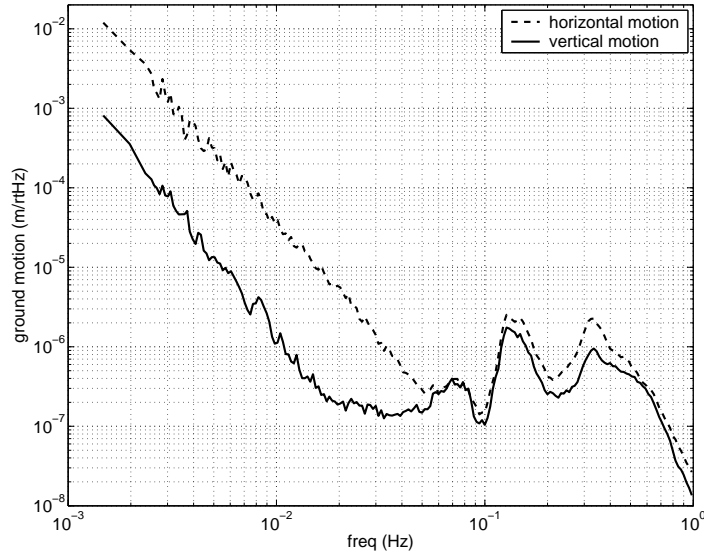
Figure 4.9: Ground motion measured by the STS-2 inertial sensor.

horizontal actuators along the vertical direction. The hope is that if the horizontal actuator could operate just at the correct point, there would be no tilt horizontal coupling. This is called actuator correction and can be done either mechanically or electronically. In fact, the transfer function of figure 4.5 was obtained by electronically moving the equivalent horizontal actuator up by 1 cm in the system that normally has a transfer function as shown in figure 4.3. As result, the sign of the tilt-horizontal coupling is changed. One might suggest that if the actuator is just moved up by 0.5 cm, the tilt-horizontal coupling could be much reduced.

One of problems of actuator correction is the alignment accuracy. Because the tilt-horizontal coupling coefficient is proportional to the square of the tilt-horizontal coupling zero frequency, to have the tilt-horizontal coupling zero frequency below 0.01 Hz and keep the curvature positive is very challenging. For example, to move the zeros in figure 4.3 down by a factor of 10, the error of the alignment of the horizontal actuators should be less than

$$\frac{0.5 \text{ cm}}{2 \times 10^2} = 25 \ \mu\text{m}, \tag{4.13}$$

where the the factor of 2 comes from the fact that we have to stay on the side of the perfect cancellation for which the zeros are minimum phase, i.e., to keep positive curvature in the positive path. In general, if a system's horizontal stiffness is the same as the vertical stiffness and vertical springs are separated by a distance L, the maximum allowed error for actuator correction alignment is:

$$\epsilon = \frac{L^2}{2R},$$
(4.14)

where R is the radius associated with the remaining tilt-horizontal coupling zero frequency. Another problem of the actuator correction is that it does not reduce the nonlinear tilt-horizontal coupling. One might suggest introducing nonlinear correction terms, but correction with enough accuracy and repeatability is very difficult to achieve in practice.

4.3.2   Tilt Correction by Inertial Tilt Sensors

One might suggest using a low frequency absolute inertial tilt sensor to measure the tilt motion and thus remove the tilt sensitivity of horizontal inertial sensors by sensor correction. Here absolute inertial tilt sensor refers to tilt sensors that are only sensitive to tilt motion in inertial space but not sensitive to horizontal motion in inertial space. Because of the principle of equivalence, the absolute inertial tilt sensors have to be non-local sensors: they have to use moments to differentiate horizontal motion from tilt motion.

For example, a gyroscope uses rotational momentum to measure absolute rotation in inertial space. However one difficulty of this tilt correction approach is that it is hard to build an absolute inertial tilt sensor that is sensitive enough. At 0.04 Hz the tilt horizontal noise of an STS-2 seismometer is about $5 \times 10^{-7} m/\sqrt{\text{Hz}}$. To correct this tilt noise, the noise level of the absolute inertial tilt sensor should be less than $3 \times 10^{-9} \, rad/\sqrt{\text{Hz}}$ at 0.04 Hz. A tilt sensor with this level of sensitivity is very difficult to build. For example, the precision Hemispherical Resonator Gyro (HRG) built by D. A. Bauer [32] has noise level about $2 \times 10^{-8} \, rad/\sqrt{\text{Hz}}$ at 0.04 Hz.

A dumbbell tilt sensor [12] [59] [61] [46] uses moments of inertia to separate tilt

from horizontal motion. The difficulty for the dumbbell sensors is that it is hard for them to reduce the ratio between the sensor's horizontal sensitivity T_h and tilt sensitivity T_t to the necessary level [46]:

$$\frac{T_h}{T_t} = \frac{d}{r^2} < \frac{\omega_0^2}{g},$$

(4.15)

where d is the distance from the suspension point to the center of gravity of the dumbbell, r is a average radius (such that moments of inertia is $M = mr^2$, and m is the mass), ω_0 is the frequency of the tilt horizontal coupling zero, and g is gravity acceleration constant. For example, if we would like to have the tilt horizontal coupling zero frequency to be less than 0.01 Hz, for a dumbbell with average radius of 0.5 meter, the suspension point should be at most 0.1 mm above the center of gravity of the dumbbell, which is quite a challenge for its mechanical design.

One could also use two vertical inertial sensors separated by a distance l to measure the tilt. Assume the horizontal sensor and the vertical sensors to have the same noise level N. The noise that is introduced to the horizontal direction by tilt correction is

$$N_{Tc} = \frac{\sqrt{2}g}{\omega^2 l} N.$$

(4.16)

The N_{Tc} will be larger than N at frequencies below $\omega_{Tc} = \sqrt{\frac{l}{\sqrt{2}g}}$. Note that ω_{Tc} is independent of N and thus the same for all inertial sensors. For $l = 1.4$ m, $\omega_{Tc} \approx 0.5$ Hz. And for STS-2 sensors, N_{Tc} is larger than that of the ground tilt noise.

For the lack of inertial sensors that are good enough at low frequencies, tilt correction is not applied in our system.

4.3.3 High Gain Control Loop in Tilt Directions

We used high gain feedback control loops in the two tilt directions to reduce tilt horizontal coupling. Figure 4.10 shows the open loop gain of one of the tilt controllers. The controller has very high loop-gain at low frequencies–about 10^3 at 0.1 Hz and above 2×10^4 below 0.02 Hz. When the control loops are closed, the controller commands the platform to move in a path such that the tilt sensor super sensor,

dominated by differential position sensors at low frequencies, goes to output zero. Hence, the tilt motion generated by the imperfection of actuators and the platform is automatically reduced. The reduction factor is about the open loop gain–more than 1000 below 0.1 Hz.

In the frequency band where the loop gains are high, the platform can be driven by injecting offset signals to the sensors' outputs. The harmonic analysis of the closed loop system is shown is figure 4.11. The offset signals of the three horizontal position sensors are driven by three sine signals with frequencies, $f1 = 0.033$ Hz, $f2 = 0.0357$ Hz, and, $f3 = 0.0390$ Hz, such that the platform moves a similar distance as it moved in figure 4.8. Compared to the open loop response shown in figure 4.8, the high order harmonics generated by nonlinearity are dramatically reduced. A detail analysis of the nonlinearity of the system when it is controlled is in chapter 6.

4.3.4   Sensor Alignment

Once the control loops are closed through the super sensors, the remaining tilt-horizontal coupling comes from the position sensors. At low frequencies, the position sensors are the dominant feedback sensors. The high loop-gain of the controllers forces the platform to follow the motion defined by the position sensors. If the target plates of the three vertical position sensors are not perfectly parallel, they will cause the platform to tilt when it moves horizontally. In fact, the parallelism can be calculated by measuring the frequency of the tilt-horizontal coupling zero. Correction terms can then be implemented in the controller by commanding a small tilt proportional to the horizontal displacement. The transfer function from the horizontal position sensor offset signal to the horizontal feedback STS-2 sensor on stage 1 of the corrected system is shown in figure 4.12. The tilt-horizontal coupling zero frequency is below 0.02 Hz, which indicates that the minimum radius is larger than 500 m. When the platform is moving horizontally at 0.1 Hz, the ratio between the tilt component and the horizontal component in the inertial sensor's signal is given by:

$$\eta = \frac{R_{0.1}}{R} < \frac{1}{20},\tag{4.17}$$

where $R_{0.1}$ is the radius associated with tilt-horizontal coupling zero frequency of 0.1 Hz, and R is the actual curvature of the horizontal path.

Another effect that needs to be considered is vertical-tilt coupling. If the gain of the vertical position sensors are not same, tilt motion will be generated when the platform is moved vertically. Similar to tilt-horizontal coupling, the amount of tilt-vertical coupling can be measured by the amount of tilt signal generated by the horizontal inertial sensors while the platform is driven to move vertically.

4.4 Summary

Because a horizontal inertial sensor is dominantly sensitive to tilt motion at low frequencies, solving the tilt horizontal coupling problem is inevitable for low frequency vibration isolation systems. Since a low frequency absolute inertial tilt sensor below 0.04 Hz is very difficult to build, tilt correction is not practical in most cases. This implies that tilt motion and horizontal motion are not distinguishable below 0.04 Hz in these systems.

The tilt horizontal coupling problem presents a fundamental performance limit for the vibration isolation system where absolute tilt sensor are not used. At low frequencies when the ground tilts, the isolated platform is preferred not to move horizontally with respect to ground to compensate the apparent acceleration. Because the whole system can not distinguish horizontal from tilt motion at low frequencies, when the ground moves horizontally the platform should not move with respect to ground either. The transfer function $T(\omega)$ from horizontal ground motion in inertial space to horizontal platform motion in inertial space is desired to be as close to 1 as possible at low frequencies (Note that we are discussing a single stand alone vibration isolation system here. Global control using the interferometer signal, in chapter 9 of LIGO could be different.):

$$|1 - T(\omega)| \leq T_t(\omega). \text{ for } \omega < 0.04 \text{ Hz,} \qquad (4.18)$$

where $T_t(\omega)$ is a real function which denotes the tilt horizontal coupling reduction

performance. For frequencies above 0.1 Hz, the platform is preferred not to move with respect to inertial space when the ground moves such that vibration isolation is achieved. Hence $T(f)$ should satisfy

$$|T(\omega)| \leq T_h(\omega). \text{ for } \omega > 0.1 \text{ Hz,} \qquad (4.19)$$

where the real function T_h denotes the desired horizontal isolation performance. Hence, the complementary filter design problem given by inequality 4.18 and 4.19 presents the fundamental tradeoff between tilt horizonal coupling reduction and horizontal vibration isolation: increasing the horizontal isolation performance is at the cost of increasing tilt horizontal coupling. The performance limit for low frequency horizontal isolation system can be studied by solving the complementary filter design problem using the FIR complementary design algorithms described in previous chapters. This performance limit is true for any systems as long as the tilt and horizontal motion is not distinguished below ω_0, no matter whether the system is a passive system or an active system, no matter whether the system is a single stage system or a multi-stage system. For example, in our system, either sensor correction or sensor blending can be used to reduce the tilt horizontal coupling with the optimal FIR filters. One might suggest to use both of these techniques at the same time to get better performance. However, the best overall performance is determined by inequality 4.18 and 4.19. If using one technique can achieve the overall best possible performance, adding another technique in will not bring much benefit.

The advantage of active vibration isolation systems is that the fundamental performance limit can be approached by the active control by two means. First, reduce the tilt motion when the system is moved horizontally, which can be achieved very efficiently with high gain active tilt control. Second, optimal FIR filters with high frequency resolution can be used to separate tilt noise below 0.1 Hz from horizontal motions above 0.1 Hz in the frequency domain.
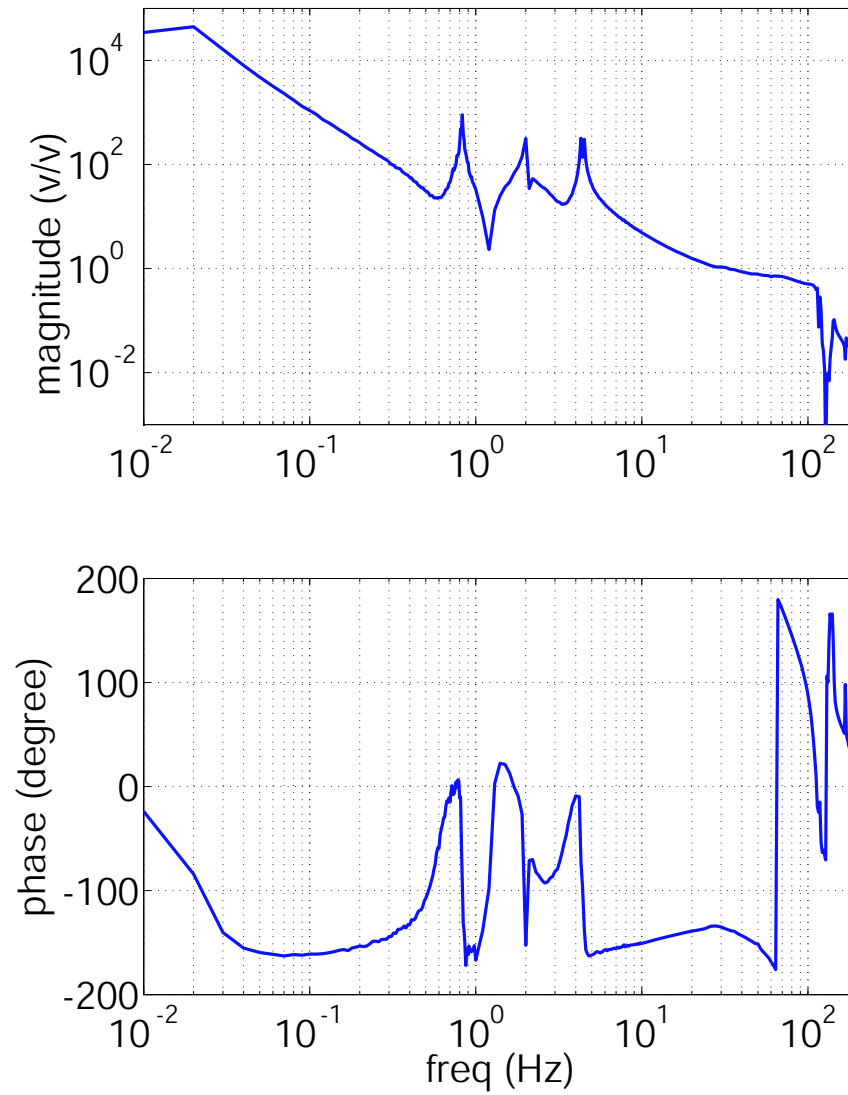
Figure 4.10: Open loop gain of the tilt controller. The high loop gain at low frequencies helps linearize the system.
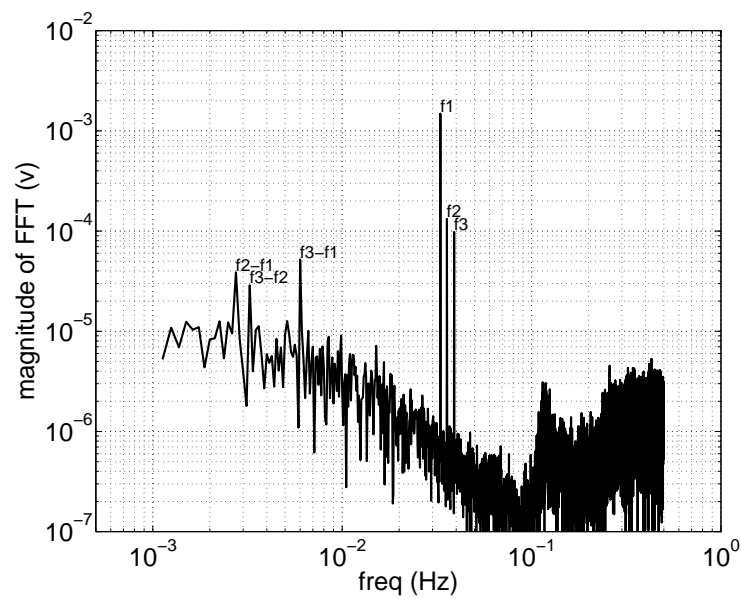
Figure 4.11: Harmonic analysis of the closed loop system. The offset of the three position sensors are driven by three sine signals with frequencies, $f1 = 0.033$ Hz, $f2 = 0.0357$ Hz, and, $f3 = 0.0390$ Hz. This figure shows the spectrum of the signal of one of the horizontal STS-2 sensors.
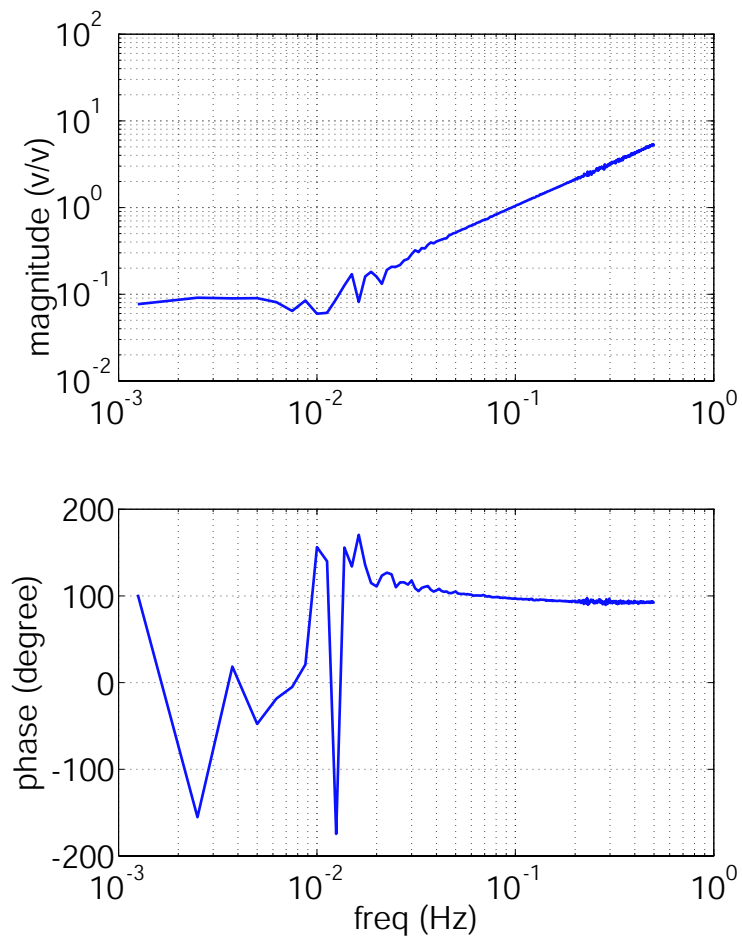
Figure 4.12: Closed loop transfer function from the horizontal position sensor offset signal to the feedback horizontal STS-2 sensor on stage 1. The data below 0.02 Hz in this figure is dominated by measurement noise. Hence, it shows that the tilt-horizontal coupling zero frequency is below 0.02 Hz.

Chapter 5

Linear MIMO System analysis

5.1 Introduction

The vibration isolation and alignment system proposed for LIGO is a multi-input multi-output (MIMO) system with 12 degrees of freedom, 12 actuators and about 42 sensors. To efficiently study the behavior of such complicated systems, a set of MIMO linear and nonlinear analysis tools are developed. In this chapter, we will discuss the tools to measure the transfer function and the spectral densities of different signals when the system is assumed to be linear.

5.2 Frequency Resolution of the Fourier Transform

The Fourier transforms are frequently used in the system analysis tools that are going to be discussed in this chapter. For a time domain digital signal x with sampling time t_s, the Fourier transform is conducted in two steps:

1. Collect N equally spaced points of data ($x(n)$, $n = 0$, 1, ..., N) from the signal x. Hence the data collection time is $T = Nt_s$ is also called the integration time of the Fourier transform.

2. Calculate the digital Fourier transfer of $x(n)$: $X(f)$, $f = 0$, f_0, $2f_0$, ... , $(N-1)f_0$, where $f_0 = 1/T$ is called the frequency step of the Fourier transform.

5.2.1   Integer Number Frequency

For a finite time Fourier transform, the frequency resolution is limited. In general, the Fourier transform of a sinusoid signal contains nonzero elements not only at its nominal frequency, but also at other frequencies. This is called frequency leaking, which is shown in Figure 5.1. The only set of sinusoid signals that do not have such a problem are those whose frequencies are multiples of frequency step f_0, i.e., 0, f_0, f_1, ..., and so on. We call this set of frequencies integer frequencies because we can label them with integer numbers according to its multiple of f_0.

Definition 5.2.1. *Particularly, for integration time T, define the frequency number of frequency n/T as n.*
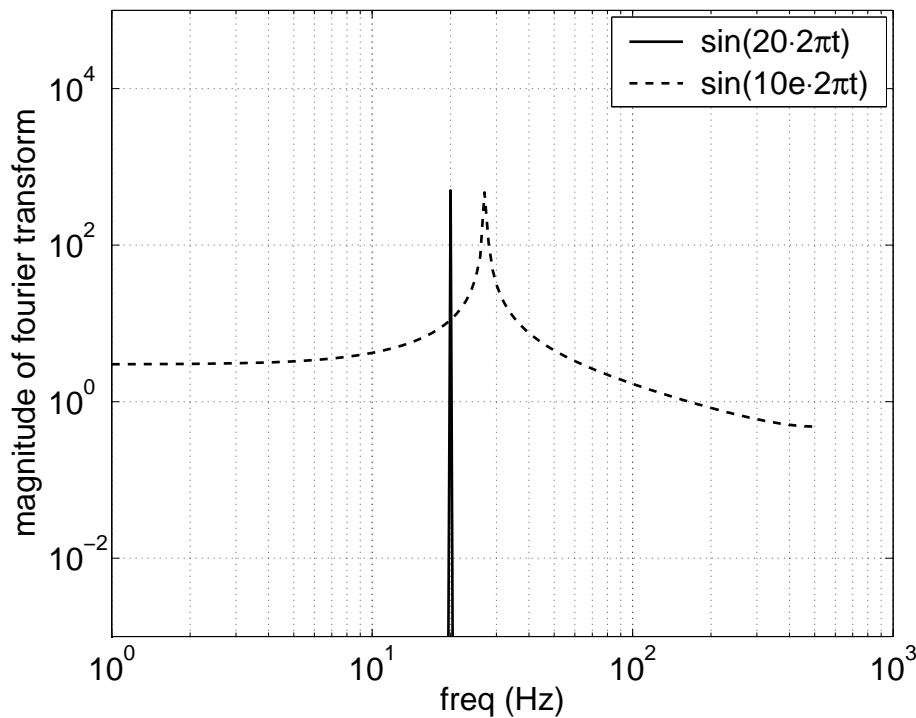
Figure 5.1: Frequency leakage problem for finite integration time Fourier transform. The integration time, T, is one second. Only when the frequency is a multiple of $1/T = 1$ Hz, the signal does not leak from its nominal frequency to the neighboring frequencies. As shown by the solid line in the picture, when the frequency is 20 Hz, there is no leakage. As a counter example shown by the dash line, where the frequency

of the signal is $10e \approx 27.18$ Hz. The fourier transform of the signal leaks from the nominal frequency at 27 Hz to neighboring frequencies.

For signals that complete integer number of cycles in the integration time T, all of their frequency components have integer frequencies and hence does not have the frequency leaking problem.

5.2.2   Non-Integer Number Frequency

For the signals that contains non-integer number frequency components, frequency leaking is not avoidable. However, there are two ways to reduce the leakage. First, a window function can be applied to the signal before the Fourier transform. Second, one use a long integration time when it is possible.

5.3   MIMO Transfer Function Measurement

The transfer function of a linear system is measured in the following sequence:

1. Apply the drive signals to the system's actuators.

2. Wait for a settling time T_w, until the system is in steady state.

3. Collect data from the sensors and process it.

4. Repeat from step one with different drive signals if necessary.

5.3.1   Step Sine Drive Signal and Random Drive Signal

There are two kinds of signal that are commonly used for drive signals: step sine signal and random signal.

The step sine drive signal measurement is done in multiple steps. In each measurement step (i.e. steps 1 to 3 in procedure 5.3) a sinusoid signal of a certain frequency is used as the drive signal to measure the system's transfer function at that frequency. The advantage of step sine measurement includes

1. The integration time can be chosen as the integer multiple of the sine function period to avoid frequency leakage.

2. The magnitude of the sine function can be adjusted at each step such that sensors or actuators have large enough signal level within their dynamic range.

3. For each step sine measurement, high order harmonics can be observed to test the nonlinearity of the system.

4. For MIMO systems sine signals with different frequencies can be used for different actuators to achieve channel multiplexing (measure multiple transfer functions at the same time).

The disadvantage of step sine is that we have to wait for settling time for the system to go to steady state for each measurement cycle. For systems with low resonant frequency and low damping the total wait time could be so long that it becomes the dominate time consumption for the whole measurement procedure.

In random drive signal measurement, a band limited, white or colored, random signal is used as the drive signal. The advantage of random drive signal is that a whole frequency band, rather than a frequency point, is measured every measurement cycle. Hence, the system only need to settle down once and a lot of waiting time can be saved. The drawback of random drive measurement is obvious:

1. Because the drive signal is not a periodical signal, frequency leakage is inevitable. Hence one needs to depend on a long integration time to achieve high frequency resolution.

2. It is difficult to monitor if the system is nonlinear or not.

3. Channel multiplexing can be achieved by driving independent random signals on different actuators. However, high orthogonality of different drive signal channels can only be obtained by a long integration time.

5.3.2   Comb Frequency Random Signal

To overcome the disadvantages of step sine and random drive signals, a comb frequency random signal (CFRS) is proposed as the drive signal. All frequency componenta of CFRS are integer frequencies for the integration time, so no frequency leaking happens during the Fourier transform.

signal construction

The CFRS is designed in the frequency domain in three steps.

1. Decide the magnitude of drive level for each frequency number $m(n)$.

2. Randomly choose phase $\phi(n)$ for each frequency number.

3. Construct the time domain signal by the inverse Fourier transform.

To keep the drive signal a real function in time domain the magnitude and the phase has to satisfy:

$$m(n) = m(-n) \text{ and } \phi(n) = -\phi(-n). \tag{5.1}$$

Hence, we only need to choose the magnitude and phase for the non-negative frequency numbers, and the rest is determined by equation 5.1. One problem of constructing the drive signal in the frequency domain is that the signal in the time domain could have high peaks, which appears when many different frequency components add up constructively at a certain time. To find a set of optimum phases for each frequency component such that the magnitude of the time domain peak is minimized is not a convex optimization problem and hence very difficult to solve. Practically, this problem is addressed by randomizing the phases of different frequency components such that the probability of many of them adding up constructively in the time domain is low. One can also do a Monte Carlo optimization along this approach: design the drive signal for many times and chose the one with the minimum time domain peak.

Noise Measurement

We can choose a certain frequency components to have zero magnitudes to measure
the noise at those frequencies. Those zero magnitude frequency components are called
noise traps. For example, we can choose to have nonzero magnitude components to
be at the frequency numbers of 0, k, $2k$,..., where k is an integer, and zero magnitude
components on other frequency numbers, as shown in figure 5.3
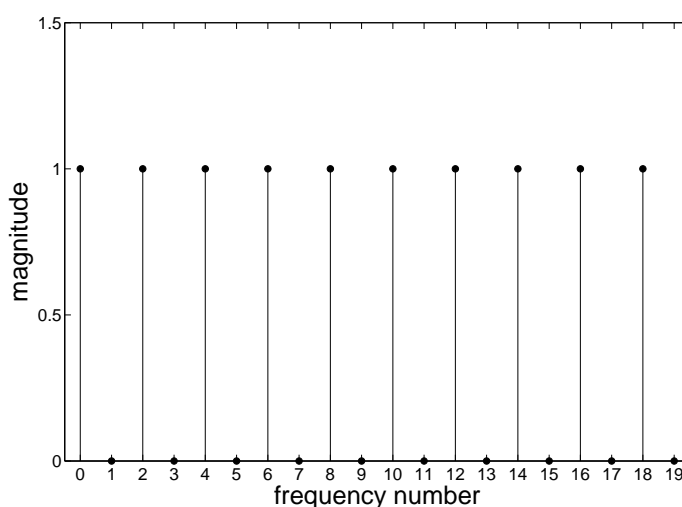
Figure 5.2: Choose some frequency components in the comb frequency random sig-
nal to have zero magnitudes to measure the noise at those frequencies. Those zero
magnitude frequency components are called noise traps.

Nonlinearity Monitoring

Similar to the noise traps, we can also use zero magnitude frequency components to
monitor nonlinearity of the system, which are called nonlinearity traps. For example,
we can put the nonzero magnitude components in frequency numbers of an odd
multiple of integer k, i.e., k, $3k$, $5k$,..., etc. The zero magnitude components at even
multiple of k, i.e. 0, $2k$, $4k$, ..., etc., becomes the nonlinearity traps. The rest of
zero components are noise traps. If the system is linear, if the input of a certain
frequency is zero, the output should also be zero except noise. For nonlinear systems,
this is not true. For example if the system has a second order nonlinearity, and

the nonzero input frequency components are at frequency numbers of k and $3k$, the output could have nonzero frequency components at frequency numbers of $2k$ and $4k$. If the nonzero magnitude frequency numbers are multiple of k, the nonzero frequency component generated by nonlinearity of the system in the output signal should also have frequency numbers that are multiples of k. If the system is nonlinear, the nonlinear traps will have larger magnitudes than the neighboring noise traps. If the system shows signs of nonlinearity, it should be studied using the nonlinear analysis tool that is going to be discussed in chapter 6.
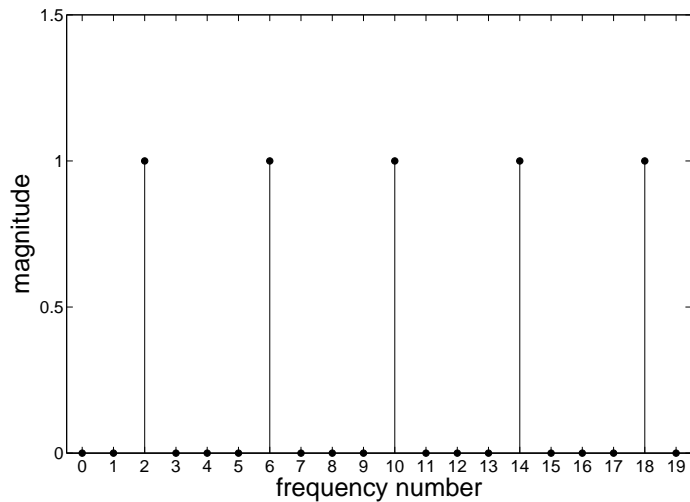
Figure 5.3: Choose some frequency components in the comb frequency random signal to have zero magnitudes to monitor the nonlinearity of the system. Frequency numbers of 0 4 8 ... are nonlinearity traps. Frequency numbers of 1 3 5 ... are noise traps.

Channel Multiplexing

Channel multiplexing using CFRS can be achieved by choosing different nonzero components for different input channels. For example in a two input system, we can choose nonzero components to be at even frequency numbers for the first actuator and at odd frequency numbers for the second actuator.

In conclusion, the three different methods of measuring MIMO transfer functions

are compared in table 5.1.

	step sine	random	CFRS
settling time	multiple	once	once
nonlinear monitor	yes	no	yes
frequency leak	no	yes	no
noise measurement	yes	yes	yes
channel multiplexing	yes	yes	yes

Table 5.1: Comparing different drive signals for MIMO transfer function measurement.

5.4   Spectrum Measurement

Daniell's periodogram [14] [47] frequency averaging method is used to estimate the power spectral density (PSD), amplitude spectral density (ASD), and cross spectral density (CSD) of different signals. In general, a spectral density (including PSD, ASD, and CSD), is measured in six steps:

1. Collect N points of data from each of the signal channels.

2. Detrend the time domain signal of each channel by subtracting the best fitted polynomial, which is obtained by least-squares fitting. Order 5 polynomials are used in our experiments.

3. Apply window functions to time domain data. Hanning windows are used in our experiments.

4. Calculate the FFT of windowed time domain data.

5. For each of signal channels, divide the frequency domain data into F frequency bins. Each bin has n frequency data points. Hence, $N = Fn$. The frequency band width of the frequency bin is denoted as f_b.

6. Calculate the average spectral density and average frequency of each frequency bin. In each frequency bin, the average frequency is defined as the arithmetic

average of the frequencies of the data points. The n data points in each frequency bin of each channel are represented by a column vector. The elements of each vector are assumed to be random variables with the same probability distribution function and independent of each other.

For the frequency bin with average frequency ω, the frequency domain data points of sensor channel x is denoted as a vector $x(\omega)$. The PSD of signal x is defined as

$$P_x(\omega) = \lim_{n \to \infty} \frac{x(\omega)x^{\dagger}(\omega)}{f_b}. \tag{5.2}$$

The ASD of x is $A_x(\omega) = \sqrt{P_x(\omega)}$. The CSD of signal x and signal y is defined by

$$C_{xy}(\omega) = \lim_{n \to \infty} \frac{y^{\dagger}(\omega)x(\omega)}{f_b}. \tag{5.3}$$

Note that $C_{xx}(\omega) = P_x(\omega)$. $C_{xy}(\omega)$ is estimated with finite n, i.e.

$$C_{xy}(\omega) \approx \bar{C}_{xy}(\omega) = \frac{y^{\dagger}(\omega)x(\omega)}{f_b}. \tag{5.4}$$

Note that $\bar{C}_{xy}(\omega)$ is a unbiased estimation, i.e. the expectation value of $\bar{C}_{xy}$ is

$$\mathbf{E}\bar{C}_{xy}(\omega) = C_{xy}(\omega). \tag{5.5}$$

Another method, the Welch's periodogram, is widely used for spectral density measurement [57] [47]. For example, Matlab uses Welch's method to calculated PSD, CSD and ASD. The advantage of Daniell's method is that it offers higher frequency resolution than Welch's method [25][8].

5.4.1 Back to Back Sensor Noise Measurement

In an active vibration isolation system, the sensor noise dominates the platform's vibration noise in the controlled band. Hence, it is very important to measure the noise levels of different sensors in the system.

Back to back sensor noise measurement is one of the ways to measure the noise levels of the sensors [7] [37]. For example, to measure the noise levels of two seismometers, one could put them back to back along a straight line, and use the difference of the two outputs to estimate the noise level of the sensors. One problem with this approach is: because the common mode motion signal is often much larger than the sensor noises, the gain of the two sensors have to be accurately matched. To obtain a good gain match, the following automatic gain matching algorithm [7] [37] can be used.

For the frequency bin with average frequency ω, the frequency domain data points of the two sensors are denoted as vectors $x(\omega)$ and $y(\omega)$. The motion that these two sensors are measuring is denoted as $m(\omega)$.

$$
\begin{aligned}
x(\omega) &= g_x(\omega)m(\omega) + n_x(\omega); & (5.6) \\
y(\omega) &= g_y(\omega)m(\omega) + n_y(\omega), & (5.7)
\end{aligned}
$$

where $g_x(\omega)$ and $g_y(\omega)$ denote the gains of the two sensors, and $n_x(\omega)$ and $n_y(\omega)$ denote the noise of the two sensors. Denote the motion portion of the sensor signals as $m_x(\omega)$ and $m_y(\omega)$:

$$
\begin{aligned}
m_x(\omega) &= g_x(\omega)m(\omega); & (5.8) \\
m_y(\omega) &= g_y(\omega)m(\omega). & (5.9)
\end{aligned}
$$

$m(\omega)$, $n_x(\omega)$ and $n_y(\omega)$ are assumed to be independent complex Gaussian inter-element independent random vector variables (CGIEIRVV), which is defined as follows.

Definition 5.4.1. *A complex random vector variable with n elements*

$$
A = \begin{bmatrix} A_{1r} + A_{1i}j \\ A_{2r} + A_{2i}j \\ \vdots \\ A_{nr} + A_{ni}j \end{bmatrix}
\tag{5.10}
$$

is defined as complex Gaussian inter-element independent random vector variable, if all the real and imaginary parts of the elements, i.e. A_{1r}, A_{1i}, A_{2r}, A_{2i}, ..., A_{nr}, A_{ni} are independent real random variables with identical Gaussian distributions.

$$P_x(\omega) = g_x^\dagger(\omega)g_x(\omega)P_m(\omega) + P_{n_x}(\omega); \tag{5.11}$$

$$P_y(\omega) = g_y^\dagger(\omega)g_y(\omega)P_m(\omega) + P_{n_y}(\omega); \tag{5.12}$$

$$C_{xy}(\omega) = g_y^\dagger(\omega)g_x(\omega)P_m(\omega) \tag{5.13}$$

The relative gain between the two sensors

$$k_{xy}(\omega) = \frac{g_x(\omega)}{g_y(\omega)} \tag{5.14}$$

is estimated by solving the optimization problem with variable $\bar{k}_{xy}(\omega)$:

$$\min \quad P_{\epsilon_x}(\omega) \tag{5.15}$$

$$\text{subject to} \quad \epsilon_x(\omega) = x(\omega) - y(\omega)\bar{k}_{xy}(\omega) \tag{5.16}$$

. The basic idea behind this automatic gain matching method is to remove the part that is coherent with the reference sensor, $y(\omega)\bar{k}_{xy}(\omega)$, from the signal of the target sensor, and treat the residue , $\epsilon_x(\omega)$, as sensor noise. The optimal solution is:

$$\bar{k}_{xy}(\omega) = \frac{C_{xy}(\omega)}{P_y(\omega)} = \frac{g_y^\dagger(\omega)g_x(\omega)P_m(\omega)}{g_y^\dagger(\omega)g_y(\omega)P_m(\omega) + P_{n_y}(\omega)}, \tag{5.17}$$

$$\epsilon_x(\omega) = n_x(\omega) - \bar{k}_{xy}(\omega)n_y(\omega) + (g_x(\omega) - g_y(\omega)\bar{k}_{xy}(\omega))m(\omega), \tag{5.18}$$

$$P_{\epsilon_x}(\omega) = P_{n_x}(\omega) + |\bar{k}_{xy}(\omega)|^2 P_{n_y}(\omega) + |g_x(\omega) - g_y(\omega)\bar{k}_{xy}(\omega)|^2 P_m(\omega) \tag{5.19}$$

The PSD of the motion portion of the sensor signals are.

$$P_{m_x}(\omega) = |g_x(\omega)|^2 P_m(\omega) \tag{5.20}$$

$$P_{m_y}(\omega) = |g_y(\omega)|^2 P_m(\omega) \tag{5.21}$$

In terms of P_{m_x} and P_{m_y}, the optimal solution becomes:

$$\bar{k}_{xy}(\omega) \quad = \quad k_{xy}(\omega)\frac{P_{m_y}}{P_y}, \tag{5.22}$$

$$\epsilon_x(\omega) \quad = \quad n_x(\omega) + \frac{P_{m_y}}{P_y}k_{xy}(\omega)n_y(\omega) + \frac{P_{n_y}}{P_y}g_x(\omega)m(\omega), \tag{5.23}$$

$$P_{\epsilon_x}(\omega) \quad = \quad P_{n_x}(\omega) + (\frac{P_{m_y}(\omega)}{P_y(\omega)})^2|k_{xy}(\omega)|^2P_{n_y}(\omega) + (\frac{P_{n_y}(\omega)}{P_y(\omega)})^2P_{m_x}(\omega) \tag{5.24}$$

$P_{\epsilon_x}(\omega)$ can be used as an estimation of $P_{n_x}(\omega)$. Since $P_{\epsilon_x}(\omega) \geq P_{n_x}(\omega)$, $P_{\epsilon_x}(\omega)$ is actually an upper limit of the PSD of the noise of sensor x. The estimation becomes unbiased when the other two terms on the right side of equation 5.24 are zero. The second term on the right side of equation 5.24 is the amount of noise of the sensor y that was introduced to $P_{\epsilon_x}(\omega)$ when the two sensor two sensors channels were combined together. When the signal to noise ratio of sensor y is high, i.e. $\frac{P_{n_y}}{P_{m_y}} \gg 0$, $\frac{P_{m_y}}{P_y} \approx 1$, this term becomes $|k_{xy}|^2P_{n_y}$, which can be interpreted as the equivalent PSD of the noise of sensor y if it is measured by sensor x. Hence, even if the sensor to noise ratio of y is high and the gain match error is low, the noise of sensor y can not be separated from the noise of sensor x. The third term, denoted as $P_{\epsilon_{xk}}$, is the contribution from the common mode motion due to the error in gain matching. When the signal to noise ratio of y is high, $P_y(\omega) \approx P_{m_y}$,

$$P_{\epsilon_{xk}} \approx \frac{P_{n_y}^2(\omega)P_{m_x}}{P_{m_y}^2(\omega)} = \frac{P_{n_y}^2(\omega)|g_x|^2}{|g_y|^4P_m} \tag{5.25}$$

Equation 5.25 shows that the contribution due to gain match error is proportional to the inverse of the PSD of the common mode motion. The estimation of the sensor noise level is better when the common mode motion is higher.

The Effect of Finite Data Points

In the above analysis, the number of frequency points in each frequency bin, n, is assumed to be infinity, which is practically impossible. If n is finite, the relative gain

between the two sensors is obtained by solving the optimization problem: $\tilde{k}_{xy}(\omega)$:

$$\min \quad \bar{P}_{\epsilon_x} = \frac{\epsilon_x^\dagger \epsilon_x}{f_b} \tag{5.26}$$

$$\text{subject to} \quad \epsilon_x(\omega) = x(\omega) - y(\omega)\tilde{k}_{xy}(\omega) \tag{5.27}$$

. The optimal solution is:

$$\tilde{k}_{xy}(\omega) = \frac{y^\dagger(\omega)y(\omega)}{y^\dagger(\omega)y(\omega)} \tag{5.28}$$

$$\bar{P}_{\epsilon_x}(\omega) = \frac{x^\dagger(\omega)x(\omega)}{f_b}\left(1 - \frac{|x^\dagger(\omega)y(\omega)|^2}{x^\dagger(\omega)x(\omega)y^\dagger(\omega)y(\omega)}\right) = \bar{P}_x(\omega)(1 - \bar{\rho}_{xy}(\omega)), \tag{5.29}$$

where $\bar{\rho}_{xy}(\omega)$ denotes the estimation of the coherence between $x(\omega)$ and $y(\omega)$.

If $x(\omega)$ and $y(\omega)$ are independent CGIEIRVV, the expected value of $\rho(\omega)$ is $1/n$ [25] [8]. Hence, for finite n, the noise level estimated by the optimal gain matching, $\bar{P}_{\epsilon_x}$, is, on average, $1 - 1/n$ of the noise measured directly, $\bar{P}_x$.

For the case that $x(\omega)$ and $y(\omega)$ are not independent, consider the optimization problem with variable $\hat{k}_{xy}$:

$$\min \quad \bar{P}_{\epsilon_x} = \frac{\epsilon_x^\dagger \epsilon_x}{f_b} \tag{5.30}$$

$$\text{subject to} \quad \epsilon_x(\omega) = x(\omega) - y(\omega)(\hat{k}_{xy}(\omega) + \bar{k}_{xy}(\omega)), \tag{5.31}$$

where $\bar{k}_{xy}(\omega)$ is the solution of the optimization problem defined by equation 5.33 and 5.34 when there are infinite number of data points in each frequency bin. Note that the optimal value $\bar{P}_{\epsilon_x}(\omega)$ for the optimization problem defined by equation 5.33 and 5.34 is the same as the optimal value of the optimization problem defined by equation 5.30 and 5.31. Construct new variable

$$\grave{x}(\omega) = x(\omega) - \bar{k}_{xy}(\omega)y(\omega). \tag{5.32}$$

(Note that $P_{\grave{x}}(\omega)$ is the estimation of the PSD of the portion of signal of x that is not correlated to y when $\bar{k}_{xy}$ is known.) The optimization problem defined by equation

5.30 and 5.31 becomes:

$$\min \quad \bar{P}_{\epsilon_x} = \frac{\epsilon_x^\dagger \epsilon_x}{f_b} \tag{5.33}$$

$$\text{subject to} \quad \epsilon_x(\omega) = \dot{x}(\omega) - y(\omega)\hat{k}_{xy}(\omega) \tag{5.34}$$

.

For any two corresponding elements, $\dot{x}_i(\omega)$ and $y_i(\omega)$, in the vectors $\dot{x}(\omega)$ and $y(\omega)$, the expected value:

$$\mathbf{E}y_i^\dagger(\omega)\dot{x}_i(\omega) = \mathbf{E}y_i^\dagger(\omega)x_i(\omega) - \bar{k}_{xy}(\omega)\mathbf{E}y_i^\dagger(\omega)y_i(\omega) \tag{5.35}$$

Note that

$$\bar{k}_{xy}(\omega) = \frac{\mathbf{E}y_i^\dagger(\omega)x_i(\omega)}{\mathbf{E}y_i^\dagger(\omega)y_i(\omega)}. \tag{5.36}$$

We have

$$\mathbf{E}y_i^\dagger(\omega)\dot{x}_i(\omega) = 0. \tag{5.37}$$

So, since $\dot{x}(\omega)$ and $y(\omega)$ are assumed CGIEIRVV, they are independent vector variables. Hence, for finite n, the optimal value $\bar{P}_{\epsilon_x}$ for the optimization problem defined by equation 5.33 and 5.34 is:

$$\bar{P}_{\epsilon_x} = (1 - \frac{1}{n})P_{\dot{x}}(\omega) \tag{5.38}$$

For conclusion, if n is finite, the expected value of the estimated noise level is about $1 - 1/n$ the estimated noise level when n is infinite.

Discussion

From the analysis above, the automatic gain matched back to back noise measurement method has some attractive properties. However, when the noise levels of the sensors are low, there are some practical difficulties for this approach. First, because ground vibration is orders of magnitudes higher than the noise level of sensors, the dynamic ranges of the sensors, electronic readouts and the analog to digital (DA) converters

are often not high enough for an accurate measurement of the sensors' noise levels. Hence, the two seismometers have to be put on a vibration isolated platform to reduce the total signal levels. Secondly, because the motion of the platform on which the two sensors are mounted has more than one degree of freedom, the two sensors have to be aligned along a line to ensure that they are sensing the same motion. Thirdly, even though a sensor's noise level can be measured using such a method, the sensor's actual noise level could be different when it is installed in the actual system. For example, the noise levels of capacitive position sensor might depend on their electrical environments.

5.4.2 Measure Noise Level of Sensors on Platform With Multiple Degrees of Freedom

The idea of automatic gain matching for back to back noise measurements can easily be generalized for measuring the noise of multiple sensors on a platform with multiple degrees of freedom. For example, on the second stage of our ETF vibration isolation system (the details of the system will be discussed in chapters 7), there are 6 vertical GS-13 seismometers (3 of them are feedback sensors and 3 of them are witness sensors). The second stage platform has 3 degrees of freedom associated with vertical motion: vertical translation and the two tilt rotations. Any three of the six sensors are enough to measure all three DOF motion. We can pick one of the six sensors as the target sensor and call the rest reference sensors.

In general, the data points of the target sensor x in a frequency bin is denoted as $x(\omega)$. The data points of the k reference sensors y_1, y_2, ..., y_k are denoted as a matrix

$$y(\omega) = [y_1(\omega), y_2(\omega), ..., y_k(\omega)]. \tag{5.39}$$

Note that x and y_i are not X and Y axes but different sensor names.

$$x(\omega) = m(\omega)g_x(\omega) + n_x(\omega), \tag{5.40}$$

$$y(\omega) = m(\omega)g_y(\omega) + n_y(\omega), \tag{5.41}$$

where matrix $m(\omega)$ denotes the motion of the platform in d degrees of freedom,

$$m(\omega) = [m_1(\omega), m_2(\omega), ..., m_d(\omega)],$$

matrix $n_y(\omega)$ denotes the motion of the noise of the sensors,

$$n_y(\omega) = [n_{y_1}(\omega), n_{y_2}(\omega), ..., n_{y_k}(\omega)],$$

and d by k matrix $g_y(\omega)$ denotes the gain of reference sensors to the motion of the platform. The CSD matrix of the reference channels $C_{yy}(\omega)$

$$C_{yy} = g_y^\dagger P_m g_y + P_{n_y}. \tag{5.42}$$

The CSD between the target sensor and the reference sensors is

$$C_{xy} = g_y^\dagger P_m g_x. \tag{5.43}$$

Conceptually, we can construct a virtual sensor, $\check{x}$, by the linear combination of the reference sensors such that the virtual sensor and the target sensor measures the same motion:

$$\check{x}(\omega) = y(\omega)k_{xy}(\omega), \tag{5.44}$$

where k_{xy} is a gain matching vector. The noise of the target sensor can be estimated in a similar way to the back to back measurement that was discussed in the last section. The gain matching vector can be estimated by solving a optimization problem:

$$\min \quad P_{\epsilon_x} \tag{5.45}$$

$$\text{subject to} \quad \epsilon_x(\omega) = x(\omega) - y(\omega)\bar{k}_{xy}(\omega) \tag{5.46}$$

.

The optimal solution is:

$$\bar{k}_{xy} = C_{yy}^{-1}C_{xy} \tag{5.47}$$

$$\epsilon_x = n_x - n_Y\bar{k}_{xy} + m(g_x - g_y\bar{k}_{xy}), \tag{5.48}$$

$$P_{\epsilon_x} = P_{n_x} + \bar{k}_{xy}^\dagger P_{n_y}\bar{k}_{xy} + (g_x - g_y\bar{k}_{xy})^\dagger P_m(g_x - g_y\bar{k}_{xy}) \tag{5.49}$$

Note that for simplicity of the notation the variables in equation 5.47 through 5.49 are not written explicitly as a function of ω. The third term on the right side of equation 5.48 is the platform motion leaked to the noise estimation due to an error of the gain matching.

$$\begin{aligned} m(g_x - g_y\bar{k}_{xy}) &= m(g_x - g_y(C_{yy})^{-1}C_{xy}) \\ &= m(I - g_y(g_y^\dagger P_m g_y + P_{ny})^{-1}g_y^\dagger P_m)g_x \end{aligned} \tag{5.50}$$

Comparing to equation 5.23, $I - g_y(g_y^\dagger P_m g_y + P_{ny})^{-1}g_y^\dagger P_m$ can be interpreted as the generalized ratio between the noise and the total signal of y, which vanishes if $P_{ny} = 0$ and $\mathbf{Rank}(g_y) \geq \mathbf{Rank}(P_m)$. Equation 5.49 shows the P_{ϵ_x} is an estimation of the upper bound of noise level of the target sensor. The second term on the right side of equation 5.49 is the amount of reference sensor noise that is introduced into the target sensor noise estimation. Since P_{n_y} is diagonal,

$$\bar{k}_{xy}^\dagger P_{n_y}\bar{k}_{xy} = \sum |\bar{k}_{xyi}|^2 P_{n_{yi}}. \tag{5.51}$$

The Effect of Finite Data Points

Similar to the two sensor case in section 5.4.1, the effect of finite data points for multiple sensors can be analyzed by a sequence of equivalent optimization problems. Construct new variable

$$\grave{x} = x - y\bar{k}_{xy}. \tag{5.52}$$

We have

$$\mathbf{E}y^\dagger\grave{x} = \mathbf{E}y^\dagger(x - y\bar{k}_{xy}) = \mathbf{E}y^\dagger y\bar{k}_{xy} - \mathbf{E}x^\dagger x = 0. \tag{5.53}$$

Since $\dot{x}$ and all the columns of y are CGIEIRVV, $\dot{x}$ and y are independent. The expected value of the PSD of the residue is

$$\bar{P}_{\epsilon_x} = (1 - \frac{h}{n})P_{\dot{x}}(\omega). \tag{5.54}$$

Hence for h reference sensors, the expected value of the final estimated noise level is about $(1 - h/n)$ of the estimated noise level when n is infinite.

5.4.3   Noise Measurement Experiment

There are 39 sensors used on the ETF vibration isolation platform: on the first stage there are 6 capacitive position sensors, 6 L-4C seismometers and 9 STS-2 seismometers; on the second stage, there are 6 capacitive sensors, 9 GS-13 seismometers and 3 STS-2 seimometers. For details of the sensor setup please refer to chapter 7.

Time domain signal from all these sensors are collected for 1000 seconds with sampling frequency of 250 Hz. The time domain data are then transformed to the frequency domain by FFT and then divided into frequency bins. In each frequency bin there are 100 data points. The upper limit of the noise level of each sensor is obtained using the other 38 sensors as reference sensors. The PSD of the residue is then divided by $1 - 38/100$ to compensate the effect for finite number of data points in each frequency bin. As an example, the ASD of the signal and noise of one of the witness GS-13 sensors on the second stage is shown in figure 5.4. At 2 Hz and 10 Hz, where the signal has peaks, ASD of the sensor noise is obtained while the ASD of the signal is about 5×10^4 times higher. Due to the reason discussed before, the high signal to noise ratio actually helps to get a better measurement of the noise. Because of the high frequency resolution of the Daniell's frequency averaging method, the peaks in the signal at high frequencies are removed from the noise measurement. The fact that the noise curve is smooth through all the frequency range gives us confidence about this measurement. This measurement shows that the sensor's noise level at 1 Hz is about 1×10^{-10} meter per root Hz, which is too high for us to reach the performance requirement at 1 Hz for Advanced LIGO. More detailed study shows that the noise above 20 Hz is dominated by analog to digital ADC noise and the noise

below 20 Hz is dominated by sensor noise.
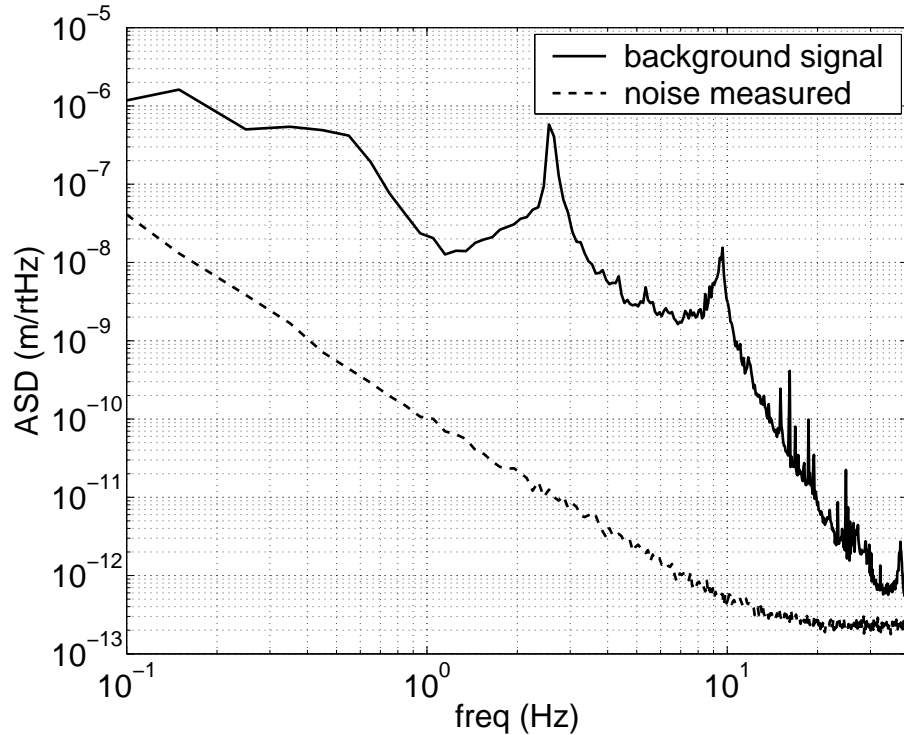
Figure 5.4: The ASD of the background signal and the noise of the GS-13 witness sensor on the second stage.

5.4.4   Measure the Noise Levels of Individual Sensors

One Degree of Freedom Case

Equation 5.24 shows that the noise of the two back to back sensors cannot be separated even if the signal to noise ratio of the sensors are high and the relative gain between the two sensors is exactly known. However, if there are three sensors that are used in the back to back measurement and the signal to noise ratios are high for every sensor, the noise of each individual sensors can be measured. When the signal to noise ratios of all the sensors are high, equation 5.24 becomes

$$P_{\epsilon_x}(\omega) = P_{n_x}(\omega) + |k_{xy}(\omega)|^2 P_{n_y}(\omega) \tag{5.55}$$

Similarly, we obtain

$$P_{\epsilon_y}(\omega) \;=\; P_{n_y}(\omega) + |k_{yz}(\omega)|^2 P_{n_z}(\omega); \tag{5.56}$$

$$P_{\epsilon_z}(\omega) \;=\; P_{n_z}(\omega) + |k_{zx}(\omega)|^2 P_{n_x}(\omega). \tag{5.57}$$

The noise of each sensor can be obtained by solving the linear equations 5.55 through 5.57. Note that there are 4 signal sources: the motion of platform and 3 sensor noises, but there are only 3 sensors. Although we can not measure the signals exactly, we can estimate theire PSD's.

Multi Degrees of Freedom Case

In a back to back noise measurement, the noise levels of individual sensors can be measured if three sensors are used on the single DOF platform. Similarly, on a platform that has multiple DOF's, we can measure the noise of an individual sensor if two independent virtual-gain-matched sensors can be constructed by linear combination of the reference sensors. For the example above, the platform has three degrees of freedom. Hence, if there are six reference sensors, we can divide the six reference sensors into two three-sensor groups and construct two independent virtual sensors from each group. Hence if the platform has d DOF, we need $1+2d$ sensors to measure the noise of each individual sensor. There is a way to use fewer sensors.

Consider all the sensors, including the target sensor and the reference sensors together. Denote the data point of all the sensors in a frequency bin as

$$z(\omega) = [x(\omega)\; y(\omega)]. \tag{5.58}$$

Hence,

$$z = mg_z + n_z, \tag{5.59}$$

where g_z is the gain of the sensors, and n_z is the noise of the sensors. g_z can be factored as:

$$g_z = g_g g_t, \tag{5.60}$$

where g_g is a real matrix that maps the platform motion m to the sensitive direction of the sensors, and g_t is a full rank complex diagonal matrix that represents the transfer functions of the sensors. The null space of g_g is denoted as a real matrix D_g. $D_z = g_t^{-1} D_g$ is the null space of g_z.

$$g_g D_g = 0 \Rightarrow \tag{5.61}$$

$$g_g g_t g_t^{-1} D_g = 0 \Rightarrow \tag{5.62}$$

$$g_z D_z = 0 \tag{5.63}$$

Use h to denote the total number of sensors. The rank of D_z and D_g are both $l = d - h$.

From equation 5.48 we have

$$\epsilon_x = [n_x \ n_Y] \begin{bmatrix} 1 \\ -\bar{k}_{xy} \end{bmatrix} + m[g_x \ g_y] \begin{bmatrix} 1 \\ -\bar{k}_{xy} \end{bmatrix}. \tag{5.64}$$

Denote

$$q_1 = \begin{bmatrix} 1 \\ -\bar{k}_{xy} \end{bmatrix}. \tag{5.65}$$

We have

$$\epsilon_{z_1} = n_z q_1 + m g_z q_1. \tag{5.66}$$

Considering all the sensors, have

$$\epsilon_z = n_z q + m g_z q, \tag{5.67}$$

where, $q = [q_1, q_2, ..., q_h]$, and

$$\epsilon_z = \begin{bmatrix} \epsilon_{z_1} \\ \epsilon_{z_2} \\ \vdots \\ \epsilon_{z_h} \end{bmatrix}. \tag{5.68}$$

If the signal to noise ratio of the sensors are high, from equation 5.51, we have:

$$
P_{\epsilon_{z1}} = P_{\epsilon_x} = [|q_{11}|^2 \; |q_{12}|^2 \; \ldots \; |q_{1h}|^2]
\begin{bmatrix}
P_{n_{z1}} \\
P_{n_{z2}} \\
\vdots \\
P_{n_{zh}}
\end{bmatrix}.
\tag{5.69}
$$

Define

$$
Q_1 = q_1^{|\tilde{2}|} = [|q_{11}|^2 \; |q_{12}|^2 \; \ldots \; |q_{1h}|^2],
\tag{5.70}
$$

where operator $\cdot^{|\tilde{2}|}$ denotes element-wise norm square.

$$
V =
\begin{bmatrix}
P_{n_{z1}} \\
P_{n_{z2}} \\
\vdots \\
P_{n_{zh}}
\end{bmatrix},
\tag{5.71}
$$

Similarly, we can repeat the process for each sensor and obtain $q_1,\ldots,\ q_{h-1}$. We have:

$$
U = QV,
\tag{5.72}
$$

where U is defined as

$$
U =
\begin{bmatrix}
P_{\epsilon_{z0}} \\
P_{\epsilon_{z1}} \\
\vdots \\
P_{\epsilon_{zh}}
\end{bmatrix}.
\tag{5.73}
$$

and matrix Q is defined as

$$
Q = q^{|\tilde{2}|} =
\begin{bmatrix}
|q_{11}|^2 & |q_{12}|^2 & \ldots & |q_{1h}|^2 \\
|q_{21}|^2 & |q_{22}|^2 & \ldots & |q_{1h}|^2 \\
\vdots & \vdots & \ddots & \vdots \\
|q_{h1}|^2 & |q_{h2}|^2 & \ldots & |q_{hh}|^2
\end{bmatrix}
\tag{5.74}
$$

If Q has rank h, the individual noise levels U can be obtained by solving equation 5.72. First, let us study the rank of the Q when the noise levels of the sensors are zero. When there is no sensor noise, from equation 5.66,

$$mg_z q_1 = 0, \tag{5.75}$$

which has to be true for any m. Choose $m = I$, we have

$$g_z q_1 = 0. \tag{5.76}$$

From equation 5.60 and that D_g is the null space of g_g,

$$g_t q_1 = D_g \alpha_1. \tag{5.77}$$

where α_1 is real a vector with l elements. Similarly, we have

$$g_t q = D_g \alpha, \tag{5.78}$$

where $\alpha = [\alpha_1, \alpha_2, ..., alpha_h]$. Since g_t is diagonal,

$$(g_t q)^{|\tilde{2}|} = g_t^{|\tilde{2}|} q^{|\tilde{2}|} = g_t^{|\tilde{2}|} Q. \tag{5.79}$$

Define
$$Q_g = (g_t q)^{|\tilde{2}|} = (D_g \alpha)^{|\tilde{2}|}. \tag{5.80}$$

Since g_t is full rank, Q_g has the same rank as Q. Since $D_g \alpha$ is real, the element of Q_g is given by

$$\begin{aligned} Q_{gij} &= (\sum_w D_{gjw} \alpha_{iw})^2 \\ &= \sum_w \sum_u \alpha_{iw} \alpha_{iu} D_{jw} D_{gju} \end{aligned} \tag{5.81}$$

Hence Q_g can be factored as

$$Q_{gij} = AB^T \tag{5.82}$$

$$A = \begin{bmatrix} D_{g11}^2 & D_{g11}D_{g12} & \ldots & D_{g11}D_{g1l} & D_{g12}D_{g11} & D_{g12}^2 & \ldots & D_{g1l}^2 \\ D_{g21}^2 & D_{g21}D_{g22} & \ldots & D_{g21}D_{g2l} & D_{g22}D_{g21} & D_{g22}^2 & \ldots & D_{g2l}^2 \\ \vdots & \vdots & \ddots & \vdots & \vdots & \vdots & \ddots & \vdots \\ D_{gh1}^2 & D_{gh1}D_{gh2} & \ldots & D_{gh1}D_{ghl} & D_{gh2}D_{gh1} & D_{gh2}^2 & \ldots & D_{ghl}^2 \end{bmatrix} \tag{5.83}$$

$$B = \begin{bmatrix} \alpha_{11}^2 & \alpha_{11}\alpha_{21} & \ldots & \alpha_{11}\alpha_{l1} & \alpha_{21}\alpha_{11} & \alpha_{11}^2 & \ldots & \alpha_{l1}^2 \\ \alpha_{12}^2 & \alpha_{12}\alpha_{22} & \ldots & \alpha_{12}\alpha_{l2} & \alpha_{22}\alpha_{22} & \alpha_{22}^2 & \ldots & \alpha_{l2}^2 \\ \vdots & \vdots & \ddots & \vdots & \vdots & \vdots & \ddots & \vdots \\ \alpha_{1h}^2 & \alpha_{1h}\alpha_{2h} & \ldots & \alpha_{1h}\alpha_{lh} & \alpha_{2h}\alpha_{1h} & \alpha_{2h}^2 & \ldots & \alpha_{lh}^2 \end{bmatrix} \tag{5.84}$$

A and B are both h by l^2 matrices. There are $\frac{l(l+1)}{2}$ different columns in each matrix. There exist $\alpha \in \Re^{h \times l}$ such that $\mathbf{Rank}(B) = \min(h, \frac{l(l+1)}{2})$. For example let

$$\alpha_{iw} = \alpha_{1w}^{2^{i-1}} \tag{5.85}$$

and

$$\alpha_{1w} \neq 0; \ \alpha_{1w} \neq \alpha_{1v} \text{ unless } w = v. \tag{5.86}$$

and B becomes,

$$B = \begin{bmatrix} \alpha_{11}^{2^0+2^0} & \alpha_{11}^{2^0+2^1} & \ldots & \alpha_{11}^{2^0+2^l} & \alpha_{11}^{2^1+2^0} & \alpha_{11}^{2^1+2^1} & \ldots & \alpha_{11}^{2^{l-1}+2^{l-1}} \\ \alpha_{12}^{2^0+2^0} & \alpha_{12}^{2^0+2^1} & \ldots & \alpha_{12}^{2^0+2^l} & \alpha_{12}^{2^1+2^0} & \alpha_{12}^{2^1+2^1} & \ldots & \alpha_{12}^{2^{l-1}+2^{l-1}} \\ \vdots & \vdots & \ddots & \vdots & \vdots & \vdots & \ddots & \vdots \\ \alpha_{1h}^{2^0+2^0} & \alpha_{1h}^{2^0+2^1} & \ldots & \alpha_{1h}^{2^0+2^l} & \alpha_{1h}^{2^1+2^0} & \alpha_{1h}^{2^1+2^1} & \ldots & \alpha_{1h}^{2^{l-1}+2^{l-1}} \end{bmatrix} \tag{5.87}$$

In the first row of B, all the elements are powers of α_{11}. In binary format, the powers are sum of two l digits numbers. For each of the two binary numbers, one digit is 1 and rest of digits are 0. From Vandermonde matrix theory, the rank of B is $\min(h, \frac{l(l+1)}{2})$. Hence, it is possible to measure the noise level of each individual sensor if

$$h \leq \frac{l(l+1)}{2} \Rightarrow l \geq \frac{1 + \sqrt{1+8d}}{2} \tag{5.88}$$

For $d = 3$, we have $l \geq 3$. So on a platform with 3 DOF, we need 6 sensors to

measure the noise of each of them. Practically, we do not construct the matrix α and D_g by equation 5.85. We just observe the singular value of matrix Q to make sure that it can be reliably inverted. An experiment to demonstrate this idea will make an interesting future project for sensor noise measurement.

5.4.5 Discussion

One of the advantages of measuring noise levels of multiple sensors simultaneously on a multiple DOF platform is that it can be used directly on the isolation system itself. In fact, the vibration isolation system itself can be used to control the amplitude sensor signals such that they would not go out of the dynamic ranges of the sensors.

Equation 5.25 and 5.50 show that if the sensors have enough linear dynamic range it might be beneficial to drive the platform to increase the signal to noise ratio such that a better measurement of sensor noise level can be obtained.

It should be noted that there are some problems with this noise measurement method. First, it assumes that the noise of different sensors are incoherent. However, practically it might not be true. For example, if all the seismometers are sensitive to the electromagnetic noise generated from the same noise source, that noise will be considered as signal by the algorithm and thus not counted as sensor noise. Secondly, the sensors are assumed to be linear over the dynamic ranges. If they are not, the noise measurement will have an error. So, linearity of the sensors should be evaluated when this linear noise measurement technique is used.

Chapter 6

Nonlinear MIMO System Analysis

6.1 Introduction

The vibration isolation and alignment system proposed for LIGO is a complicated multi-input multi-output (MIMO) system. To fully understands its behavior, MIMO nonlinear analysis is necessary. For example, the nonlinear tilt horizontal coupling at low frequencies needs to be carefully studied. In this chapter, we will discuss the tools to analyze the nonlinearity of MIMO the systems.

A model of MIMO nonlinear system is shown in figure 6.1. The whole system is composed of the actuators, the sensors, and the plant. The actuators and the sensors are single-input-single-output(SISO) systems. An actuator takes commands from an input and acts accordingly on the plant. A sensor observes the plant in a certain direction and generates an output signal. Any part of the system can be nonlinear.

It might seem that the problem is made unnecessarily complicated when we separate the actuators and the sensors from the MIMO plant, rather than considering everything as a whole MIMO system together. However, it is worth the effort for two reasons. First, in many practical situations, the sensors and actuators are naturally separated from the plant. Keeping them separated in the model helps us to maintain good intuition about the real system. For example, in a satellite control system, the plant is the satellite body, the actuators are the thrusters, and the sensors are, for
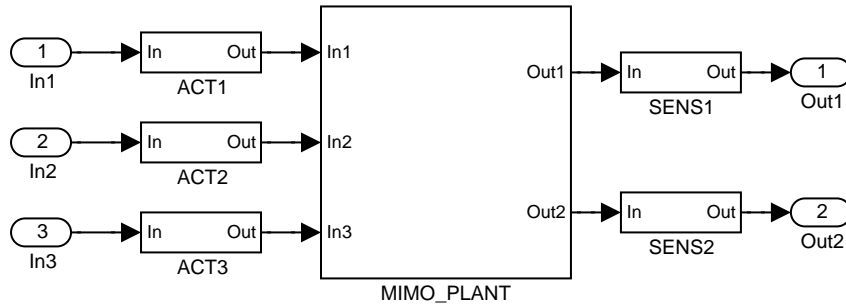
Figure 6.1: A three-in-two-out nonlinear system

example, gyroscopes. Each of these parts has its unique physical characters. Second, the actuators and sensors are often the dominating nonlinear parts of the whole system. In those cases, keeping them as separate SISO systems helps to isolate the problem.

When we drive a nonlinear system with a set of sine functions at different frequencies, the output contains not only those driving frequency components but also some harmonic frequency components. For example, in the system shown in figure 6.1, if we use frequency f_1, f_2 and f_3 to drive actuator 1,2 and 3 respectively, the sensor outputs may contain any frequency component F that satisfies:

$$F = a_1 \cdot f_1 + a_2 \cdot f_2 + a_3 \cdot f_3, where\ a_1, a_2, a_3 \in \mathbb{Z}. \tag{6.1}$$

When $(a_1, a_2, a_3) = (1, 0, 0)$, $F = f_1$, which is the first driving frequency. When $(a_1, a_2, a_3) = (0, 0, 2)$, $F = 2f_3$, which is the second order harmonic of driving frequency f_3. When $(a_1, a_2, a_3) = (0, 0, 0)$, $F = 0$, which is DC component.

Definition 6.1.1. *The collection of all input frequencies is defined as the input frequency vector $f = (f_1, f_2, ..., f_n)$, $f \geq 0$.*

Each actuator's input signal is a linear combination of sinusoidal functions whose frequencies come from the input frequency vector. In general, the qth input signal is

$$U_q(t) = \sum_{n=1,...,n_p} \beta_{qn} cos(2\pi f_{qn} t + \phi_{qn}) = \mathbb{R}(\sum_{n=1,...,n_p} \lambda_{qn} e^{i2\pi f_{qn} t}), \tag{6.2}$$

where $\lambda_{qn} = \beta_{qn}e^{i\phi_{qn}}$ is a complex number.

Definition 6.1.2. *Define $\Lambda_q = (\lambda_{q1}, ..., \lambda_{qn})$ as the input coefficient vector of the qth input.*

In general, the *pth* sensor's output Y_p can be written as a linear combination of all possible harmonics, which are shown as spikes in the frequency spectrum plot.

$$Y_p = \mathbb{R}(\sum_{j=0,...\infty} \gamma_{pj}e^{i2\pi F_j t}). \tag{6.3}$$

Definition 6.1.3. *Each harmonic has four properties which are defined as follows.*

1. *F_j called the frequency of jth harmonic.*

2. *γ_{pj} is the coefficient of jth harmonic in pth output.*

   Each harmonic frequency is a linear combination of the input frequencies with integer coefficients.

   $$F_j = \sum_{m=1,...n} a_{mj}f_m, \ a_{mj} \in \mathbb{Z} \tag{6.4}$$

3. *$A_j = (a_{1j}, ..., a_{nj}), a_{mj} \in \mathbb{Z}$ is defined as the harmonic number vector of jth harmonic.*

4. *$O(A) = \sum_{m=1,...,n}|a_m|$ is defined as the order of the harmonic vector A, or simply, the order of the harmonic. The order of a harmonic indicates the level of the system's nonlinearity that the harmonic represents. The harmonics with order zero and one are related to the zero frequency and the linear terms of the system. The higher order harmonics betray the nonlinear properties of the system. The highest order of the harmonics with nonzero coefficients indicates how nonlinear the system is.*

   Two harmonics are the same iff all these four properties are the same.

The nonlinear system identification is done in five steps.

1. Construct the input signal by selecting the appropriate input frequency vector and input coefficient vectors.

2. Find an appropriate maximum harmonic order, O_{max}, based on the physical characteristics of the system. Construct all possible harmonic number vectors whose harmonic order is less than or equal to O_{max}. Find the frequency of each harmonic using equation 6.4.

3. Drive the system and observe the outputs of all sensors. Find the coefficient of each harmonic frequency for each output by Fourier transform.

4. Associate the harmonic number vectors with the harmonic coefficients by comparing their frequencies generated in step two and three. Thus all four properties off each harmonic are identified.

5. Use the properties of all the harmonics to identify the physical model of the system.

In the above procedure, we might have some trouble in step four if two harmonics have the same associated frequency. For example, if the input frequency vector is $(f_1, f_2) = (2, 3)$, then $A_{j1} = (3, 0)$ and $A_{j2} = (0, 2)$ will have the same frequency $F_{j1} = F_{j2} = 6$. Only one coefficient can be identified for the shared frequency, $F = 6$, and it is not clear which of the two different harmonic number vectors it should be associated with. This is called the *harmonic frequency overlapping problem* (HFOP). It should be mentioned that if the input frequency vector contains only one frequency, f, HFOP do not exist. In that case, the harmonic frequency is given by:

$$F_j = j * f. \tag{6.5}$$

So, A_j is a scaler, $A_j = (j)$, and no two harmonics share the same associated frequency. However, for nonlinear MIMO system identification, in which multiple input frequencies are often needed, HFOP can easily happen if the input frequency vector is not carefully selected.

In this chapter, we are going to propose an algorithm using linearly prime integer number frequencies (LPINF) to construct the input frequency vector so that HFOP can be avoided. The basic theory of LPINF is shown in section 6.2. Following that, three examples about how to use LPINF in MIMO nonlinear system identification are

demonstrated in section 6.3, 6.4, and 6.5. Note that nonlinear analysis using Voltera kernals has been thoroughly studied for SISO systems [10] [13] [17]. Efficient ways to measure Voltera kernals at multiple frequency points using number theory has been proposed [10], [17]. In this chapter, we focus on nonlinear analysis for MIMO systems. We are not trying to measure the full Voltera kernals. Rather, we just try to analyze some aspects of the whole systems. Interestingly, the linearly prime integer numbers can be used to measure the SISO Voltera kernals with high order nonlinearity in ways similar to [10], [17].

6.2 Linearly Prime Integer Number Frequencies

To prevent HFOP, the input frequencies have to be carefully selected such that it can be guaranteed that if two harmonics have the same frequency then they must have the same harmonic number vector, i.e.,

$$F_1 = F_2 \implies A_1 = A_2. \tag{6.6}$$

This implies if

$$\sum_{m=1,...n} a_{m1} f_m = \sum_{m=1,...n} a_{m2} f_m, \ a_{mi} \in \mathbb{Z}, \tag{6.7}$$

i.e.,

$$\sum_{m=1,...n} (a_{m1} - a_{m2}) f_m = 0, \tag{6.8}$$

then

$$(a_{m1} - a_{m2}) = 0, \ i.e., \ a_{m1} = a_{m2}. \tag{6.9}$$

If another harmonic number vector, $A_d = A_1 - A_2$, is introduced, then the statement above becomes:

$$\sum_{m=1,...,n} a_{md} f_m = 0, \ a_{md} \in \mathbb{Z} \implies a_{md} = 0. \tag{6.10}$$

In this section,we are going to discuss how to select the input frequencies so that the statement in equation 6.10 is assured.

6.2.1   Linearly Prime Harmonics

If only integer number frequencies are used as input frequencies, i.e. $f_i = \omega_i/T$, the statement 6.10 becomes a statement about integer numbers:

$$\sum_{m=1,\ldots,n} a_{md}\omega_i = 0, \ a_{md}, \ \omega_i \ \in \mathbb{Z} \Longrightarrow a_{md} = 0. \tag{6.11}$$

In vector form,

$$A_d F^T = 0, \ A_d, F \in \mathbb{Z}^n \Longrightarrow A_d = 0. \tag{6.12}$$

If no other constraints are applied to the harmonic number vector, the statement 6.12 is not true, because $a_1 = \omega_2$, $a_2 = -\omega_1$, $a_i = 0$ for $i > 2$, is an obvious counter example. First, we can constrain the order of the harmonic number vector.

Definition 6.2.1. *If*

$$A_d F^T = 0, \ O(A_d) \le \sigma, \ A_d, \ F \in \mathbb{Z}^n \Longrightarrow A_d = 0, \tag{6.13}$$

then F is called linearly prime up to order σ.

Note that σ indicates the F's ability to avoid HFOP. If the order of nonlinearity of the system is denoted as ρ, and $\sigma > 2\rho$, then HFOP can be avoided. Since

$$F_d = F_2 - F_1, \tag{6.14}$$

the order of them satisfies

$$O_d \le O_2 + O_1 \le 2\rho = \sigma. \tag{6.15}$$

In practice, the range from which we can choose input frequency numbers is also constrained. Typically, $\omega_i < \omega_{max}$. Thus the input frequency vector construction problem becomes the following integer optimization problem:

$$\max \ \sigma \ \| \ \omega_i \le \omega_{max}. \tag{6.16}$$

Or equivalently,

$$\max_{\Omega}(\min_{A} \sum_i |a_i| \; \| A\Omega^T = 0, \; A \neq 0, \; \omega_i \leq \omega_{max}, \; A, \; \Omega \in \mathbb{Z}^n). \tag{6.17}$$

For $n = 1$, the solution of this problem is simply $\omega_1 = \omega_{max}$. For $n = 2$, the solution is also simple: $\omega_1 = \omega_{max}$, $\omega_2 = \omega_{max} - 1$. Since ω_1 and ω_2 are relatively prime to each other, $a_1 = \omega_2$, $a_2 = -\omega_1$ is the optimal solution for 6.17. However, for $n > 2$, the optimal solutions of 6.17 are much harder to find. The brute force algorithm takes about $(f_{max})^n$ calculations to solve this problem.

So far, the optimal solution for 6.17 remains unknown to us. Here, we propose a suboptimal approach based on following theorem.

Theorem 6.2.2. *If n positive integer numbers, $p_1 < p_2 < ... < p_n$, are relatively prime to each other, then the frequency numbers given by*

$$\omega_i = \prod_{j \neq i} p_j \tag{6.18}$$

are linearly prime up to order $p_1 + p_2$.

Proof. Suppose $A^t \Omega = 0$, we have

$$\sum_{i=1,...,n} a_i \omega_i \;\; = \;\; 0 \tag{6.19}$$

$$- \sum_{i=2,...,n} a_i \omega_i \;\; = \;\; a_1 \omega_1 \tag{6.20}$$

$$-p_1 \sum_{i=2,...,n} (a_i \prod_{j \neq i,1} p_j) \;\; = \;\; a_1 \prod_{j \neq 1} p_j. \tag{6.21}$$

Because the left side of equation 6.21 is a multiple of p_1, the right side must also be a multiple of p_1. Because p_2, ..., p_n, are relatively prime to p_1 by the assumption above, a_1 must be a multiple of p_1. Similarly, a_i must be a multiple of p_i for $i = 2, ..., n$. If one term in a_1, ..., a_n is nonzero, then there must be another term that is also

nonzero. Otherwise equation 6.19 is not true. Hence, if $A \neq 0$,

$$O(A) \geq p_1 + p_2. \tag{6.22}$$

$\square$

Note that when $n = 2$, $\omega_1 = p_2$ and $\omega_2 = p_1$. Hence, the 'linearly prime numbers' can be considered as a generalization of the 'relative prime numbers' to the case with more than two numbers.

Using theorem 6.2.2, the input frequency vector can be easily constructed by finding a set of appropriate relative prime numbers. For example, when $n = 3$ and $\omega_{max} = 100$, we can choose $p_1 = 7$, $p_2 = 9$, and $p_3 = 10$. Therefore, the input frequency number vector is $\Omega = (63, 70, 90)$, which is linearly prime up to order 15. Approximately, this suboptimal approach generates input frequency numbers that are linearly prime up to order $2 \sqrt[n-1]{\omega_{max}}$.

6.3   Isolate the Nonlinearities to Actuators in MIMO System

In a feedback control system, accuracy requirement on actuators are generally less than that on sensors. Therefore, in many practical nonlinear systems, the dominating nonlinear parts are the actuators. In this section, we are going to study the characteristic pattern of harmonics of such systems.

For a SISO system, it is impossible to isolate the nonlinearity to any specific part. The input signal goes through a single path in the system: from the actuator to the plant, and then to the sensor. Any one of these three parts can be nonlinear, and the harmonic generated by such nonlinearities can not be distinguished from that generated by another.

It might be surprising that for more complicated MIMO systems, nonlinearity isolation is possible. The idea is actually very simple: we can 'color' the input signals using different frequencies and by observing those 'colors' at the output, we can find
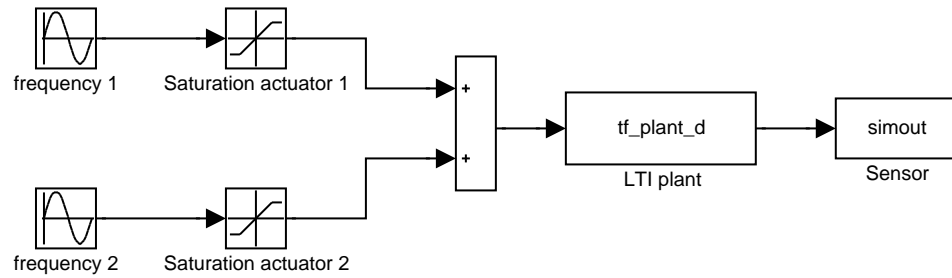
Figure 6.2: A two-in-one-out nonlinear system. The two actuators are nonlinear: they saturate when the magnitude of the drive signal is larger than 0.7. The plant and the sensor are linear.

where the nonlinearity is. Particularly, use a sinusoidal signal of frequency f_1 to drive actuator 1, frequency f_2 to drive actuator 2, and so on. These frequencies, f_1, f_2, etc., are linearly prime frequencies. Because each actuator is a SISO system, no matter what kind of nonlinearity it has, it can only generate harmonics of its own input frequency. For example, actuator 1 can only generate harmonics with frequency 0, f_1, $2f_1$, $3f_1$, and so on. If the plant and the sensors are linear, no other harmonics can be generated. Thus the sensors can only observe harmonics whose frequencies can be expressed as nf_i, where n is an integer. This feature of output harmonics can be used as a signature to identify actuator nonlinearity.

Let us study an example. Figure 6.2 shows a two input one output system. Actuators are the only nonlinear parts in this system: they saturate when the magnitude of the drive signal is larger than 0.7. The plant is a simple second order linear time invariant (LTI) system whose frequency responses are shown in figure 6.3. The sensor is a simple proportional observer with unit gain. The frequencies of the sinusoid signals are $f_1 = 23$ Hz and $f_2 = 17$ Hz. The magnitude of each is one. Figure 6.4 shows the time history of the sensor's output. The data collection time is one second. Figure 6.5 shows the magnitude of the Fourier transform of the output signal. The spikes at 17 and 23 Hz come from the driving frequencies. The other spikes at higher frequencies are the harmonics of higher orders. Note that because all the harmonics are integer number frequencies, all the spikes are very sharp. Using the procedure described in section 6.1, we can obtain the four properties of all the harmonics. Figure 6.6 is a

plot of the log magnitude of harmonic coefficients of different harmonic orders. The high magnitude harmonics show up only in the first row and the first column because those frequencies are harmonics of either f_1 or f_2, but not any combination of them. This signature is just what we are looking for.

6.4   Isolating the Nonlinearities to Sensors

If the actuators and the plant are linear, then the inputs to the sensors are a linear combination of sinusoid signals with the same frequencies as the input signals. For example, if the input the frequencies are f_1 and f_2, then the input signal to the first sensor has the form:

$$g(t) = \alpha_1 \cos(f_1 2\pi t + \phi_1) + \alpha_2 \cos(f_2 2\pi t + \phi_2). \qquad (6.23)$$

In general, the combination coefficients α_i and the phases ϕ_i are not known. We assume the sensor's output output signal is a scalar function of its input signal which can be represented by a mth order Taylor series:

$$Y = Y(g) = \sum_{i=0...m} \nu_i g^i. \qquad (6.24)$$

It is a little more difficult to isolate nonlinearity to the sensors than to the actuators. From equation 6.23 and 6.24, we can see that nonlinear sensors can generate many more number of harmonics than nonlinear actuators. Furthermore, the order vectors of those harmonics do not have an obvious structure that can be used to distinguish sensor nonlinearity from plant nonlinearity.

Fortunately, a rather simple algorithm exists to identify sensor nonlinearity given by equation 6.23 and 6.24. In order to simplify the notation, introduce two variables
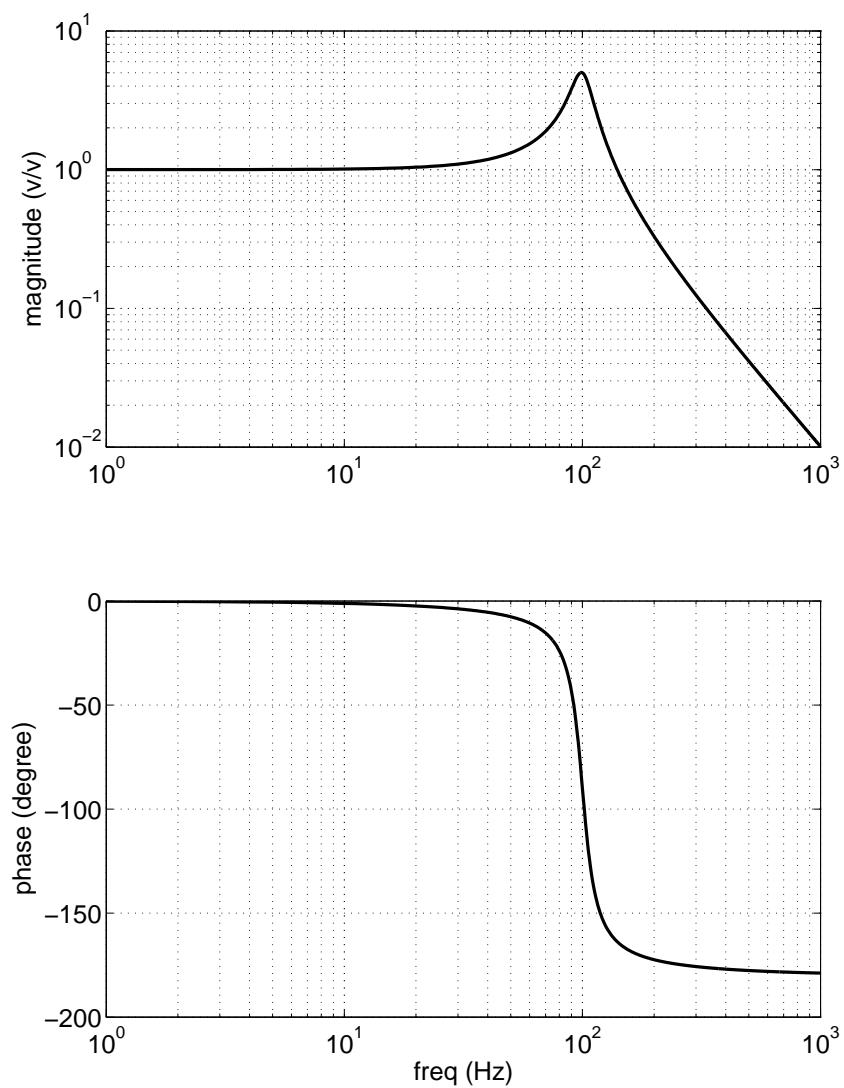
Figure 6.3: Frequency Responds of the plant. The plant is a simple second order LTI system with resident frequency of 100 Hz.
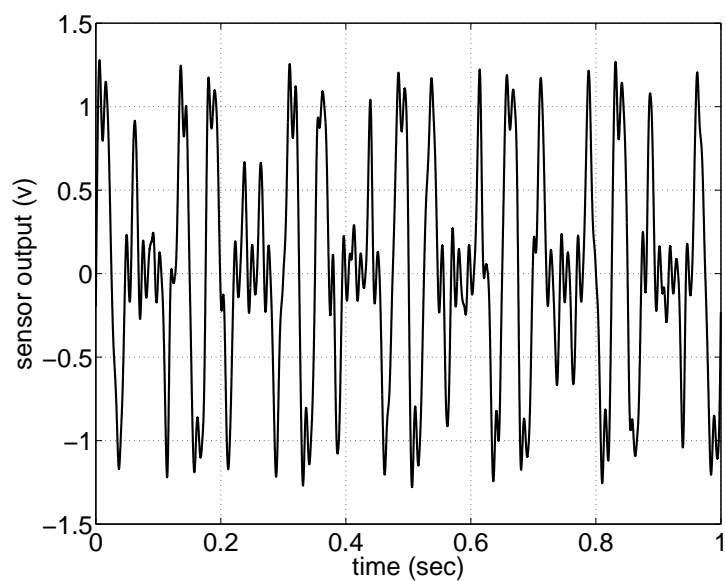
Figure 6.4: Time history of the sensor's output.
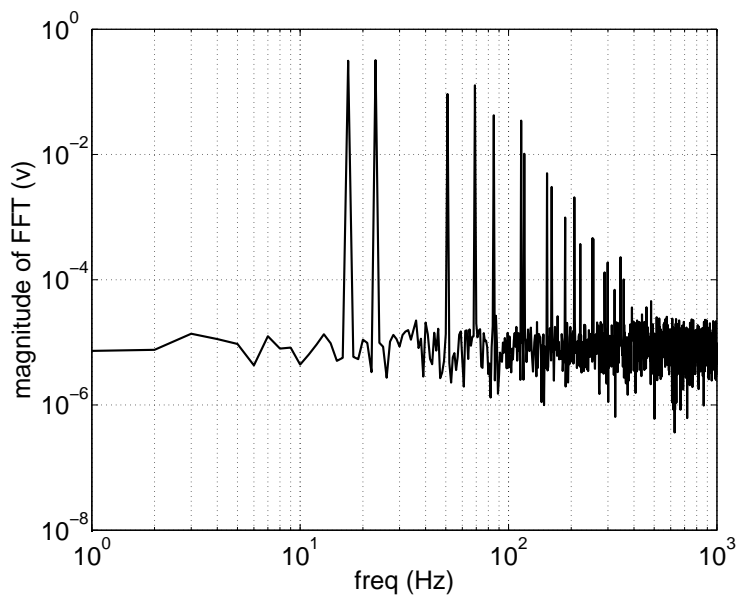
Figure 6.5: FFT of the sensor's output.
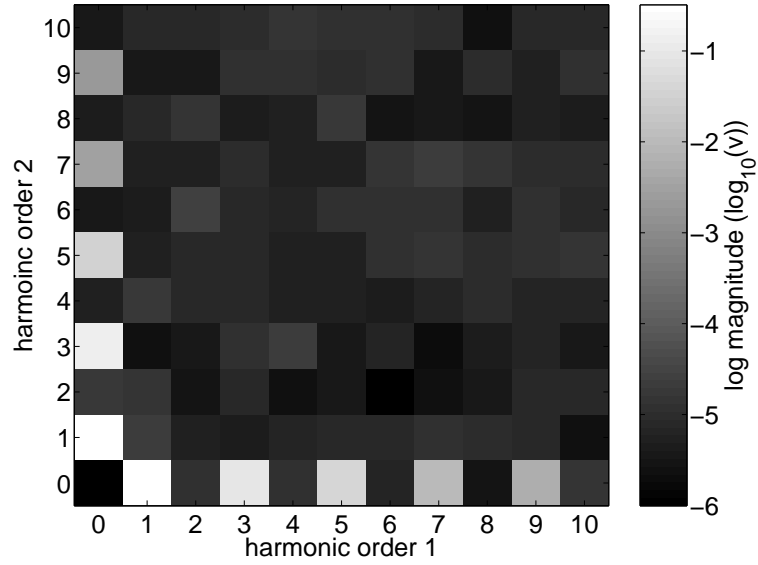
Figure 6.6: Log magnitude of harmonic coefficients of different harmonic orders. The fact that high magnitudes, represented as light blocks, show up only in the first row and the first column indicates actuator nonlinearity.

to represent the two frequency components in the input signal g.

$$g_1 = \alpha_1 \cos(f_1 2\pi t + \phi_1), \tag{6.25}$$

$$g_2 = \alpha_2 \cos(f_2 2\pi t + \phi_2). \tag{6.26}$$

$$\tag{6.27}$$

Thus, we have

$$g = g_1 + g_2; \tag{6.28}$$

$$Y(g_1, g_2) = Y(g_1 + g_2). \tag{6.29}$$

Note that the level curves (contour plot) of $Y(g_1, g_2)$ are straight lines on the (g_1, g_2) plane.

From equation 6.23 and 6.24, it can be easily identified that the first order harmonics in Y have the same phase as g_1 and g_2. By measuring the two phases, we can
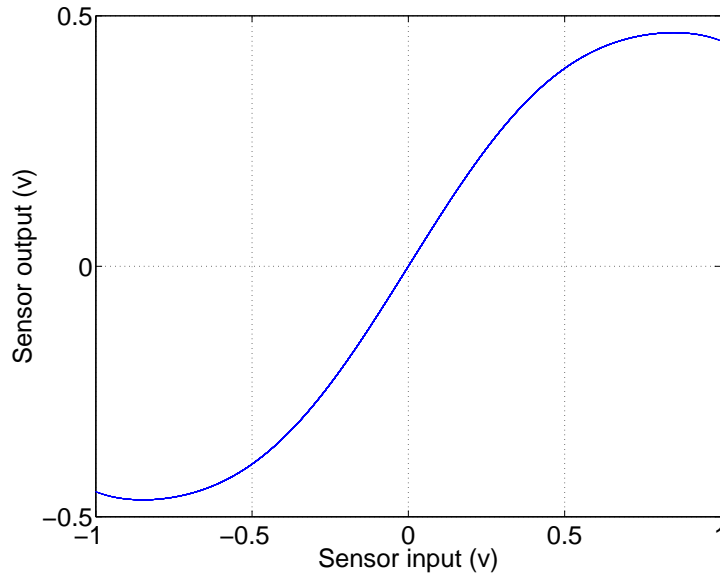
Figure 6.7: Scalar nonlinear function of the sensor.

construct two sinusoid signals:

$$g_1' \quad = \cos(f_1 2\pi t + \phi_1), \tag{6.30}$$

$$g_2' \quad = \cos(f_2 2\pi t + \phi_2). \tag{6.31}$$

$$\tag{6.32}$$

Thus, we can construct function $Y(g_1', g_2')$. Because $Y(g_1', g_2')$ is obviously a linear transform of $Y(g_1, g_2)$, its level curves are also straight lines. Therefore, sensor nonlinearity can be identified by those straight equal-level lines.

The upper algorithm is applied to a simulated example, in which $\alpha_1 = 0.7, \phi_1 = 0.2$, $\alpha_1 = 0.3$, $\phi_1 = -0.5$. The nonlinear scalar function of the sensor is

$$Y = g - g^3 + 0.7g^5 - 0.25g^7, \tag{6.33}$$

which is plotted in figure 6.7. The time history of steady state output from the sensor is shown in figure 6.8.
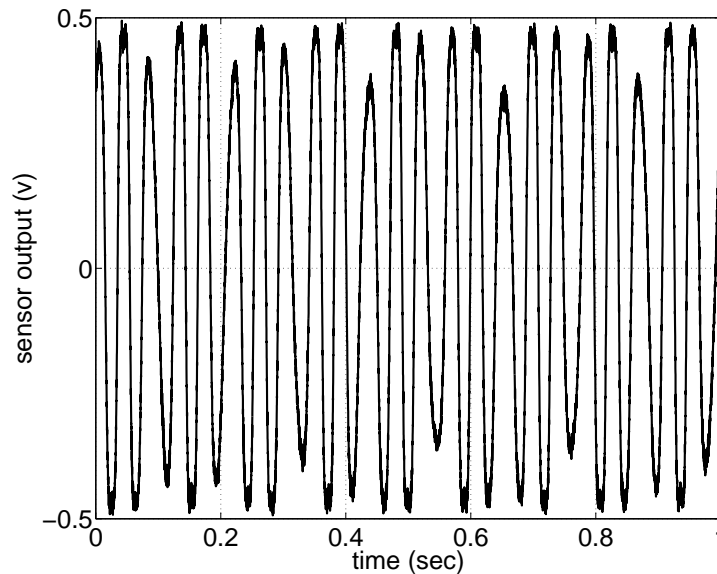
Figure 6.8: Time history of the sensor output.

The level curves of the sensor output as a function of the two frequency compo-nents of the sensor input, i.e. $Y(g'_1, g'_2)$, is plotted in figure 6.9. As we can see, the level curves are straight lines up the accuracy determined by the sensor noise.

One remark that we want to make is that the accuracy of the phase measurement is critical in this algorithm. Figure 6.10 shows the equal-level of sensor output as a function of actuator output. Because the phases of the actuator inputs are different from the phase of the sensor inputs, the level curves are not even close to straight lines in figure 6.9. In fact figure 6.10 is a typical picture of plant nonlinearity. Also, we would like to note that the linear prime number frequencies prevent higher order harmonics from falling on the frequency of the first order harmonics, and thus keep the phase measurement of the first order harmonics accurate.

6.5 Nonlinear Tilt-Horizontal Coupling

In previous chapters, it was shown that nonlinear tilt horizontal coupling of low frequency isolation system can be dramatically reduced by high gain feedback loops in
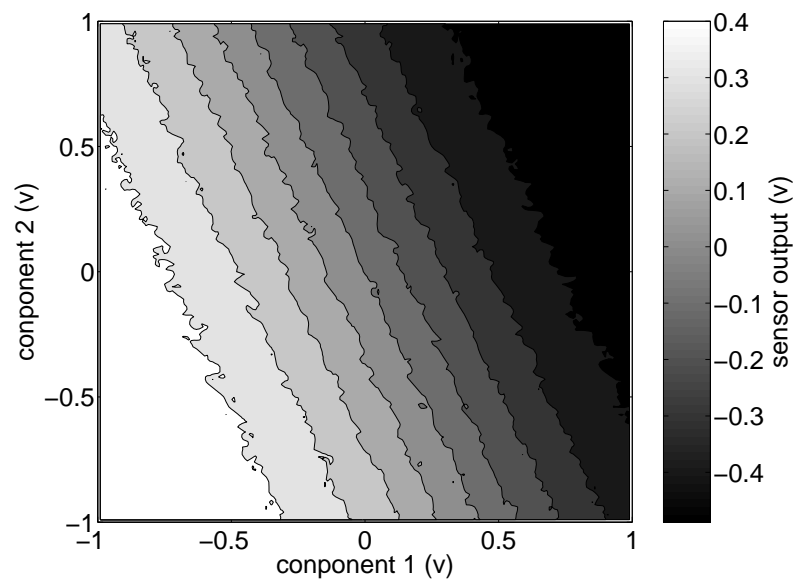
Figure 6.9: Level curves of sensor output as a function of two frequency components of the sensor input.
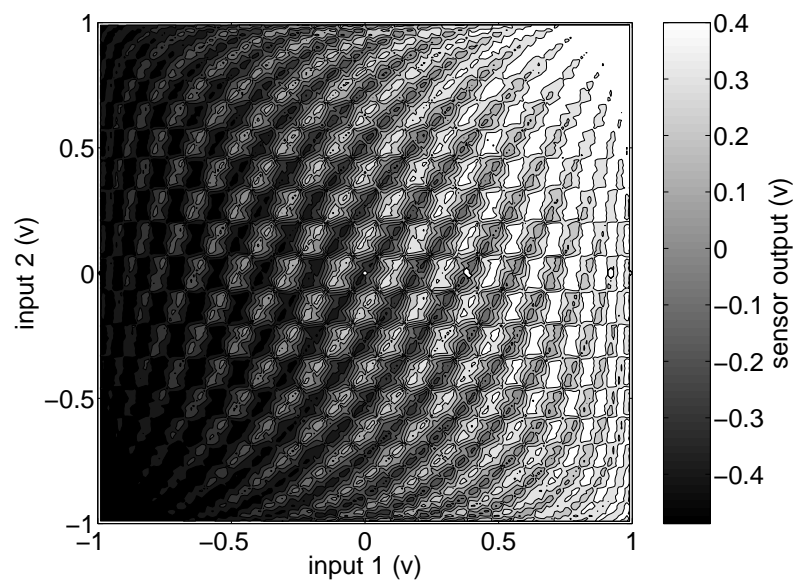

Figure 6.10: Level curves of sensor output as a function of actuator output.
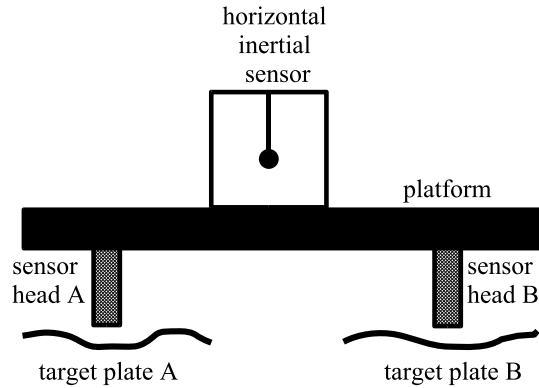
Figure 6.11: Nonlinear tilt horizontal coupling caused by the non-flat target plates of the vertical capacitive position sensors.

the tilt direction. In that situation, the tilt horizontal coupling effect is dominated by the capacitive position sensors. A capacitive position sensor measures the electrical capacity between a sensor head and a target plate and then deduces the relative distance between them. If the target plate of a vertical capacitive position sensor is not flat, the sensors output will not only be a function of the distance between the sensor heads and the target plate in the vertical direction, but also a function of the sensor head's horizontal position relative to the target plate. Hence, nonlinear tilt motion could be generated when the platform is moved horizontally, as shown in figure. 6.11.

For example, an experiment to study the nonlinear tilt horizontal coupling when the system is controlled in done on the ETF vibration isolation system. The two stage system is controlled in all 12 degrees of freedom. The open loop gains of the tilt controllers are more than 10^4 below 0.1 Hz. The blending frequencies between the position sensors and inertial sensors are at about 2 Hz. Hence, the position sensor signal will dominate the feedback signal below 2 Hz. The choice of this blending frequency is to simplify the platform dynamics at low frequencies where the tilt-horizontal coupling is studied. When the platform is in vibration isolation mode, the blending frequency will be moved lower. The local coordinates of the target plates of the three vertical position sensors on the first stage are shown in figure 6.12.
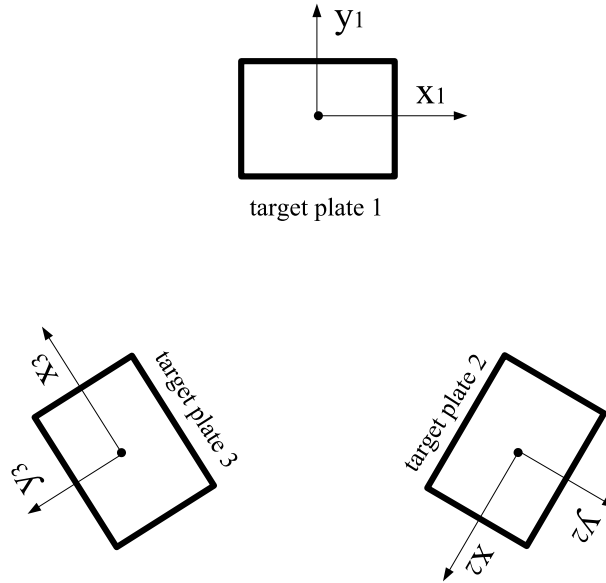
Figure 6.12: Local coordinates of the target plates of the three vertical capacitive position sensors.

There is one horizontal position sensor and one horizontal STS2 inertial sensor at each corner. Both of them are sensitive along the x direction. The platform of the first stage is driven to move horizontally by injecting three sinusoidal signals at the offset of the horizontal position sensors. The frequency numbers of the drive signals are 11×12, 11×13, and 12×13 for sensor 1, 2 and 3. The common period of the three signals is 2000 seconds. Hence, the frequencies of the sinusoid signals are $f_1 = 0.066$ Hz, $f_2 = 0.0715$ Hz and $f_3 = 0.078$ Hz. The magnitudes of the drive signals are 150 μm (i.e. peak to peak value of 300 μm). The data collection time is 4000 seconds. The Fourier transforms of the outputs of three horizontal STS2 sensors are shown in figure 6.13. The second order harmonics at frequencies of $f_2 - f_1 = 0.0055$ Hz, $f_3 - f_2 = 0.0065$ Hz, and $f_3 - f_1 = 0.012$ Hz are generated by tilt horizontal coupling. The sum of the three identical inertial sensors measures the rotation of the platform along the vertical axis and it is not sensitive to tilt motion. The fact that this signal's second order harmonics vanish in the background noise indicates that the three sensors are quite linear and the second order harmonics in the individual
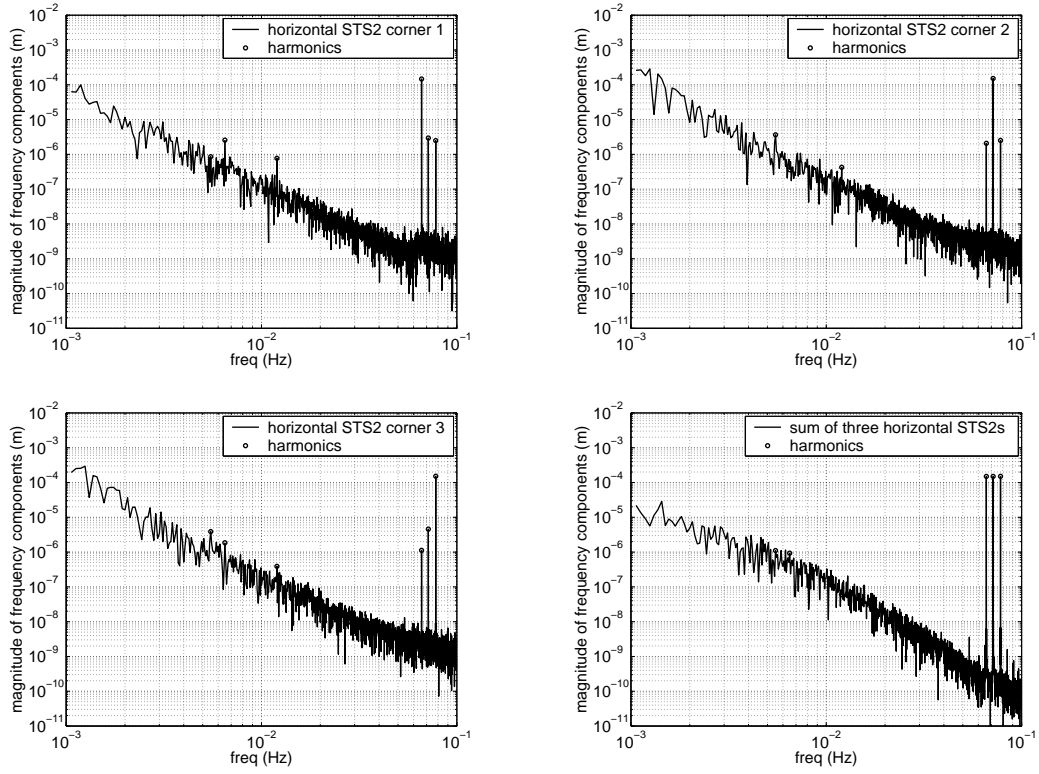
Figure 6.13: The output of the STS-2 inertial sensors when the platform is driven to move by three sinusoidal signals at frequencies $f_1 = 0.066$ Hz, $f_2 = 0.0715$ Hz and $f_3 = 0.078$ Hz. The first and second order harmonics are marked with little circles in the plots. The second order harmonics are at frequencies of $f_2 - f_1 = 0.0055$ Hz, $f_3 - f_2 = 0.0065$ Hz, and $f_3 - f_1 = 0.012$ Hz. The signal generated by summing up all three STS2 sensors is shown at the lower right of the figure.

sensors are tilt motion.

If the horizontal sensors are considered tilt sensors, (as we discussed before, they are much more sensitive to tilt motion than horizontal motion at low frequencies), the Fourier transform of the sensors are shown in figure 6.14. The magnitudes of second order harmonics generated by the tilt horizontal coupling in these signals are less than 0.4 nrad. The noise level of the magnitudes of the harmonics is about 0.1 nrad in the frequency range of the second order harmonics.
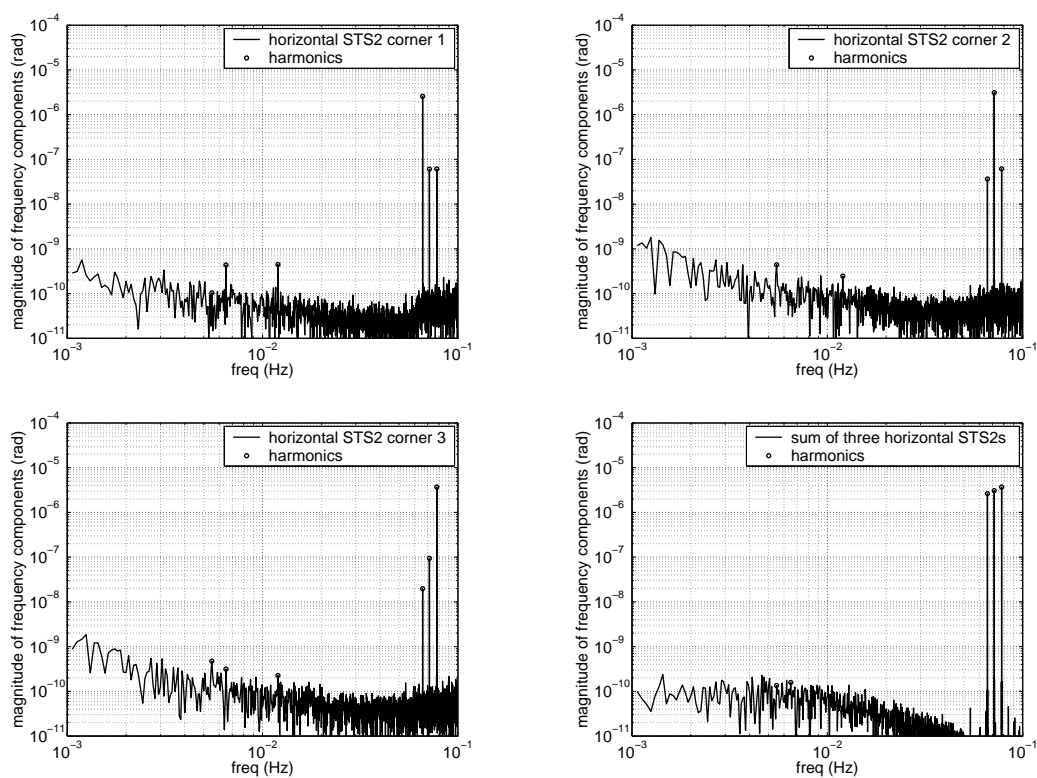
Figure 6.14: The output of the STS-2 sensors if they are considered as tilt sensors.

6.5.1   Reconstruction the Profile of the Position Sensor Target Plates

Denote the tilt motion measured by the three inertial sensors as T_1, T_2 and T_3. The second order tilt horizontal coupling can be represented by second order polynomial functions of the platform's horizontal motion measured by x_1, x_2, and x_3.

$$T_i = a_i x_1^2 + b_i x_2^2 + c_i x_3^2 + d_i x_1 x_2 + e_i x_2 x_3 + g_i x_3 x_1, \ a_i, \ b_i, \ c_i, \ d_i, \ e_i, \ g_i \in \Re. \quad (6.34)$$

The coefficients d_i, e_i and g_i can be obtained by comparing the magnitudes and phases of the second order harmonics of the tilt motion to the magnitudes and phases of the horizontal drive signals. For the signals shown in figure 6.14, we have

$$\begin{bmatrix} d_1 & d_2 & d_3 \\ e_1 & e_2 & e_3 \\ g_1 & g_2 & g_3 \end{bmatrix} = \begin{bmatrix} -0.0045 & 0.0182 & -0.0193 \\ -0.0192 & -0.0015 & 0.0139 \\ 0.0197 & -0.0108 & -0.0098 \end{bmatrix} \quad (6.35)$$

In each local coordinate, i, the height, H_i, of the target plate surface can be represented by a second order polynomial of x_i and y_i

$$H_i = m_i x_i^2 + n_i y_i^2 + k_i x_i y_i, \ m_i, \ n_i, \ k_i \in \Re. \quad (6.36)$$

Realize that

$$y_1 = \frac{1}{\sqrt{3}}(x_3 - x_2) \quad (6.37)$$

$$y_2 = \frac{1}{\sqrt{3}}(x_1 - x_3) \quad (6.38)$$

$$y_3 = \frac{1}{\sqrt{3}}(x_2 - x_1). \quad (6.39)$$

Hence,

$$H_1 = m_1 x_1^2 + \frac{1}{3} n_1 (x_3 - x_2)^2 + \frac{1}{\sqrt{3}} k_1 x_1 (x_3 - x_2) \tag{6.40}$$

$$H_2 = m_2 x_2^2 + \frac{1}{3} n_2 (x_1 - x_3)^2 + \frac{1}{\sqrt{3}} k_2 x_2 (x_1 - x_3) \tag{6.41}$$

$$H_3 = m_3 x_3^2 + \frac{1}{3} n_3 (x_2 - x_1)^2 + \frac{1}{\sqrt{3}} k_3 x_3 (x_2 - x_1) \tag{6.42}$$

The tilt motions can be obtained by:

$$
\begin{aligned}
T_1 &= \frac{1}{L}(H_3 - H_2) \\
T_2 &= \frac{1}{L}(H_1 - H_3) \\
T_3 &= \frac{1}{L}(H_2 - H_1)
\end{aligned}
\tag{6.43}
$$

where L is the distance between two vertical capacitive position sensors. n_i and k_i can be obtained by comparing equations 6.43 with the terms associated with d_i, e_i and g_i in equation 6.34:

$$
\begin{bmatrix} n_1 & k_1 \\ n_2 & k_2 \\ n_3 & k_3 \end{bmatrix} = \begin{bmatrix} 0.0043 & -0.0064 \\ 0.0150 & -0.0138 \\ 0.0146 & -0.0058 \end{bmatrix}
\tag{6.44}
$$

Note that there are 9 constraints and 6 variables and a least square fit is done to obtain the variables. With the Assumption $m_i = 0$, the heights of the target plates are shown in figure 6.15.

The coefficients m_i are not determined by this experiment. m_i can be determined by another experiment. For example, we can choose

$$x_1(t) = 150 \times 10^- 6 (sin(2\pi f_1 t) + sin(2\pi f_2 t)) \tag{6.45}$$

$$x_2(t) = 0; \tag{6.46}$$

$$x_3(t) = 0; \tag{6.47}$$
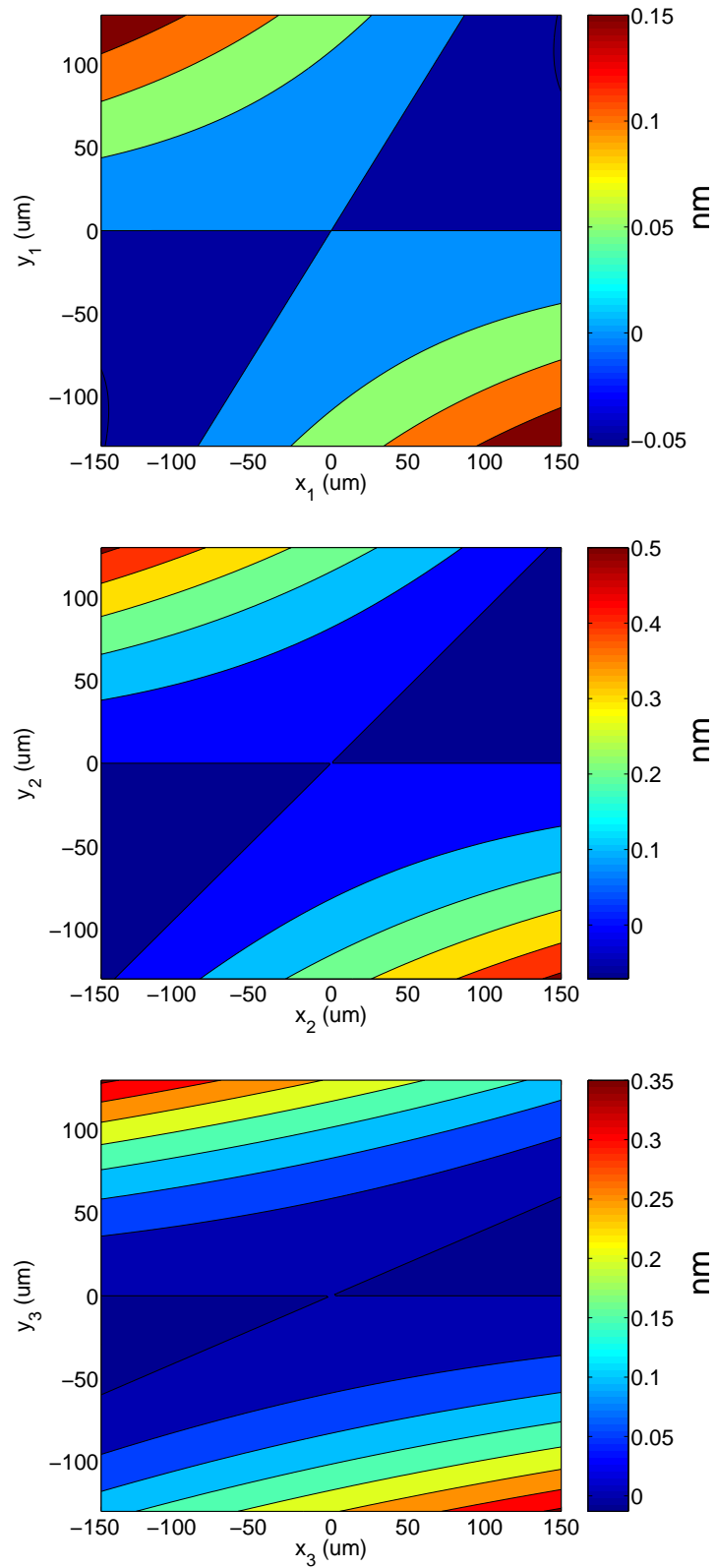
Figure 6.15: The contour map of the reconstructed position sensor target plates.

and measure m_1 by observing the magnitude and phase of the harmonic at frequency $f_2 - f_1$. In general, to measure other higher order coupling coefficients, the drive signals can be designed to make the desired harmonic to be in the sensitive band of the sensors, i.e. frequencies between 0.001 Hz and 0.1 Hz. Once those coefficients are obtained, the surfaces of the sensor target plates can be reconstructed. Because the inertial horizontal sensors are very sensitive to tilt at low frequencies as shown in figure 6.14, nanometer level accuracy can be expected by this method. The experiment to do the measurement is one of future works along this approach.

Chapter 7

Experiments and Results

7.1 Systems

Two double stage prototype vibration isolation systems were built based on the theories discussed in the previous chapters.

7.1.1 The Rapid Prototype

The first prototype was call the Rapid Prototype, which was a relatively simple system. There were two aims for this prototype. First, study the interaction between the two active stages and develop stable controllers for this 12 DOF system. Second, achieve vibration the isolation requirement of Advanced LIGO at 0.16 Hz, i.e. get an isolation factor of 10 and reach a noise level of 2×10^{-7} m/$\sqrt{\text{Hz}}$.

The two stages of the Rapid Prototype are shown in figure 7.1. Each stage is based on an equilateral triangle. Three cantilever springs are used to hang stage 1 from the support structure and three more are used to hang stage 2 from stage 1. The cantilever springs support the static load of the system.

Figure 7.1(b) shows the top view of stage 1. The stage has three-fold rotational symmetry. There are three different kinds of sensors used on this stage. ADE capacitive relative position sensors with dynamic range of ± 1 mm are used to measure the relative position between the support structure and stage 1. These sensors measure

the distance between the sensor head and an aluminum "target plate" by monitoring the capacitance between them. Two position sensors are used at each corner: one for vertical motion and one for horizontal motion. One Streckeisen STS-2 seismometer is used at each cornor. Each STS-2 sensor provides inertial information in three translational directions. The three horizontal STS-2 channels along the tangential directions are used as the feedback sensors. The three along the radius directions are used as horizontal witness senors. Each corner also has two Sercel L-4C geophones as high frequency horizontal and vertical inertial sensors. There are two BEI linear voice coils at each corner to provide the horizontal and vertical forces between the supporting structure and stage 1. The setup of stage 2 is identical to stage 1 with two exceptions: first, stage 2 does not have the STS-2 sensors; secondly, the dynamic range of ADE position sensors on the stage 2 is ± 0.25 mm, which offers higher sensitivity than those used on stage 1. While stage 1 is referenced to the support structure, stage 2 is referenced to stage 1.

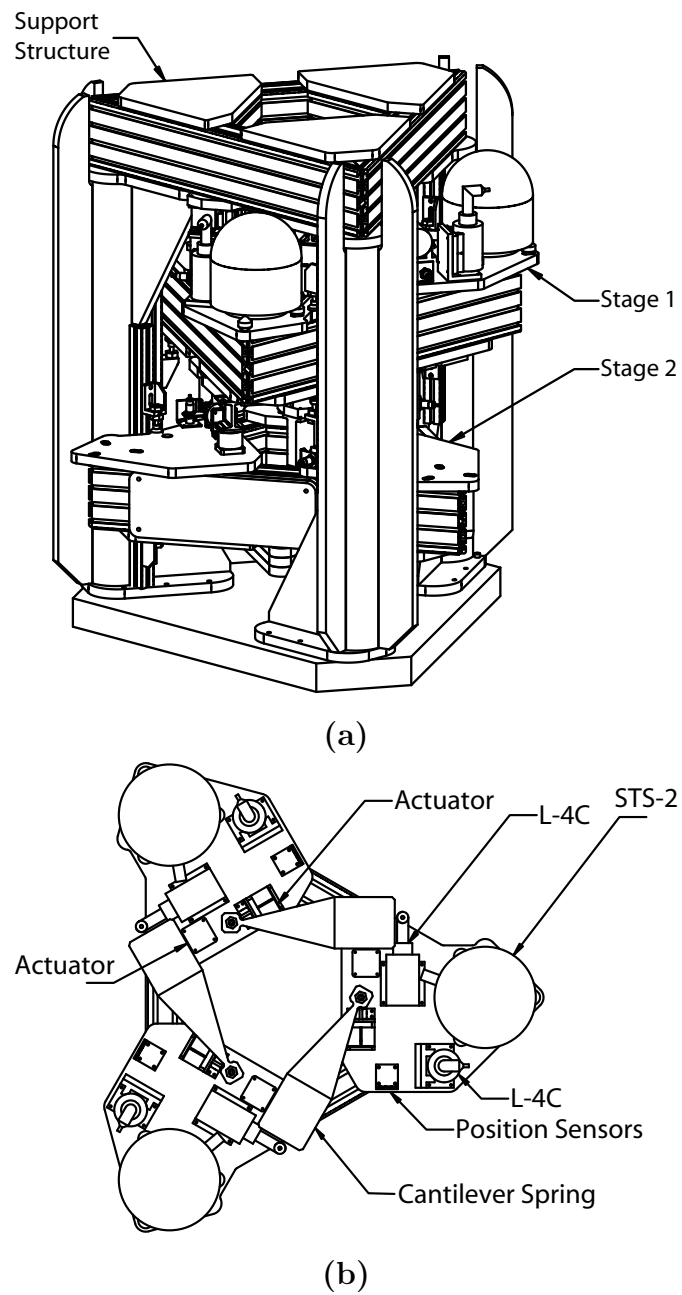Figure 7.1: The Rapid Prototype vibration isolation system. (a)The two stages and the support structure. (b) The top view of stage 1. For scale, the structure is 1.34 meter tall and the STS-2 sensors are 0.91 meter apart.
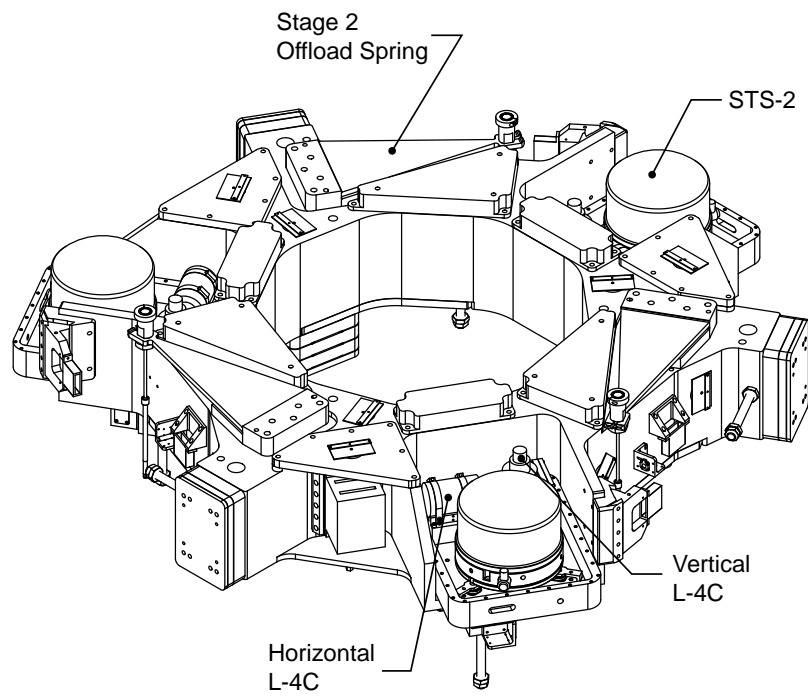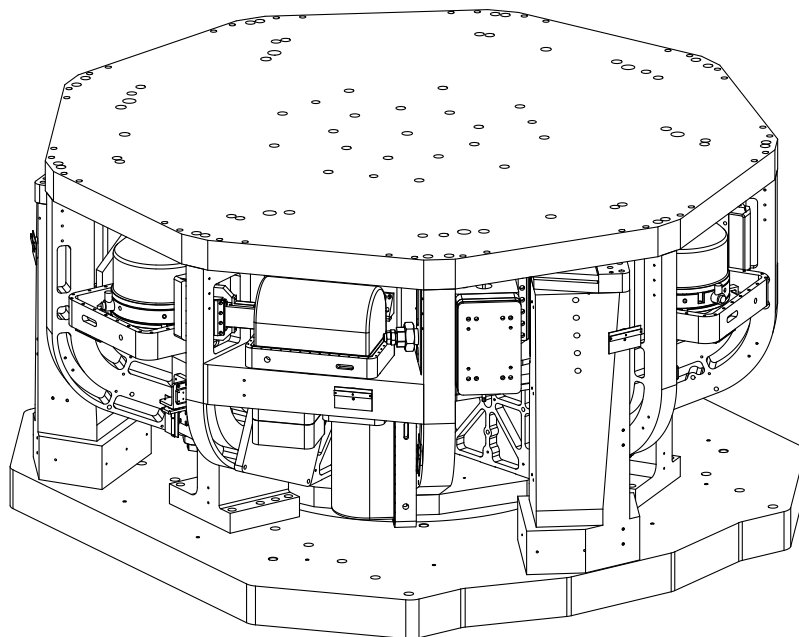
Figure 7.2: Stage 1 of the ETF Prototype.

Figure 7.3: The ETF Prototype. For scale, the structure is 0.83 meter tall and 1.78 meter in diameter.
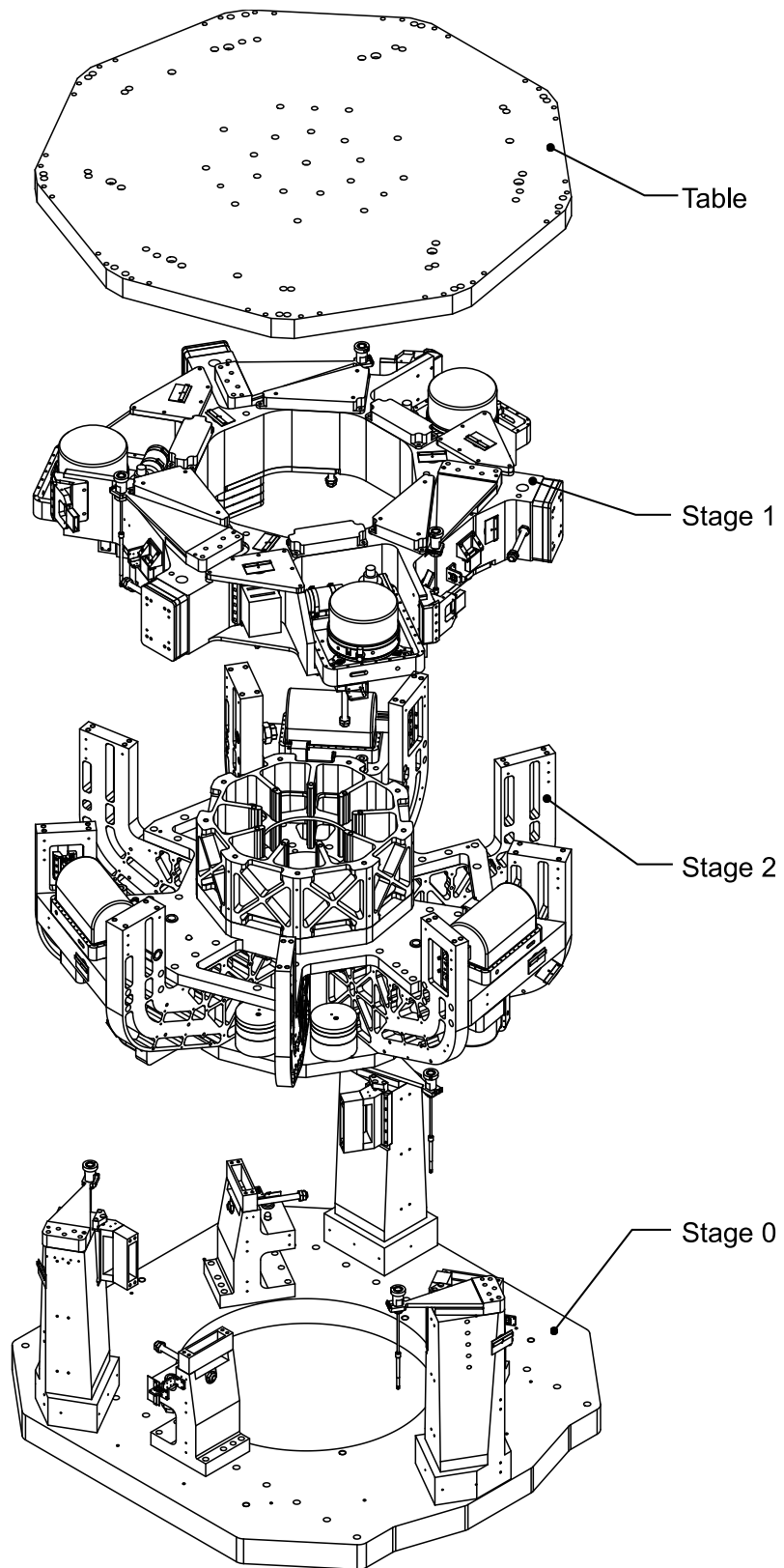
Table

Stage 1

Stage 2

Stage 0

Figure 7.4: The ETF Prototype disassembled. The two stages are nested together with the centers of mass aligned to save space and to reduce coupling between the stages.

7.1.2   The ETF Prototype

The second prototype was called the ETF Prototype. The aims of this prototype are: 1, meet the vibration isolation requirement at all frequencies; 2, make the size of prototype close the size of the actual system and provide a vibration isolated platform, i.e. an optical table, to support up to 600 kilograms of instrument payload, similar to the Advanced LIGO HAM payload. The BSC playload is 800 kilograms.

The topology of the ETF Prototype, as shown in figure 7.2, 7.3 and 7.4, is the same as the Rapid Prototype, but the mechanical structure of the ETF Prototype is more complicated. The two stages are nested together, which offers two benefits: first, it makes the whole system more compact; second, it allows the mass centers of the two stages to be close to each other to reduce coupling between the stages. The sensors are identical to those of the Rapid prototype except that Teledyne Geotech GS-13 seismometers are used for feedback and witness inertial sensors on stage 2 for their low noise levels in the frequency range between 1 Hz and 10 Hz.

7.2   Control

Similar control algorithms are used in both systems. The details of several techniques used to control the twelve DOF systems are discussed in this section.

7.2.1   Modular Control

The signals from the sensors are mapped to the mass center of the relevant stage to measure three translational and three rotational motions in Cartesian space. The control commands in each of these six normal directions are then mapped back to the commands of the individual actuators. SISO controllers are designed for each of these normal directions. There are several benefits with this modular control approach:

1. Because of the tilt-horizontal coupling problem, the vertical direction is fundamentally different from the horizontal directions. Hence, it is natural to separate them.

2. It helps to decouple the system. Because the stages are three fold rotationally symmetric, the coupling between the two normal horizontal directions is small, whereas the coupling between the 3 horizontal actuator directions is large.

3. Since the sensors and actuators all have finite size, they cannot be located at the same physical location, (as seen in figure 7.1, 7.2 and 7.4.). The geometric re-projection helps ensure that each set of sensors measures the same physical variable. This simplifies the design of sensor blending and sensor correction that will be discussed in the following sections.

7.2.2   Sensor Blending

As discussed in the previous section, multiple sensors are used to measure the stages' positions in each degree of freedom. Complementary filters are used to blend the signals from different sensors together and is called a super sensor. For example, figure 7.5 shows the sensor blending configuration and the feedback controller of stage 1 in one degree of freedom. First, complementary filter pair (H_2, L_2) (note that H_2 is the high pass filter and L_2 is low pass filter) is used to blend the two inertial sensors, i.e. the STS-2 seismometer and the L-4C seismometer together. Then, (H_1, L_1) is used to combine the position sensor and the inertial sensors. A key feature of this technique is that the position sensors are used as the dominate sensors at low frequencies. The reasons for this approach include:

1. Because the super-sensor has zero frequency sensitivity, the feedback control loop does not have a low frequency cross-over.

2. Position sensors do not have tilt-horizontal coupling, so the nonlinear tilt-horizontal coupling problem that the direct feedback systems suffer at very low frequencies can be avoided.
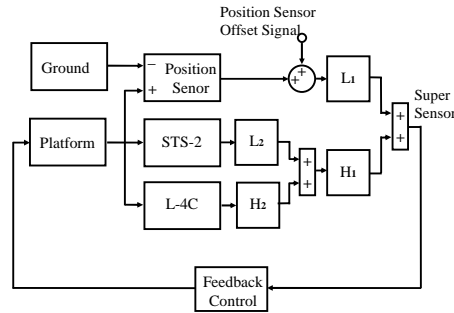
Figure 7.5: Block diagram of sensor blending and feedback control.

3. The position sensors provide alignment information and make alignment control possible;

4. This technique enables sensor correction in which the ground motion is measured externally and subtracted from the position sensors.

5. It linearizes the system at low frequencies.

7.2.3   Multi Layer Control

The control laws which were used for the system were relatively simple. The overall MIMO controller is constructed with a set of unconditionally stable SISO controllers which can be conceptually separated into several layers. The basic idea is to turn on these layers of SISO controllers sequentially. The existence of the early controllers and our experience with them have made the later controllers easier to design.

Damping Layer

The first layer of controllers are simple dampers. The velocity signals from the inertial sensors are fed back to the voice coil actuators to create electronic damping such that the Q of the vibrational modes is reduced. In the Rapid Prototype, the L-4C sensors are used on both stages. In the ETF Prototype, the L-4C sensors are used on stage 1 and the GS-13 sensors are used on stage 2. These dampers help to:

- Make the transfer functions smooth. Since the mechanical system itself does not provide much damping, the system's transfer functions vary dramatically in the frequency range where the systems's natural vibration modes are. To design a high gain unconditionally stable control loop directly on the original system, one has to invert the system's dynamics to smooth out the transfer function, which makes the controller non-robust. Hence, the dampers helps to make the next layer of high gain controllers easier to design.

- Reduce the cross coupling between different directions. In the original system without the dampers, the major cross coupling is caused by the coupled natural vibration modes. For example, consider a vibration mode that involves a little of horizontal motion but a lot of tilt motion. When the platform is driven horizontally at frequencies around the natural frequency of that mode, the vibration mode will be excited and thus a lot of tilt coupling is generated. Hence, by damping out the natural vibration modes of the system, cross coupling between different directions is significantly reduced.

It should be noted that because inertial sensors are used to provide the velocity signal for damping, the dampers do not add noise to the system other than the noise of the sensors. In contrast, if relative velocity between ground and the stages is used for damping, ground noise would be introduced to the system.

Feedback Layer

The second layer of controllers is a set of 12 SISO controllers on the 12 modular directions. The aim of this set of controllers is to achieve the isolation performance requirement. Hence, they must have high open loop gain and high cross over (unity gain) frequency. The controllers for the tilt directions are also responsible for low frequency tilt reduction. Hence, their loop gain at frequencies below 0.1 Hz should be very high, typically 10^3 to 10^4. Because the low frequency loop gain is very high, the controllers have to be turned on by increasing the gains gradually. Hence, they are designed to be unconditionally stable controllers such that they are kept stable during the turn on process. Successive loop closure is important for this system. The
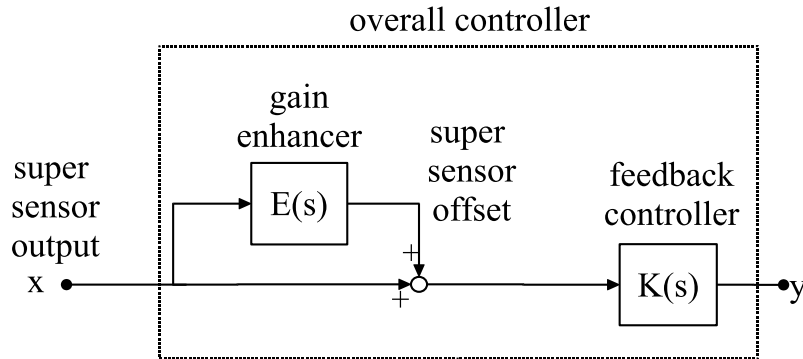
Figure 7.6: Gain enhancer. The overall loop gain is $|E(s) + 1|$ times larger than the original loop gain.

two tilt loops improve the horizontal plant - the high loop-gain and low-noise, linear displacement sensors dramatically reduce the tilt-horizontal coupling, the nonlinearity of the plant, and the tilt noise generated by the actuators. Hence, it is essential that those loops be closed before the horizontal translation loops are closed.

The major challenge of the feedback controller design is to obtain a high cross over frequency. For example, at 10 Hz, the vibration isolation requirement is to obtain an isolation factor if 2000. In the vertical direction the mechanical passive isolation of the system provides a factor of 10 isolation, which implies that the open loop gains of the two vertical controllers should be more than 14 in order that a total factor of 200 active isolation can be achieved. However, the mass stages of the ETF Prototype have resonant frequencies starting from about 120 Hz. Even with aggressive notch filters, we can only make the cross over frequency of the controllers about 40 Hz. Consequentially, the open loop gain of the controllers at 10 Hz is about 5 to 7.

Gain Enhance Layer

To increase the gain of the controllers, a set of gain enhancement loops could be added as shown in figure 7.6. As a result, the overall open loop gain is $|E(s) + 1|$ times larger.

The gain enhancer can be designed by considering the super sensor offset as the virtual actuator. The overall controller including the gain enhancer and the original

feedback controller is not unconditionally stable. However, through this layered design approach it is separated into two unconditionally stable controllers. The problem with this approach is that typically the original feedback controller magnifies the magnitudes of the resonant vibration modes, thus more aggressive notch filters are needed in the gain enhancer.

7.2.4   Control Procedure

As a summary, the whole system should be controlled in the following steps.

1. Design and turn on all of the 12 dampers.

2. With the blending frequency between the position sensors and the inertial sensors at 2 Hz, design and turn on the 12 feedback controllers. At each step of the sequence, turn on the tilt controllers before the horizontal controllers.

3. Measure the transfer function from the position sensor signal to the horizontal inertial sensor output. Align the coordinate defined by the position sensors to the coordinate defined by the gravity field using the method discussed in section 4.3.4 in chapter 4.

4. Check the nonlinear tilt horizontal coupling and make sure that the nonlinearity of the system is small.

5. Determine sensor correction gain if sensor correction is going to be used

6. Lower the blending frequencies between the inertial sensors and position sensors such that desired vibration isolation can be achieved.

7. If it is necessary, design and turn on the gain enhancers.

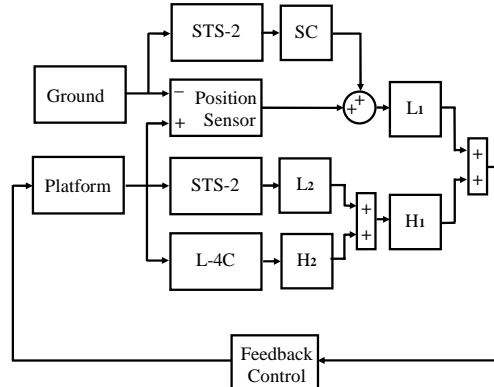8. Turn on sensor correction if it is used.

Figure 7.7: Block diagram of the whole control system of stage 1 of the Rapid Prototype. The block 'SC' stands for the sensor correction filter. The sensor correction signal drives the position sensor offset input shown in figure 7.5.

7.3   Results

7.3.1   Vibration Isolation by Sensor Correction on the Rapid Prototype

In our experiment, the blending frequency between the position sensors and the inertial sensors is at 0.3 Hz in the horizontal directions and 0.07 Hz in the vertical direction. Hence, there is no vibration isolation from the feedback loop below those frequencies. Instead, low frequency vibration isolation is achieved by sensor correction. The diagram of sensor correction is shown in figure 7.7.

The transfer function of the horizontal sensor correction filter is shown in figure 7.8. It reduces the tilt noise with a magnitude proportional to frequency's third power below 0.04 Hz and has a gain match error less than 0.04 in frequencies above 0.1 Hz. In the vertical direction, because there is much less tilt noise, a less aggressive sensor correction filter is used, as shown in figure 7.9.

The performance of our vibration isolation system is shown in figure 7.10, 7.11 and 7.12. The figure compares the ground motion measured by the STS-2 sensors on the ground with the platform motion measured by STS-2 sensors on stage 1. One might
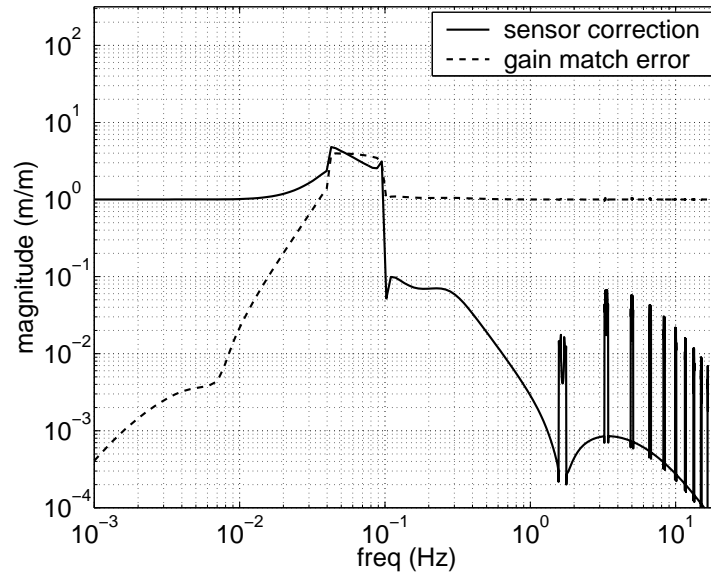
Figure 7.8: Transfer function of the optimal polyphase FIR filter as the horizontal sensor correction filter for the Rapid Prototype.

worry that the same STS-2 sensors are used both as feedback sensors and witness sensors. Actually, this is not a problem in this measurement for two reasons: first, the noise level of the STS-2 sensors are lower than the isolated platform motion in the experiment and second, the horizontal STS-2 sensors are not used as feedback sensors below 0.3 Hz. Broadband isolation above 0.1 Hz is achieved in three directions simultaneously. Particularly, the isolation factors are at least 10 at 0.15 Hz and the vibration level of 2×10^{-7} m/$\sqrt{\text{Hz}}$ is achieved in all directions. This result meets the isolation requirements for Advanced LIGO at low frequencies. In the horizontal directions, the vibration is magnified by three times between 40 mHz and 100 mHz, which is a result of the overshoot of the sensor correction filter shown in figure 7.8. In the vertical direction, the sensor correction filter does not have as much overshoot, so there is less noise-magnification at low frequencies.
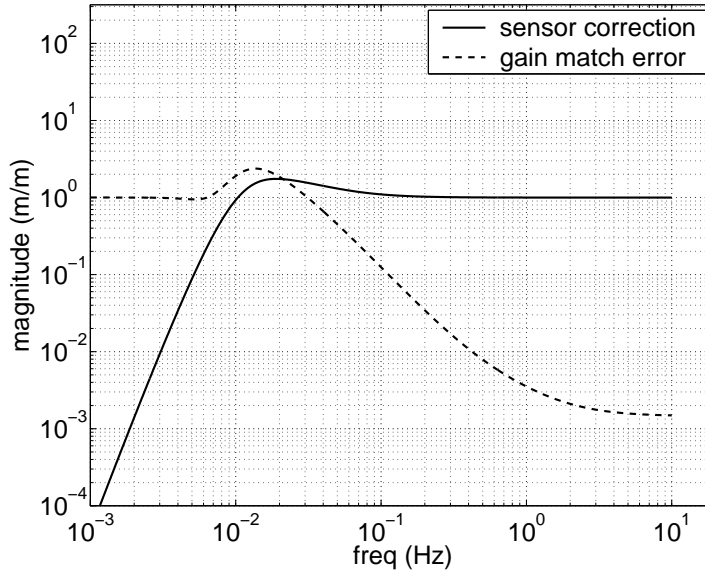
Figure 7.9: Transfer function of the vertical sensor correction filter for the Rapid Prototype.

7.3.2   Vibration Isolation by Feedback Only on the ETF Prototype

The sensor correction technique shown in previous section demonstrated good performance at 0.16 Hz. However, because practically it is very difficult to match the gain of the inertial sensor and the position sensor on the platform with an error less than 5%. So, even if there is no additional gain match error from the sensor correction filters, it is very difficult to achieve an isolation factor more than 20 just by sensor correction. At 1 Hz, we would like to have an isolation factor of 1000. It is obvious that a significant part of the isolation has to come from feedback.

From the previous chapters, we learned that we have to address the same fundamental trade-off between the low frequency tilt noise reduction performance and the high frequency isolation performance. Either sensor correction or feedback or any combination of them is used. The convex optimization complementary filter design tool is used to study this trade-off. It is learned that the trade-off is quite tight: to increase the vibration isolation by a factor of 1000 at 1 Hz must be at the cost of
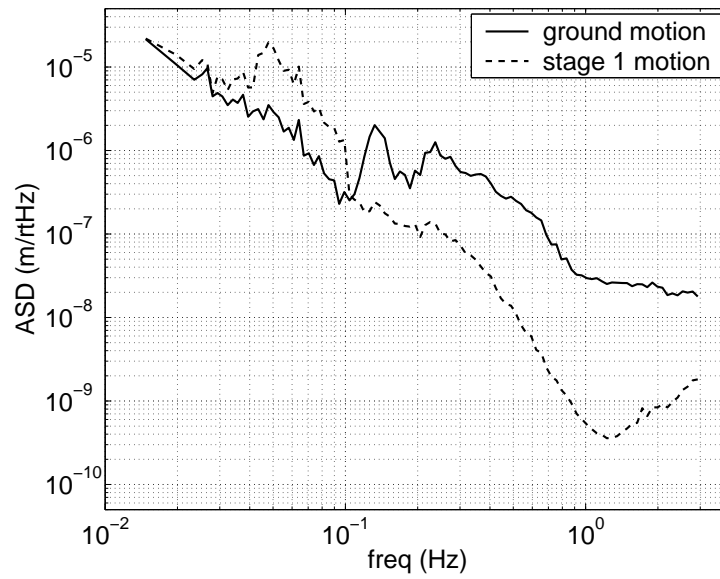
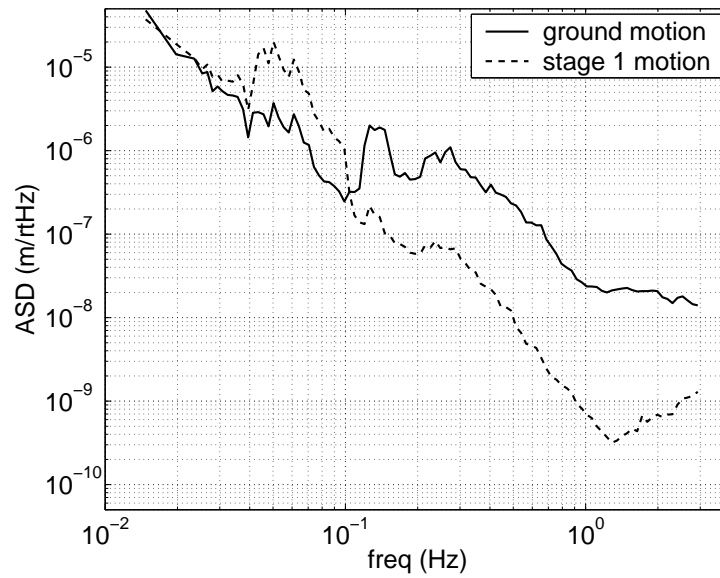Figure 7.10: Low frequency isolation performance in horizontal x direction.

Figure 7.11: Low frequency isolation performance in horizontal y direction.
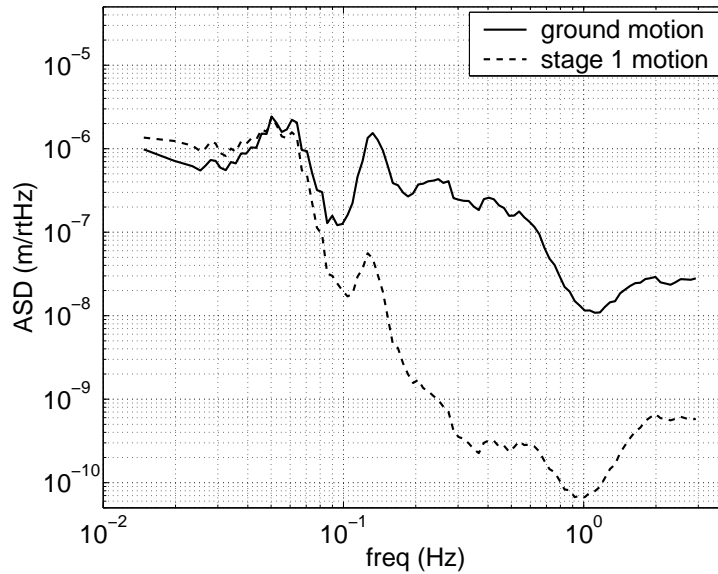
Figure 7.12: Low frequency isolation performance in vertical z direction.

adding a significant amount of tilt noise below 0.12 Hz. On the other hand, it is also learned that the vibration isolation performance at 10 Hz does not have much to do with tilt noise reduction performance at low frequencies.

The transfer functions of the polyphase FIR complementary filters used for sensor blending on stage 1 is shown in figure 7.13. Compared to the filters used for sensor correction in figure 7.8, over shoot at low frequencies is higher and wider. If the loop gain is enough, this pair of filters could offer a factor of 7000 isolation at 1 Hz. It is higher than the 1000 requirement because we would like to have other noise sources dominate so they can be easily identified. Once the other noise sources are eliminated, we could design a pair of filters that is less aggressive at 1 Hz and reduce the overshoot at low frequencies.

The performance of the ETF platform is shown in figure 7.14, 7.15 and 7.16.

1. At 0.16 Hz, we obtained an isolation factor of 5 and kept the noise levels to be less than 2×10^{-7} m/$\sqrt{\text{Hz}}$ on both stages in all three DOF.

2. At 1 Hz, the noise levels of the second stage seen by the witness sensors are about 2×10^{-10} m/$\sqrt{\text{Hz}}$ in all 3 DOF, which is believed to be limited by the
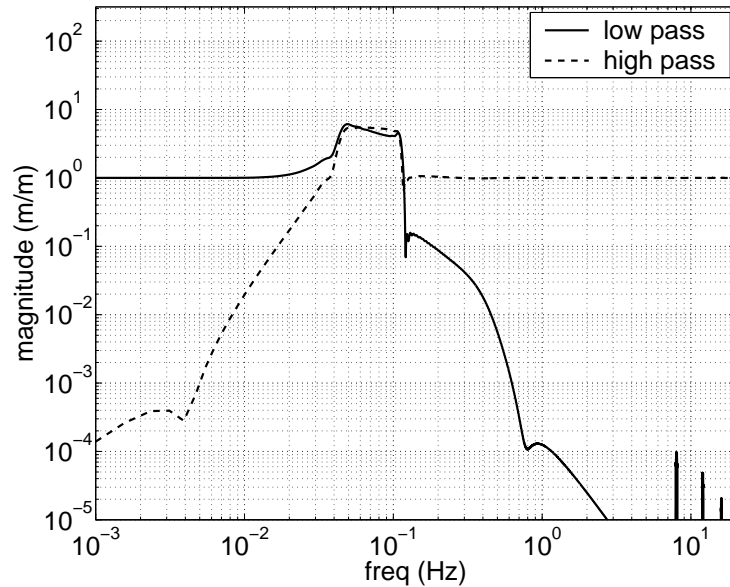
Figure 7.13: ployphase FIR complementary filters used for sensor blending on stage 1 of the ETF platform.

GS-13 sensor noise. The noise levels of the stage 2 feedback GS-13 sensors are about 10^{-11} m/$\sqrt{\text{Hz}}$ which is 1000 times lower than the ground motion. This implies that there is enough loop gain in the controllers and that the polyphase FIR filters behave very well in the feedback system.

3. At 10 Hz, in the horizontal direction, the feedback GS-13 sensors indicate a motion of 10^{-12} m/$\sqrt{\text{Hz}}$ which is about 1000 times lower than that of the ground. The sensor noise of the GS-13 is about 4×10^{-13} m/$\sqrt{\text{Hz}}$ at 10 Hz as shown in chapter 5. Hence we think the GS-13 output is a good measurement of the platform motion. In the vertical direction, the platform motion seen by the witness GS-13 is about 2×10^{-11} m/$\sqrt{\text{Hz}}$ and the isolation factor is about 150. Since the natural vibration frequencies for the vertical modes are higher than that of the horizontal modes, the passive isolation is less in the vertical direction, which explains the relatively poorer performance in the vertical direction.

Figure 7.14: ETF performance by feedback only: horizontal x direction
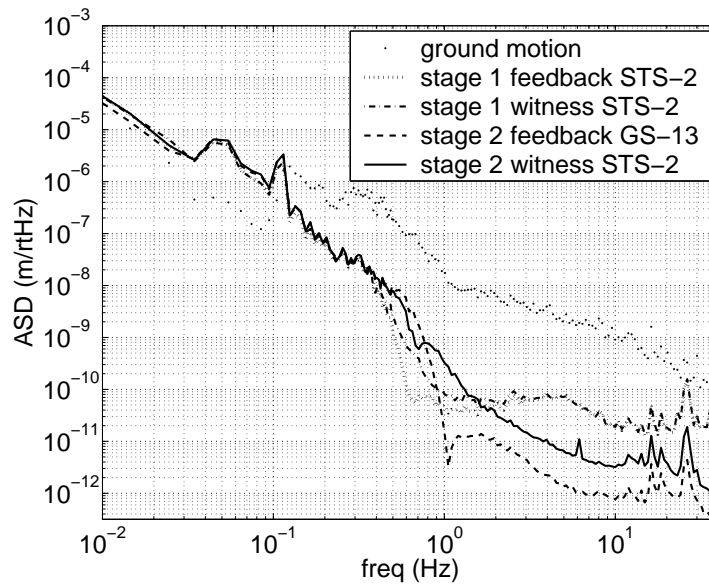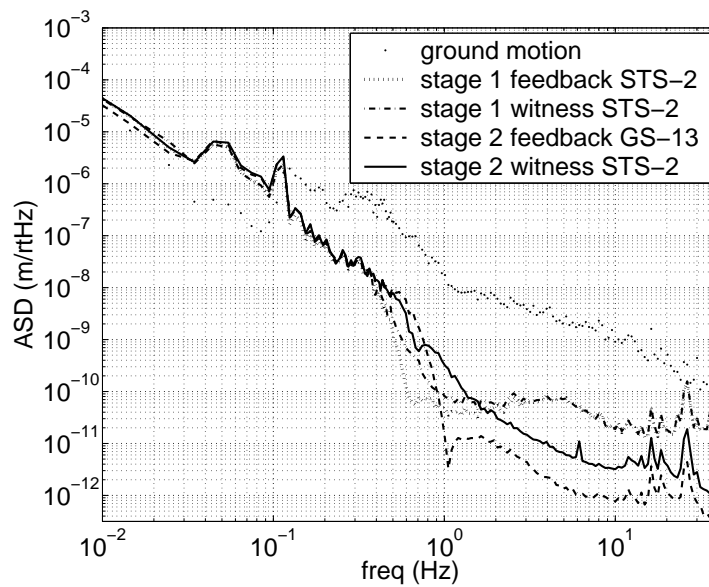

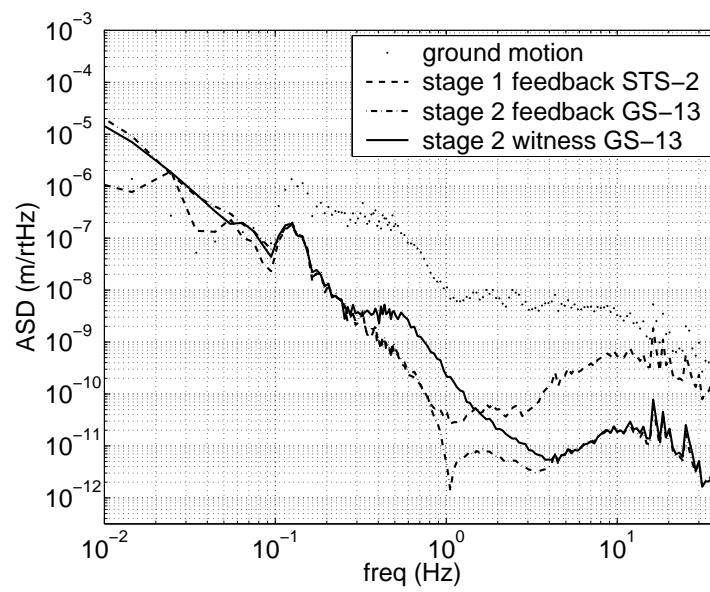Figure 7.15: ETF performance by feedback only: horizontal y direction

Figure 7.16: ETF performance by feedback only: horizontal z direction

Chapter 8

Summary and Conclusions

The purpose of the work described in this thesis is to investigate the active low frequency seismic vibration isolation and alignment system for Advanced LIGO. The system that we proposed is fairly complicated: it has 12 degrees of freedom, 12 actuators and more than 30 sensors. However, we demonstrated that it can be controlled by a set of relatively simple unconditionally stable SISO controllers to nearly satisfy the performance requirement of Advanced LIGO.

The tilt-horizontal coupling problem is of one the most challenging problems for a low frequency vibration isolation system below 1 Hz. If not properly addressed, it could cause the system to be unstable and/or add a tremendous amount of noise to the system.

In this work, the tilt-horizontal coupling problem is attacked by two means. First, feedback tilt controllers with very high loop gains at low frequencies are used to reduce both the linear and the nonlinear tilt-horizontal coupling caused by the mechanical system. With these controllers running, the remaining tilt-horizontal coupling is dominantly caused by the position sensors, which can be calibrated by the linear and nonlinear MIMO analysis tools developed in this work. Secondly, FIR complementary filters are used to reduce the noise caused by tilt-horizontal coupling at low frequencies. The global optimal FIR complementary filters can be designed very efficiently using convex optimization. We have developed a computationally efficient polyphase FIR filter structure which makes high order FIR complementary filters practical.

157

Since there are more than one sensor for each degree of freedom on the ETF Prototype, the very complexity of the system can be used to calibrate the relative gains between different sensors and to measure the noise levels of them, which offers essential information for sensor blending filter design and for system performance analysis.

We have successfully demonstrated the concepts necessary to make the Advanced LIGO Vibration Isolation and Alignment System a practical system. We have achieved the required performance below 1 Hz, and nearly achieved necessary performance above 1 Hz. The work on the ETF prototype makes clear the modification necessary for the Advanced LIGO system.

Chapter 9

Future Work: Global Control

9.1 Introduction

In previous chapters, signals only from the local sensors were used to control the vibration isolation systems. In this chapter we are going to study the possibility of using the signals from the gravitational wave detection interferometer for better isolation performance. It is called the global control since it involves multiple individual vibration isolation systems. The basic motivations for doing this includes:

1. The interferometer is much more sensitive than any of the sensors used in the vibration isolation system.

2. The interferometer measures relative positions and it does not have the tilt horizontal coupling problem.

3. The ultimate goal of the vibration isolation is to make the interferometer work properly. Hence, if the vibration of the whole system in some direction impacts the interferometer performance, it implies that the interferometer works as a sensor for the vibration of the system in that direction (for the frequencies below the observation band). On the other hand, if the interferometer is not sensitive to the vibration of the system in some direction, the vibration isolation performance in that direction is not important. Hence, although the interferometer

does not provide information in all the degrees of freedom of the whole system, in principle, it provides the information in the directions that are important.

9.2   The signal from the Interferometer

The LIGO interferometer generates many signals as functions of the positions of the mirrors. To make use of these signals, the whole vibration isolation system, involving many individual local isolation systems, has to be studied together. For simplicity, we will study a single interferometric cavity with two vibration isolation systems as shown in figure 9.1. The interferometer measures the changing in distance between the two mirrors. The block diagram of the signal flow is shown in figure 9.2. The output of the interferometer is not only a function of the difference of the positions of the mirrors, but also a function of the incoming gravitational wave:

$$C(s) = w(s) + m_a(s) - m_b(s) = w(s) + x_{2a}(s)P_a(s) - x_{2b}(s)P_b(s), \qquad (9.1)$$

where $w(s)$ is the displacement generated by the gravitational wave, x_{2a} and x_{2b} are the positions of the second stages of the two active isolation system in horizontal direction, P_a and P_b are the transfer functions of the two passive isolation systems. Note that this is an over simplified model. For example, the motion of the platforms in other directions are not considered. To consider the contributions from the platform motion in all degrees of freedom is an important part of future work.

The transfer function of the passive vibration isolation system proposed for Advanced LIGO [40] is included in figure 9.3.

9.3   Global Control

The controller using the interferometer signal is shown in figure 9.4. The interferometer can be used in frequency below the gravitational wave observation band starting at 10 Hz.

The global interferometer signal and the local inertial sensor signal are blended
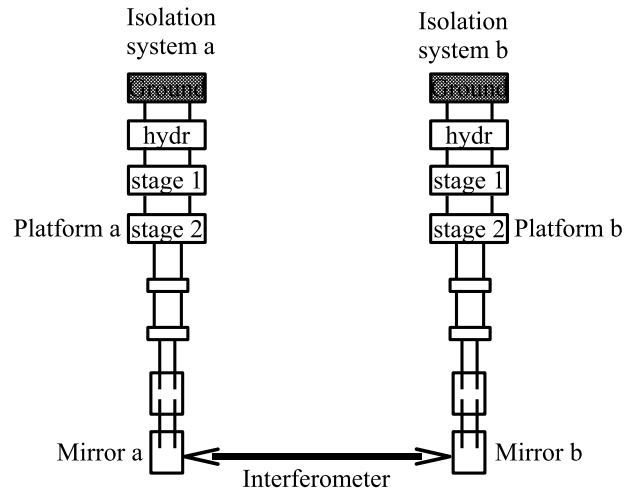
Figure 9.1: A interferometric cavity, 4 km long.
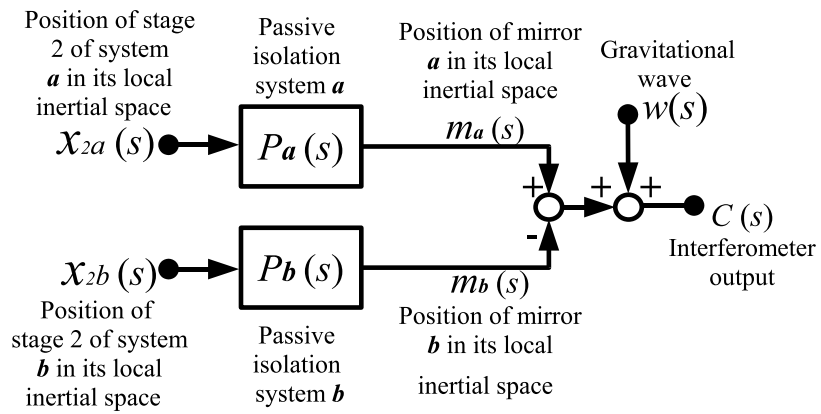
Figure 9.2: The block diagram of the signals in a interferometric cavity.
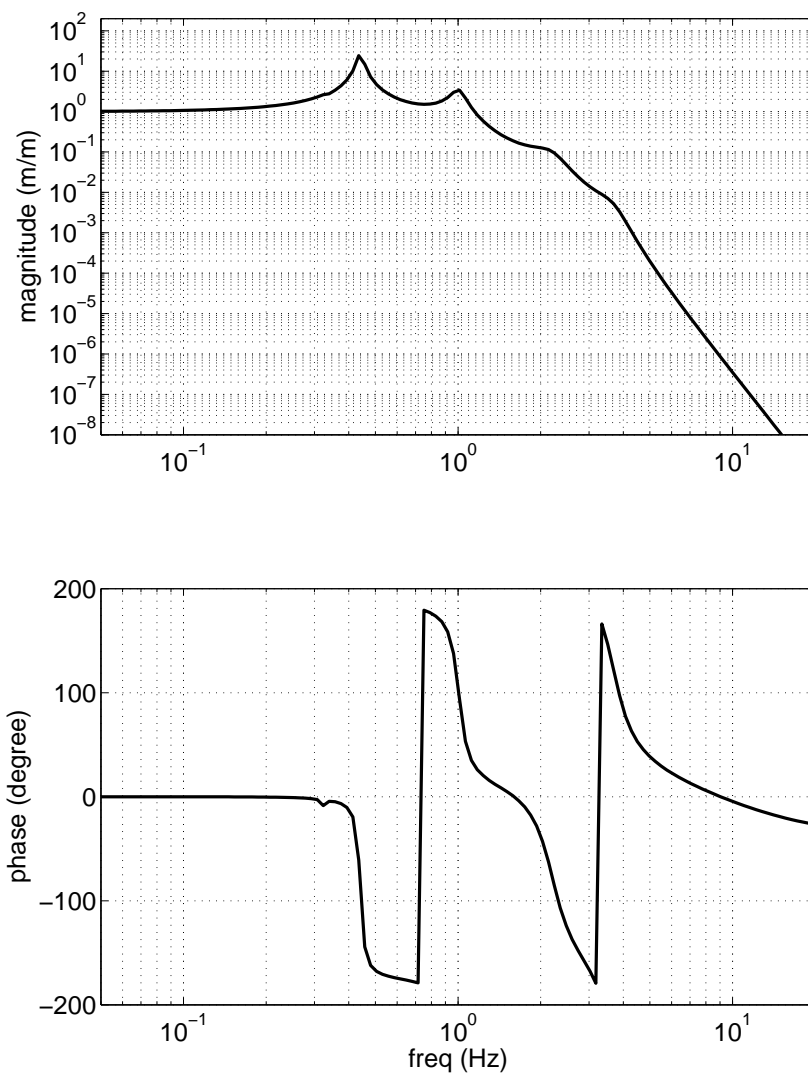
Figure 9.3: The transfer function of the passive vibration isolation system proposed for Advanced LIGO.
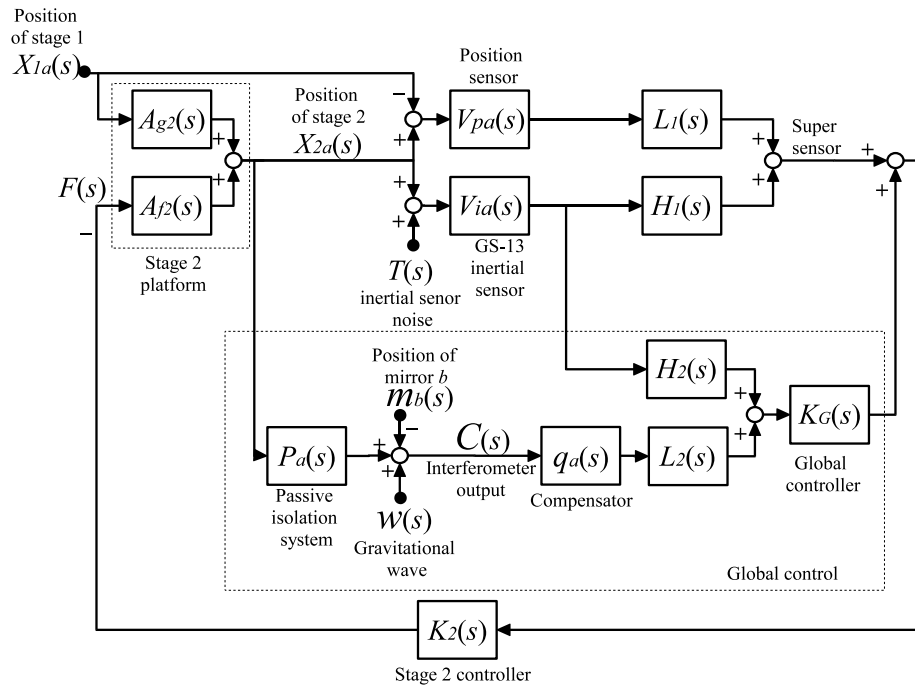
Figure 9.4: The global controller using the interferometer signal. (H_1, L_1) and (H_2, L_2) are two complementary filter pairs. The transfer functions of the position sensor and the inertial sensor are assumed to be 1, i.e. $V_i = 1$ and $V_p = 1$.

together and fed back to the super sensor offset of the original controller on stage 2 of isolation system a. The transfer function of the passive isolation system, P_a is compensated by q_a. If the compensation is perfect, we would have $P_a q_a = 1$. Practically, we could just compensate the first two resonant frequencies for the sake of robustness. Let E_c denote the error of compensation

$$E_c = 1 - P_a q_a. \tag{9.2}$$

The transfer function of the global super sensor is given by

$$V_{sG} = P_a q_a L_2 + H_2 = 1 - E_c L_2. \tag{9.3}$$

If we have

$$|E_c L_2| < 1 \tag{9.4}$$

the phase error of V_{sG} will be less than 90 degrees and thus the global controller can be kept stable with enough gain around the blending frequencies. Since the transfer function of the passive vibration isolation system is very well studied and can be easily calibrated online, the requirement of equation 9.4 should be easily satisfied. The compensation of the passive system and its error is shown in figure 9.5. At the first resonant frequency about 0.45 Hz, the frequency of zeros of the compensator is intensively misaligned by about 2% and the damping ratio is set to be about 50% less. As a result the compensation error E_c has a peak with magnitude of about 1 at 0.45 Hz. In practice, the compensator could be easily more accurate than this. The complementary filter pair H_2 and L_2 are shown in 9.6. The transfer function of the super sensor of the global control is shown in figure 9.7. The ripples of the super sensor transfer function comes from the error of the compensation.

The cross over frequency of the global controller is about the same as the original stage 2 controller, which is at about 40 Hz. Hence, its loop gain below 1 Hz should be quite high (higher than 100 at 1 Hz and 1000 below 0.1 Hz).
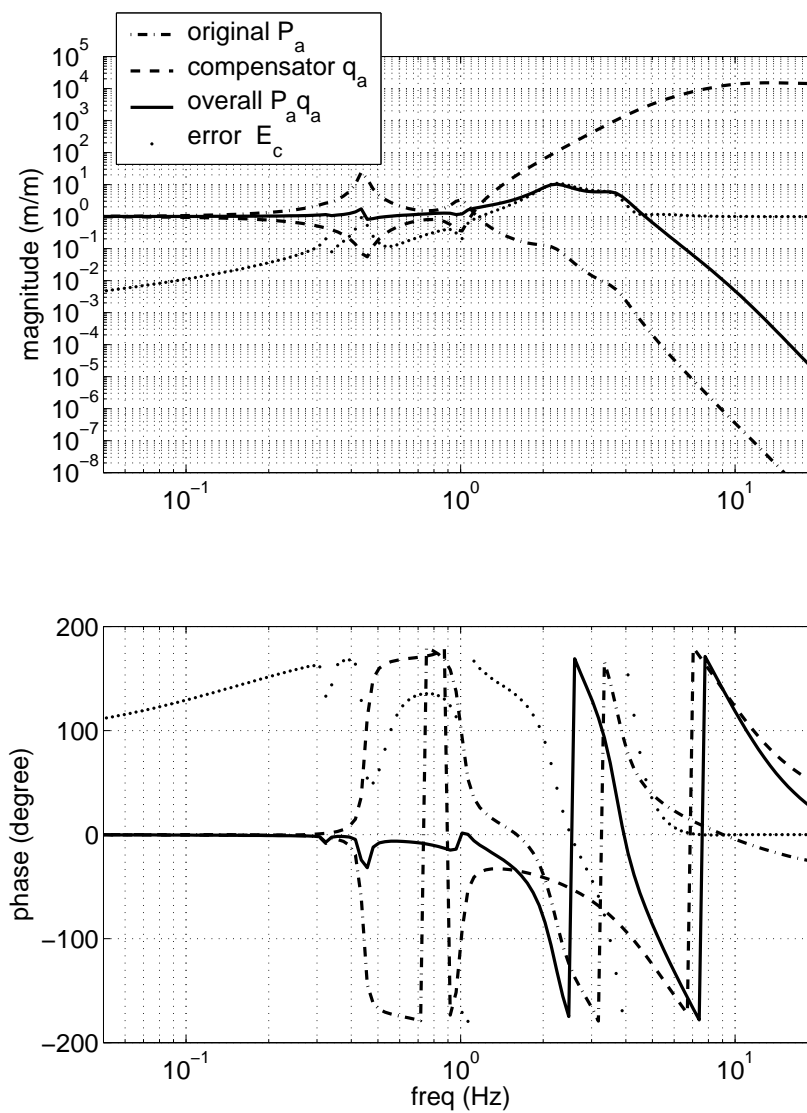
Figure 9.5: The transfer function of the passive isolation system (the quadruple pendulum) and its compensation. [40]
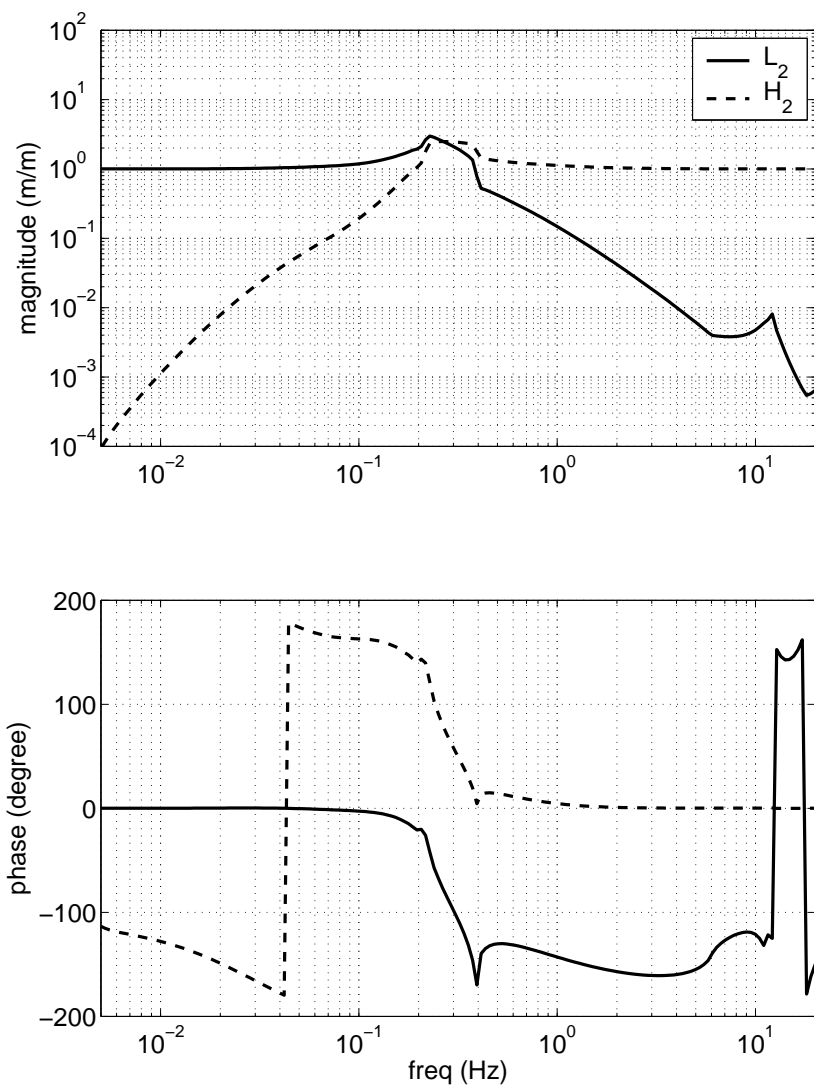
Figure 9.6: The complementary filter pair for sensor blending in global control.
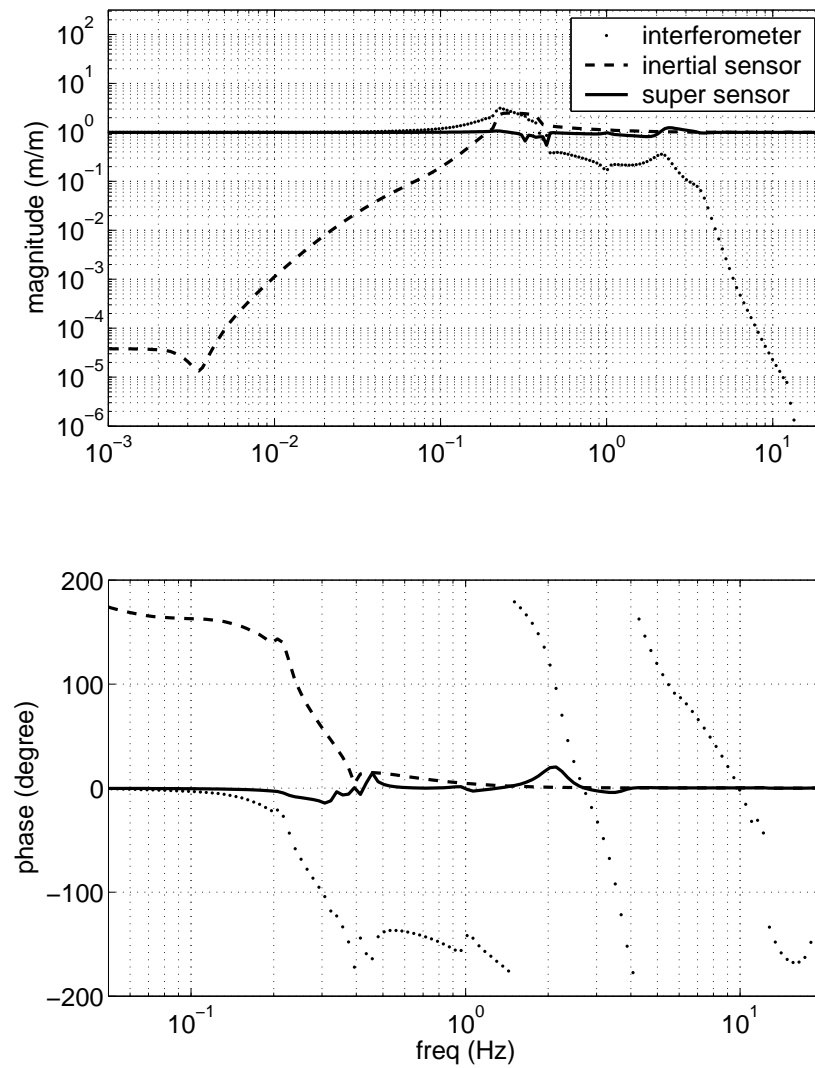
Figure 9.7: The transfer function of the super sensor and its decomposition.

The motion of stage 2 of the isolation system a is given by

$$
\begin{aligned}
X_{2a} =& \frac{L_1 K_2 A_{f2} + A_g}{1 + G_L} X_{1a} \\
&+ \frac{(q_a L_2 K_G) K_2 A_{f2}}{1 + G_L} m_b \\
&+ \frac{-(q_a L_2 K_G) K_2 A_{f2}}{1 + G_L} w \\
&+ \frac{-(H_1 + H_2 K_G) K_2 A_{f2}}{1 + G_L} T
\end{aligned}
\tag{9.5}
$$

where G_L denotes the open loop gain of the whole control system:

$$
G_L = ((H_2 + P_a q_a L_2) K_G + 1) K_2 A_{f2}.
\tag{9.6}
$$

Also, denote G_2 as the open loop gain of the stage 2 without the global control and G_G as the open loop gain of the global control,

$$
\begin{aligned}
G_2 =& K_2 A_{f2} \tag{9.7} \\
G_G =& (H_2 + P_a q_a L_2) K_G \tag{9.8} \\
G_L =& (G_G + 1) G_2. \tag{9.9}
\end{aligned}
$$

The contribution of the stage 1 motion to the stage 2 motion is

$$
\frac{L_1 K_2 A_{f2} + A_g}{1 + G_L} X_{1a}.
\tag{9.10}
$$

When $G_L \gg 1$, it becomes

$$
\frac{L_1 K_2 A_{f2} + A_g}{G_L} X_{1a} = \frac{1}{1 + G_G} \frac{L_1 K_2 A_{f2} + A_g}{G_L} X_{1a}.
\tag{9.11}
$$

So, with the global control the vibration noise from the ground of system a will be further reduced by $1 + G_G$ (larger than 100 below 1 Hz). When $G_L \gg 1$ and $G_G \gg 1$,

the contribution from the position of the mirror b is

$$\frac{(q_a L_2 K_G) K_2 A_{f2}}{1 + G_L} m_b \approx L_2 q_a m_b. \tag{9.12}$$

Since $q_a m_b$ is approximately the motion of stage 2 of system b, equation 9.12 shows that the global control will force stage 2 of system a to follow the motion of stage 2 of system b at low frequencies as we expected. Similarly, the contribution from the gravitational wave signal w is,

$$\frac{(q_a L_2 K_G) K_2 A_{f2}}{1 + G_L} w \approx L_2 q_a w, \tag{9.13}$$

which implies that the platform motion will be "sensitive" to gravitational waves at low frequencies. The noise of the horizontal inertial sensor T is a combination of the instrumental noise and the tilt noise. When the $G_L \gg 1$, the contribution from T to X_{a2} is

$$\frac{-(H_1 + H_2 K_G) K_2 A_{f2}}{1 + G_L} T \approx \frac{-H_1}{1 + G_G} T - H_2 T. \tag{9.14}$$

The $-H_1 T$ is the contribution of the noise of the horizontal sensor to the stage 2 motion without the global control, which is attenuated by $(1 + G_G)$ times by the global controller. Hence, the dominant contribution from the noise of the inertial sensor is $-H_2 T$. Since the magnitude of H_2 is about 20 time lower than H_1 at low frequencies, the contribution from inertial sensor noise, mostly tilt noise at low frequencies, is much reduced.

The output of the interferometer is

$$
\begin{aligned}
C =& P_a X_{2a} - m_b + w \\
=& \frac{(L_1 K_2 A_{f2} + A_g) P_a}{1 + G_L} X_{1a} \\
& + (\frac{P_a q_a L_2 K_G K_2 A_{f2}}{1 + G_L} - 1) m_b \\
& + (\frac{-(q_a + L_2 K_G) K_2 A_{f2}}{1 + G_L} + 1) w \\
& + \frac{-(H_1 + H_2 K_G) K_2 A_{f2} P_a}{1 + G_L} T
\end{aligned}
\tag{9.15}
$$

The contribution from the mirror of isolation system b to the interferometer output is:

$$
\begin{aligned}
& (\frac{P_a q_a L_2 K_G K_2 A_{f2}}{1 + G_L} - 1) m_b \\
=& - \frac{H_2 K_G K_2 A_{f2}}{1 + G_L} m_b - \frac{1}{1 + G_L} m_b \\
\approx& - \frac{H_2}{H_2 + L_2 P_a q_a} m_b \\
\approx& - H_2 m_b,
\end{aligned}
\tag{9.16}
$$

where the first approximations assumes $|G_L| \gg 1$, and the second approximation assumes $H_2 + L_2 P_a q_a = 1$. Similarly the contribution from the gravitational wave is approximately $H_2 w$ when the loop gains are high. Since H_2 is very close to 1 above 10 Hz, the interferometer is still sensitive to gravitational waves in the Advanced LIGO's sensitive band. When the loop gains are high,

$$
C \approx (\frac{L_1}{G_G} + A_g) P_a X_{1a} - H_2 P_a T - H_2 m_b + H_2 w.
\tag{9.17}
$$

The term $H_2 m_b = H_2 P_b X_{2b}$ will dominate the noise of C. Comparing the case when there is no global control, contribution from X_{2b} is attenuated by H_2.

One could further reduce the noise by means of sensor correction as shown in figure 9.8. Then the contribution from the motion of stage 2 of isolation system b
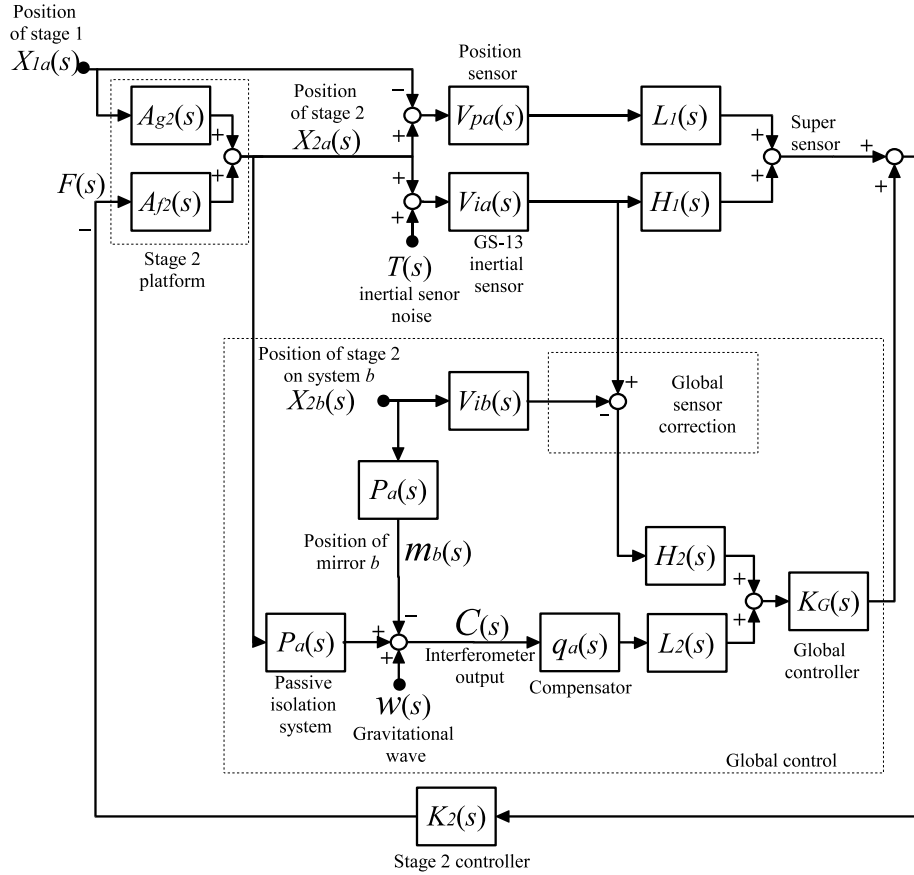
Figure 9.8: The global controller using sensor correction.

will become $H_2(P_b - P_a)X_{2b}$. Since we design $P_b \approx P_a$ and thus $|P_b - P_a| < |P_b|$, the noise can be reduced.

9.4 Discussion

The advantage of this sensor blending global control approach are the follows:

1. It allows a relatively high cross over frequency. Because the interferometer signal is not used at high frequencies, the controlled band can extend to Advanced LIGO's observe band.

2. It enables sensor correction as shown in figure 9.8.

3. It is an add-on loop to the local control loop. Hence, it enables us to turn on the local control to lock the interferometer first and then turn on the global control using the interferometer signal.

For the simplicity of this discussion, we ignored the transfer functions from the motion of the platforms in other directions to the interferometer output. For example, vertical motion of the mirrors in their local inertial space will change the length of interferometer cavity, because the vertical directions in the two inertial space are not exactly parallel due to curvature of the round earth. Noise caused by the motion of the platforms in directions other than horizontal directions can be reduced by means of sensor correction or general feed forward similar to the sensor correction approach shown in figure 9.8.

The basic idea of the global control can be generalized to higher stages (stage 1 and the hydraulic system) of the isolation systems. It can also be generalized to other degrees of freedoms of the interferometer. The global control concept also offers us the opportunity to optimize the design of the whole vibration isolation system together. For example, the design of the complementary filter pair (L_2, H_2) in the global controller introduces a tradeoff between the robustness of the compensation of the passive isolation system and the low frequency noise reduction. For another example, the complementary filter pairs (L_1, H_2) and $(L_2$ and $H_2)$ can be designed together to achieve better overall performance.

Bibliography

[1] R. Abbott, R. Adhikari, G. Allen, S. Cowley, E. Daw, D. DeBra, J. Giaime, G. Hammond, M. Hammond, C. Hardham, J. How, W. Hua, W. Johnson, B. Lantz, K. Mason, R. Mittleman, J. Nichol, S. Richman, J. Rollins, D. Shoemaker, G. Stapfer, and R. Stebbins. Seismic isolation for Advanced LIGO . *Classical and Quantum Gravity*, 19:1591–1597, April 2002.

[2] R Abbott et al. Seismic isolation enhancements for initial and Advanced LIGO. *J. Quantum Grav.*, 21:S915–S921, 2004.

[3] G. Ballardin, L. Bracci, S. Braccini, C. Bradaschia, C. Casciano, G. Calamai, R. Cavalieri, R. Cecchi, G. Cella, E. Cuoco, E. D'Ambrosio, V. Dattilo, A. di Virgilio, L. Fabbroni, F. Fidecaro, and et al. Measurement of the VIRGO superattenuator performance for seismic noise suppression. *Review of Scientific Instruments*, 72:3643–3652, September 2001.

[4] B Barish and R Weiss. LIGO and the detection of gravitational waves. *J. Phys. Today*, 52:44–50, 1999.

[5] M. A. Barton and K. Kuroda. Ultralow frequency oscillator using a pendulum with crossed suspension wires. *Review of Scientific Instruments*, 65:3775–3779, December 1994.

[6] M. A. Barton, T. Uchiyama, K. Kuroda, N. Kanda, and H. Ishizuka. Two-dimensional X pendulum vibration isolation table. *Review of Scientific Instruments*, 70:2150–2154, April 1999.

[7] A. Barzilai, T. Vanzandt, and T. Kenny. Technique for measurement of the noise of a sensor in the presence of large background signals. *Review of Scientific Instruments*, 69:2767–2772, July 1998.

[8] J. Bendat and A. Piersol. *Random data : analysis and measurement procedures.* John Wiley & Sons, 3rd edition, 2000.

[9] D. G. Blair et al. Progress in the development of technology for advanced LIGW detectors. In *Gravitational Wave Detection*, number 75. Universal Academic Press Inc., 1997.

[10] S. Boyd et al. Measuring Voltera kernals. *IEEE Trans. Circuits and Systems*, 30(8):571–577, August 1983.

[11] S. Boyd and L. Vandenberghe. *Convex Optimization.* Cambridge University Press.

[12] Y. Cheng, J. Winterflood, L. Ju, and D. G. Blair. Tilt sensor and servo control system for gravitational wave detection . *Classical and Quantum Gravity*, 19:1723–1729, April 2002.

[13] L. O. Chua et al. Measuring voltera kernals (ii). *International Journal of Circuit Theory and Applications*, 17:151–190, 1989.

[14] P. Daniell. Discussion of on the theoretical specification and sampling properties of autocorrelated time-series. *J. Royal Statistical Society*, 8:88–90, 1946.

[15] J. Van Eijk. *On the design of plate-springs.* PhD thesis, Delft University of Technology, April 1985.

[16] A. Einstein. Näherungsweise integration der feldgleichungen der gravitation. *Sitzungsberichte der Königlich Preussische Akademie der Wissenschaften (Berlin)*, page 688, 1916.

[17] Ceri Evans et al. Periodic signals for measuring nonlinear Voltera kernals. *IEEE transactions on instrumentation and measurement*, 45(2):362–371, April 1996.

[18] P Fritschel. Second generation instruments for the laser interferometer gravitational wave observatory (LIGO) gravitational-wave detection. volume 4856 of *Proc. SPIE*, pages 282–291, Bellingham, WA, 2003.

[19] P Fritschel et al. Seismic isolation subsystem design requirements document. LIGO internal document E990303-03-D, available at http://admdbsrv.ligo.caltech.edu/dcc/, January 2001.

[20] F. Garoi, J. Winterflood, L. Ju, J. Jacob, and D. G. Blair. Passive vibration isolation using a Roberts linkage. *Review of Scientific Instruments*, 74:3487–3491, July 2003.

[21] Z.J. Geng and L.S. Haynes. Six degree-of-freedom active vibration control using the Stewart platforms. *IEEE Transactions on Control Systems Technology*, 2(1):45–53, Mar 1994.

[22] J. Giaime, P. Saha, D. Shoemaker, and L. Sievers. A passive vibration isolation stack for LIGO: Design, modeling, and testing. *Review of Scientific Instruments*, 67:208–214, January 1996.

[23] Corwin Hardham. *Quiet Hydraulic Actuators For LIGO*. Ph. D., Stanford University, June 2005.

[24] J. M. Hensley, A. Peters, and S. Chu. Active low frequency vertical vibration isolation. *Review of Scientific Instruments*, 70:2735–2741, June 1999.

[25] B. Allen ; W. Hua and A. Ottewill. Automatic cross-talk removal from multi-channel data. http://arxiv.org/PS_cache/gr-qc/pdf/9909/9909083.pdf, 1999.

[26] R. Hulse and J. Taylor. Discovery of a pulsar in a binary system. *Astrophysical Journal*, 195:L51–L53, 1975.

[27] Myron Kayton and Walter R. Fried. *Avionics Navigation Systems*. New York : J. Wiley, 2nd edition, 1997. pg. 317.

[28] C. Y. Lee, C. Zhao, E. J. Chin, J. Jacob, D. Li, and D. G. Blair. Control of pre-isolators for gravitational wave detection. *Classical and Quantum Gravity*, 21:1015–+, March 2004.

[29] J. Liu, J. Winterflood, and D. G. Blair. Transfer function of an ultralow frequency vibration isolation system. *Review of Scientific Instruments*, 66:3216–3218, May 1995.

[30] G. Losurdo, M. Bernardini, S. Braccini, C. Bradaschia, C. Casciano, V. Dattilo, R. de Salvo, A. di Virgilio, F. Frasconi, A. Gaddi, A. Gennai, A. Giazotto, H. B. Pan, F. Paoletti, A. Pasqualetti, and et al. An inverted pendulum preisolator stage for the VIRGO suspension system. *Review of Scientific Instruments*, 70:2507–2515, May 1999.

[31] S. Márka, A. Takamori, M. Ando, A. Bertolini, G. Cella, R. DeSalvo, M. Fukushima, Y. Iida, F. Jacquier, S. Kawamura, Y. Nishi, K. Numata, V. Sannibale, K. Somiya, R. Takahashi, H. Tariq, K. Tsubono, J. Ugas, N. Viboud, C. Wang, H. Yamamoto, and T. Yoda. Anatomy of the TAMA SAS seismic attenuation system . *Classical and Quantum Gravity*, 19:1605–1614, April 2002.

[32] A. Matthews and D. A. Bauer. Hemispherical resonator gyro for precision pointing applications. In *Proc. SPIE Vol. 2466, p. 128-139, Space Guidance, Control, and Tracking II, Walter J. Fowski; Morris M. Birnbaum; Eds.*, pages 128–139, June 1995.

[33] Y. Neuvo, Cheng-Yu Dong, and S. Mitra. Interpolated finite impulse response filters. *IEEE Transactions on Acoustics, Speech, and Signal Processing*, 32:563–570, June 1984.

[34] D. B. Newell, S. J. Richman, P. G. Nelson, R. T. Stebbins, P. L. Bender, J. E. Faller, and J. Mason. An ultra-low-noise, low-frequency, six degrees of freedom active vibration isolator. *Review of Scientific Instruments*, 68:3211–3219, August 1997.

[35] A. I. Oliva, M. Aguilar, and V. Sosa. Low- and high-frequency vibration isolation for scanning probe microscopy . *Measurement Science and Technology*, 9:383–390, March 1998.

[36] S. Park and C. F. Quate. Theories of the feedback and vibration isolation systems for the Scanning tunneling microscope. *Review of Scientific Instruments*, 58:2010–2017, November 1987.

[37] J. Peterson et al. Test and calibration of the seismic research observatory. *United State Geological Society Open-File Report*, 80(187), 1980.

[38] M. V. Plissi, C. I. Torrie, M. E. Husman, N. A. Robertson, K. A. Strain, H. Ward, H. Lück, and J. Hough. GEO 600 triple pendulum suspension system: Seismic isolation and control. *Review of Scientific Instruments*, 71:2539–2545, June 2000.

[39] S. J. Richman, J. A. Giaime, D. B. Newell, R. T. Stebbins, P. L. Bender, and J. E. Faller. Multistage active vibration isolation system. *Review of Scientific Instruments*, 69:2531–2538, June 1998.

[40] N. A. Robertson, G. Cagnoli, D. R. M. Crooks, E. Elliffe, J. E. Faller, P. Fritschel, S. Goßler, A. Grant, A. Heptonstall, J. Hough, H. Lück, R. Mittleman, M. Perreur-Lloyd, M. V. Plissi, S. Rowan, D. H. Shoemaker, P. H. Sneddon, K. A. Strain, C. I. Torrie, H. Ward, and P. Willems. Quadruple suspension design for Advanced LIGO . *Classical and Quantum Gravity*, 19:4043–4058, August 2002.

[41] N. A. Robertson, R. W. P. Drever, I. Kerr, and J. Hough. Passive and active seismic isolation for gravitational radiation detectors and other instruments . *Journal of Physics E Scientific Instruments*, 15:1101–1105, October 1982.

[42] N. A. Robertson et al. Seismic isolation and suspension systems for Advanced LIGO. In *Optical Fabrication, Metrology, and Material Advancements for Telescopes*, SPIE, pages 81–91, September 2004.

[43] P. Saulson. *Fundamentals of Interferometric Gravitational Wave Dectectors.* World Scientific, Salem,MA, 1994.

[44] P. R. Saulson. Vibration isolation for broadband gravitational wave antennas. *Review of Scientific Instruments*, 55:1315–1320, August 1984.

[45] J. R. Smith et al. Characterization and operation of the dual-recycled geo 600. *Class. Quantum Grav.*, 21:S1737–S1745, 2004.

[46] C. C. Speake and D. B. Newell. The design and application of a novel high-frequency tiltmeter. *Review of Scientific Instruments*, 61:1500–1503, May 1990.

[47] P. Stoica and R. Moses. *Introduction to Spectral Analysis.* Prentice Hall, 1997.

[48] Jos Sturm. Sedumi. http://fewcal.kub.nl/sturm/software/sedumi.html.

[49] J. Sullivan, Z. Rahman, R. Cobb, and J. Spanos. Closed-loop performance of a vibration isolation and suppression system. In *American Control Conference*, volume 6 of *4-6*, pages 3974–3978. IEEE, Jun 1997.

[50] R. Takahashi, F. Kuwahara, E. Majorana, M. A. Barton, T. Uchiyama, K. Kuroda, A. Araya, K. Arai, A. Takamori, M. Ando, K. Tsubono, M. Fukushima, and Y. Saito. Vacuum-compatible vibration isolation stack for an interferometric gravitational wave detector TAMA300. *Review of Scientific Instruments*, 73:2428–2433, June 2002.

[51] A. Takamori, M. Ando, A. Bertolini, G. Cella, R. DeSalvo, M. Fukushima, Y. Iida, F. Jacquier, S. Kawamura, S. Márka, Y. Nishi, K. Numata, V. Sannibale, K. Somiya, R. Takahashi, H. Tariq, K. Tsubono, J. Ugas, N. Viboud, H. Yamamoto, T. Yoda, and C. Wang. Mirror suspension system for the TAMA SAS . *Classical and Quantum Gravity*, 19:1615–1621, April 2002.

[52] J. Taylor and J. Weisberg. Experimental tests of relativistic gravity using the binary pulsar PSR 1913+16. *Astrophysical Journal*, 345:434–450.

[53] K. Tsubono et al. Tama project. *Proc. of Conference on Gravitational Wave Detection*, pages 183–191, 1997.

[54] P. Vaidyanathan. *Multirate systems and filter banks*. Prentice Hall, 1st edition, 1992.

[55] J. Y. Vinet et al. Proc. of gravitation and cosmology, icgc-95 conference. In *Astrophysics and Space Library*, volume 211, pages 89–93, Pune India, Dec 1995. Kluwer Academic Publishers.

[56] R. Weiss. *Quarterly Progress Report, MIT Research Lab of Electronics*, 105:54.

[57] P.D Welch. The use of fast fourier transform for the estimation of power spectra: A method based on time averaging over short, modified periodograms. *IEEE Trans. Audio Electroacoust*, Vol. AU-15:71–73, June 1967.

[58] J. Winterflood, D. G. Blair, and B. Slagmolen. High performance vibration isolation using springs in Euler column buckling mode. *Physics Letters A*, 300:122–130, July 2002.

[59] J. Winterflood, Z. B. Zhou, L. Ju, and D. G. Blair. Tilt suppression for ultra-low residual motion vibration isolation in gravitational wave detection. *Physics Letters A*, 277:143–155, November 2000.

[60] Z. B. Zhou, S. H. Fan, F. Long, and J. Luo. Improved low frequency seismic noise isolation system for gravitational wave detectors. *Review of Scientific Instruments*, 69:2781–2784, July 1998.

[61] Z. B. Zhou, J. Winterflood, L. Ju, and D. G. Blair. Investigation of a Laser Walk-off Angle Sensor and Its Application to Tilt Measurement in Gravitational Wave Detector. In *Gravitation and Astrophysics*, page 224, 2000.